Universidad
Carlos III de Madrid

PhD THESIS

Mechanical properties of advanced high-strength steels produced via Quenching and Partitioning

Author:

María Irene de Diego Calderón

Directors:

Dr. Ilchat Sabirov

Dr. Jon M. Molina-Aldareguia

A thesis submitted for the degree of Doctor of Philosophy

Departamento de Ciencia e Ingeniería de Materiales e Ingeniería Química

Universidad Carlos III de Madrid

Leganés,18 de Septiembre de 2015

Universidad Carlos III de Madrid

TESIS DOCTORAL

Mechanical properties of advanced high-strength steels produced via Quenching and Partitioning

Autora: María Irene de Diego Calderón

Directores: Dr. Ilchat Sabirov

Dr. Jon M. Molina-Aldareguia

Firma del Tribunal Calificador:

Firma:

Presidente: Prof. Jose Manuel Torralba

Vocal: Dr. Laura Moli Sánchez

Secretario: Prof. José María Cabrera

Calificación:

Leganés, 18 de Septiembre de 2015

On ne veut bien qu'avec le cœur.
L'essentiel est invisible pour les yeux.

Le Petit Prince
Antoine de Saint-Exupéry

ACKNOWLEDGEMENTS

En la fase final de la "aventura" que ha resultado ser la realización de esta tesis doctoral, es necesario hacer un balance de todo lo vivido. Me enfrento a la parte más difícil de este trabajo, los agradecimientos. Sin duda me resulta muy complicado expresar, solamente con palabras, la gratitud que siento hacia todas las personas que, de alguna forma, son también responsables de su culminación.

En primer lugar quiero agradecer a mis directores de tesis, el Dr. Ilchat Sabirov y el Dr. Jon Molina-Aldareguia, su incondicional ayuda, dedicación, apoyo y disponibilidad en todo momento durante la realización de esta tesis. Ha sido un verdadero privilegio trabajar con vosotros durante estos años: sois los mejores mentores que podría haber elegido. Os agradezco enormemente todos los conocimientos científicos que me habéis transmitido, así como el trato cercano y los buenos consejos. ¡Muchas gracias a los dos!

Quiero expresar también mi más sincera gratitud al Instituto IMDEA Materiales. En particular, agradezco al Prof. Javier Llorca y al Prof. José Manuel Torralba la confianza depositada al abrirme las puertas del Instituto. Muchas gracias Javier y José Manuel, por tener vuestras puertas siempre abiertas para escucharme y aconsejarme.

I would like to extend my gratitude to the Department of Materials Science and Engineering of Ghent University of Technology, specially to my host and supervisor, Prof. Roumen Petrov. Thank you very much, Roumen, for your warm welcome in Ghent and all your wise advices. I could never forget to thank my Belgian ladies: Evelien, An, Athina, Aurelie and Elisabete. I am really glad I got to know each and every one of you. I really appreciate our friendship and the good moments we have lived together and those that are to come. Last but not least, I would like to thank to my good friend Dorien: dear Dr. De Knijf, of justice is to acknowledge your co-authorship in part of the results of this thesis. Thanks for sharing your knowledge with me, for letting me learn from you and for becoming a close friend.

El éxito del Instituto IMDEA Materiales radica en que tras los buenos investigadores, hay personas aun mejores. Muchas gracias a mis compañeros de IMDEA, además de por su profesionalidad y sus consejos, por el buen ambiente de trabajo. Me siento muy orgullosa de que muchos de ellos hayan terminado siendo grandes amigos.

Nico, Hangbo, Juan Carlos, Miguel, Jose Luis, Roberto, Edu y Vane: gracias por todo lo que me habéis enseñado y por las risas y buenos momentos. A mi gaditana favorita, Rocío, gracias por transmitirme tu vitalidad y alegría por vivir. Víctor, gracias por las risas y por enseñarme a aprovechar cada minuto al máximo. Luis, mi "hermano pequeño": gracias por conseguir que nos entendamos sin decir palabra. Ali, todo sensibilidad: gracias por hacerme sentir que puedo contar contigo para lo que sea. Belén, mi compañera de carreras: no sabes cuánto te admiro. Gracias por escucharme y aconsejarme en todo momento. Eva, mi compi pero, sobre todo, mi gran amiga: ni te imaginas cuánto me has faltado este último año. Gracias chicos, porque habéis sido capaces de sacarme una sonrisa incluso en los peores momentos. Ha sido un placer compartir este tiempo con vosotros.

No puedo estar más de acuerdo con aquel que dijo que los amigos son la familia que uno elige. En ese sentido me siento muy afortunada por esta familia tan numerosa. Quiero empezar dándole las gracias a Ele, mi chica de la eterna sonrisa contagiosa. Gracias por tu ayuda durante la tesis, pero sobre todo por haberme dejado compartir contigo todos los buenos momentos durante estos años. Sin duda eres el mayor tesoro que guardo de mi Erasmus.

Del mismo modo, gracias a mis amigos de la Carlos III, Pablo, Nico, Javi, Jose, Diego, Jaime, Nacho, Lisbel, Ana y Raquel. Toda esta aventura empezó de vuestra mano. Espero que, donde quiera que nos lleve el futuro, sigamos compartiendo buenos momentos.

A mis amigos de Getafe, muchas gracias por facilitarme la adaptación al sur de Madrid. Os habéis convertido en piezas imprescindibles en mi vida. Quiero hacer mención especial a Cris, tan auténtica y divertida: eres muy sabia, amiga. Y sobre todo a Patri y Rober, muchas gracias por todos los momentos que hemos compartido; no sabéis lo mucho que os estamos echando de menos. Desde luego, es un verdadero lujo teneros como amigos.

A mis chicas, Diana, Marta y Laura quiero deciros gracias, muchas gracias. Gracias por ser capaces de sacarme una sonrisa en los peores días, por hacer que un buen día sea aun mejor al compartir un ratito de charla con vosotras y sobre todo porque sigamos sintiendo como propios, los éxitos y fracasos de cada una después de tantos años.

Gracias a mi familia. A mis abuelos Abel y Dolores, de los que tanto he aprendido y a los que me faltan, mis abuelos Victoriano y Antonia. A mis tías y primos, por

hacerme sentir tan orgullosa de mis orígenes. A mi familia política, Jaime, Juan Carlos y Caridad: gracias por vuestra ayuda, apoyo y por haberme hecho sentir una más desde el primer día. A mis hermanos, que son mi mayor orgullo: Carlos, tan luchador, siempre capaz de sacarme una sonrisa y Abel, tan idealista y valiente. ¡Cuánto me queda por aprender de vosotros! A mis padres Abel y Dolores, mis ejemplos de vida: gracias por los valores y la educación que me habéis proporcionado. Papá, gracias por ser un modelo de perseverancia y de optimismo frente a todas las adversidades de la vida. Mamá, gracias por llevarme a tomar ese "Nestea" cuando estuve a punto de abandonarlo todo. Gracias por creer en mí más de lo que yo lo hago y por conseguir convencerme de que soy capaz de todo lo que me proponga. Todos mis éxitos son vuestros.

Por último a ti, Juancar. Gracias por ser mi punto de equilibrio. Gracias por los ratitos de deporte juntos. Gracias por los viajes. Gracias por Enzo. Gracias por los momentos tranquilos de sofá. Gracias por tenerme siempre tan consentida. Gracias por estar ahí en los buenos momentos, pero sobre todo por sostenerme en los peores. Gracias por conocerme casi mejor de lo que yo lo hago. Gracias por hacerme tan feliz.

Todo este trabajo ha sido posible gracias a vosotros. ¡Muchísimas gracias!

RESUMEN

Los Aceros Avanzados de Alta Resistencia (AHSSs) se utilizan generalmente en la fabricación de componentes que trabajan en condiciones de servicio estáticas y/o a fatiga. Por lo tanto, es necesario que proporcionen un buen compromiso entre coste, comportamiento mecánico y fiabilidad. En los últimos años, se está prestando una gran atención hacia el novedoso tratamiento térmico conocido en inglés como "Quenching and Partitioning" (Q&P) para la producción de AHSSs con microestructuras multifásicas que consisten en mezclas de martensita y austenita retenida, proporcionando de este modo la combinación de resistencia, ductilidad y tenacidad deseada. Sin embargo, a pesar de que ya se ha realizado un importante trabajo de investigación para avanzar en la comprensión de la microestructura y las propiedades mecánicas de estos aceros, resulta imprescindible profundizar aún más en el efecto que la arquitectura microestructural tiene en los aceros Q&P. En particular, no se ha realizado hasta la fecha ningún trabajo que analice el comportamiento a fatiga y fractura de los aceros Q&P. Por este motivo, el principal objetivo de la presente Tesis Doctoral es desarrollar el concepto de diseño microstructural en los aceros Q&P. De este modo se busca mejorar un amplio rango de propiedades mecánicas entre las que se incluyen la resistencia a tracción, así como a fatiga y fractura. Asimismo, se busca establecer la relación entre las citadas propiedades mecánicas, la microestructura y los parámetros de procesado. En este trabajo se ha comprobado que: (i) el comportamiento a tracción y la partición de la deformación entre distintas fases depende en gran medida de la microestructura de los aceros Q&P que, por otra parte, puede ajustarse gracias a la manipulación de los parámetros de procesado Q&P; (ii) las propiedades de la matriz juegan un papel muy importante en el comportamiento a fractura de los aceros Q&P y (iii) la vida a fatiga de los aceros Q&P también está determinada por la microestructura y puede ser mejorada reforzando los bordes entre fases. En base al análisis de los resultados experimentales obtenidos, se muestra que el rendimiento mecánico de los aceros Q&P puede mejorarse a través del diseño microstructural.

ABSTRACT

Advanced high-strength steel (AHSS) grades have been frequently used for applications that require a compromise between cost reduction, mechanical behavior and reliability of components that work under static and fatigue service loading conditions. Quenching and Partitioning (Q&P) is receiving increasing attention as a novel heat treatment to produce AHSSs containing martensite/retained austenite mixtures, with desirable combination of strength, ductility and toughness. However, despite the significant body of research on microstructure and mechanical properties of Q&P steels, there is still a significant lack of knowledge on the effect of microstructural architecture on their mechanical performance. Particularly, no research on fatigue and fracture behavior of Q&P steels has been carried out up-to-date. Therefore, the main objective of this PhD thesis is to develop a concept of microstructural design in Q&P steels in order to improve a wide range of mechanical properties (uniaxial tensile, fatigue and fracture), as well as to gain fundamental understanding of their relationship with the microstructure and Q&P processing parameters. It is demonstrated that: (i) tensile mechanical behavior and strain partitioning between phases strongly depend on the microstructure of Q&P steels, which, in turn, can be tuned via manipulation of the Q&P parameters; (ii) matrix conditions play an important role in fracture behavior of Q&P steels and (iii) fatigue life of Q&P steels is also determined by their microstructure and can be enhanced via improvement of strength of interphase boundaries. Based on the analysis of the experimental results, it is shown that tailoring of the microstructure of Q&P processed steels can lead to further improvement of their mechanical performance.

PREFACE

This dissertation is submitted for the degree of Doctor of Philosophy to the "Universidad Carlos III de Madrid". It is based on the work carried out at IMDEA Materials Institute (Madrid, Spain) under the supervision of Dr. Ilchat Sabirov and Dr. Jon M. Molina-Aldareguia. The work was performed in a strong collaboration with Ghent University (Ghent, Belgium), Delft University of Technology (Delft, The Netherlands), Fundació CTM Centre Tecnològic (Manresa, Spain), Centro Sviluppo Materiali (Rome, Italy), Arcelor Mittal Global R&D Gent (Ghent, Belgium) and ThyssenKrupp Steel Europe AG (Duisburg, Germany), in the frame of the European project "New Advanced High Strength Steels by the Quenching and Partitioning (Q&P) Process" (NewQP) (Grant Agreement No RFSR-CT-2011-00017), funded by the Research Fund for Coal and Steel in the 7th Framework Program.

This doctoral thesis fulfills all the requirements to be awarded with the mention of International Doctorate. In order to use the best available equipment as well as to get in touch with the world's experts in the field, part of the microstructural characterization has been carried out during a 3 months stay at Ghent University (Belgium) under the supervision of Professor Roumen Petrov. Moreover, 2 international experts in advanced high-strength steels, Dr. Javier Hidalgo Garcia (Delft University of Technology, The Netherlands) and Dr. Dimitris Chasoglou (Höganäs AB, Sweden), have reviewed the present manuscript.

The results obtained during the course of this work have led to four peer-reviewed manuscripts, which have been published in the top international journals in the field of metallurgy, one submitted manuscript and another one under preparation by the moment of submission of this PhD thesis:

- I. de Diego-Calderón, M.J. Santofimia, J.M. Molina-Aldareguia, M.A. Monclús, I. Sabirov. "Deformation behavior of a high strength multiphase steel at macro- and micro-scales", Materials Science & Engineering A 611 (2014) 201–221.
- I. de Diego-Calderón, D. De Knijf, M. A. Monclús, J. M. Molina-Aldareguia, I. Sabirov, C. Föjer, R. H. Petrov. "Global and local deformation behavior and mechanical properties of individual phases in a quenched and partitioned steel", Materials Science & Engineering A 630 (2015) 27–35.

- I. de Diego-Calderón, D. De Knijf, J. M. Molina-Aldareguia, I. Sabirov, C. Föjer, R. H. Petrov. "Effect of Q&P parameters on microstructure development and mechanical behavior of Q&P steels", Revista de Metalurgia 51(1) (2015) 1-12.
- I. de Diego-Calderón, P. Rodriguez-Calvillo, A. Lara, J.M. Molina-Aldareguia, R.H. Petrov, D. De Knijf, I. Sabirov. "Effect of microstructure on fatigue behavior of advanced high-strength steels produced by quenching and partitioning and the role of retained austenite", Materials Science & Engineering A 641 (2015) 215–224.
- I. de Diego-Calderón, D. De Knijf, J.M. Molina-Aldareguia, R.H. Petrov., I. Sabirov. "Microstructural design in Quenched and Partitioned (Q&P) steels to achieve improved fracture resistance", Materials Science & Engineering A, submitted.

Finally, this work has also been well received by experts at International Conferences, workshops and seminars in the field of advanced high-strength steels:

- I. De Diego-Calderón, D. De Knijf, M. Monclus, J. Molina-Aldareguia, I. Sabirov, C. Föjer, R. Petrov. EUROMAT 2013. Seville, Spain (September 2013).
- I. De Diego-Calderón, D. De Knijf, J. Molina-Aldareguia, I. Sabirov, C. Föjer, R. Petrov. Materials Science and Engineering 2014. Darmstadt, Germany (September 2014).
- I. De Diego-Calderón, D. De Knijf, R. Petrov, J. Molina-Aldareguia, I. Sabirov. European Workshop 'Advanced Steels: Challenges in Steel Science and Technology'. Madrid, Spain (September 2014).
- 3 internal seminars, IMDEA Materials Institute, Madrid, Spain (October 2013, March 2014, October 2014).
- 1 external seminar, Universidad Carlos III de Madrid, Madrid, Spain (May 2015).
- 2 external seminars, Arcelor Mittal Global R&D Gent, Belgium (April 2014) and ArcelorMittal Maizières Research Global R&D, Maizières-les-Metz, France (April 2015).

TABLE OF CONTENS

1.INTRODUCTION ..... - 3 -
1.1. Advanced High Strength Steels (AHSSs) ..... - 3 -
1.2. Quenching and Partitioning process as an advanced approach for fabrication of AHSSs ..... - 6 -
1.2.1. Background and "Quenching and Partitioning" fundamentals ..... - 8 -
1.2.1.1. Carbon partitioning concept ..... - 8 -
1.2.1.2. Importance of suppressing carbide precipitation ..... - 10 -
1.2.1.3. Selection of suitable chemical compositions for the Q&P steels - 11 -
1.2.1.4. Design of heat treatment ..... - 13 -
1.2.2. Microstructural changes during Q&P process ..... - 14 -
1.3. Strength and ductility of Q&P steels ..... - 16 -
1.3.1. Effect of alloying elements and the Q&P processing route on mechanical properties ..... - 16 -
1.3.2. Mechanical properties of individual Q&P phases and their deformation behavior ..... - 21 -
1.3.3. Strain partitioning in Q&P steel grades during plastic deformation ..... - 23 -
1.4. Stability of retained austenite during plastic deformation and its effect on mechanical properties ..... - 25 -
1.4.1. Grain size of the retained austenite ..... - 25 -
1.4.2. Morphology of the retained austenite ..... - 26 -
1.4.3. Local carbon concentration in the retained austenite ..... - 27 -
1.4.4. Constraining effect of the surrounding phases ..... - 28 -

1.4.5. Orientation of the retained austenite ..... - 28 -
1.5. Fracture behavior of Q&P steels ..... - 29 -
1.6. Effect of microstructure on cyclic behavior of Q&P steels ..... - 31 -
2.MOTIVATION AND OBJECTIVES ..... - 35 -
3.EXPERIMENTAL PROCEDURES ..... - 39 -
3.1. Materials and processing ..... - 39 -
3.2. Microstructural characterization ..... - 43 -
3.2.1. X-ray diffraction (XRD) ..... - 43 -
3.2.2. Scanning electron microscopy (SEM) ..... - 45 -
3.2.3. Electron backscatter diffraction (EBSD) ..... - 46 -
3.2.4. Representation of textures ..... - 49 -
3.2.5. Atomic force microscopy (AFM) ..... - 51 -
3.3. Mechanical behavior ..... - 52 -
3.3.1. Uniaxial tensile testing ..... - 52 -
3.3.2. Nanoindentation tests ..... - 54 -
3.3.3. *In situ* tensile testing and digital image correlation analysis ..... - 57 -
3.3.4. Fracture characterization ..... - 60 -
3.3.5. Fatigue characterization ..... - 65 -
3.3.5.1. Analysis of fatigue fracture surfaces ..... - 66 -
3.3.5.2. Microstructural evolution of RA during fatigue testing ..... - 67 -
4.RESULTS AND DISCUSSION ..... - 71 -
4.1. Effect of Q&P parameters on microstructure development and mechanical behavior of the Q&P steels ..... - 71 -
4.1.1. Effect of Q&P parameters on microstructure and mechanical properties ..... - 71 -
4.1.1.1. Influence of QT ..... - 75 -
4.1.1.2. Influence of PT ..... - 78 -

4.1.1.3. Influence of Pt ..... - 79 -
4.1.2. Textures after Q&P treatment ..... - 81 -
4.1.3. Conclusions to Section 4.1 ..... - 83 -
4.2. Global and local deformation behavior and mechanical properties of individual phases in the Q&P steels ..... - 85 -
4.2.1. Properties of the individual microconstituents in the Q&P steel ..... - 85 -
4.2.2. Local plastic deformation of the Q&P steel ..... - 91 -
4.2.3. Conclusions to Section 4.2 ..... - 97 -
4.3. Fracture behavior of Q&P steels ..... - 98 -
4.3.1. Microstructure and mechanical properties ..... - 98 -
4.3.2. Three-dimensional models of fracture surfaces for analysis of fracture behavior ..... - 100 -
4.3.2.1. Dimple size and energy required to form dimple structure of fracture surface ..... - 103 -
4.3.2.2. Local and global fracture toughness ..... - 105 -
4.3.2.3. Crack growth resistance ..... - 109 -
4.3.3. The principles of microstructural design in Q&P steels to improve their fracture properties ..... - 110 -
4.3.4. Conclusions to Section 4.3 ..... - 111 -
4.4. Fatigue behavior of Q&P steels ..... - 112 -
4.4.1. Microstructure of the Q&P processed steels before cyclic deformation ..... - 112 -
4.4.2. Tensile properties of Q&P steels ..... - 116 -
4.4.3. Cyclic behavior of Q&P steels ..... - 116 -
4.4.4. Evolution of microstructure in the Q&P steels during fatigue testing ..... - 117 -
4.4.4.1. Effect of cyclic deformation on phase composition of the Q&P steels ..... - 117 -

4.4.4.2. Effect of crystallographic orientation of RA on its stability during cycling ..... - 119 -
4.4.5. Fatigue fractography analysis and mechanisms of fatigue crack initiation and propagation..... - 122 -
4.4.6. Conclusions to Section 4.4..... - 124 -
5.CONCLUSIONS..... - 129 -
6.FUTURE WORK..... - 133 -
7.BIBLIOGRAPHY..... - 137 -

LIST OF ABREVIATIONS AND SYMBOLS

LIST OF ABREVIATIONS

AFM	Atomic force microscopy
AHSSs	Advanced high-strength steels
BIW	Body-in-white
BCC	Body centered-cubic lattice
CCE	Constrained carbon equilibrium
CP	Complex phase
CTOA	Crack-tip-opening angle
CTOD, δ	Crack-tip-opening displacement
. $\mathbf{OD_i^{local}}$	Local crack-tip-opening displacement at the moment of fracture initiation
$\mathbf{COD_i}$	Average crack-tip-opening displacement at the moment of fracture initiation
DBTT	Ductile-brittle transition temperature
DENT	Double edge-notched tensile
DEM	Digital elevation model
DIC	Digital image correlation
DP	Dual phase
EBSD	Electron backscatter diffraction
EDM	Electrical discharge machining
EF	Epitaxial ferrite
EPFM	Elastic-plastic fracture mechanics
FCC	Face centered-cubic lattice
HCF	High cycle fatigue
IQ	Image quality map
LCF	Low cycle fatigue
LEFM	Linear elastic fracture mechanics
MMC	Metal matrix composite
ND	Normal direction
OIM	Orientation Imaging Microscopy
ODF	Orientation distribution function
Pt	Partitioning time
PT	Partitioning temperature

QT	Quenching temperature	**Q&P**	Quenching and Partitioning
RA	Retained austenite	**RD**	Rolling direction
SEM	Scanning electron microscopy	**SNOM**	Scanning near field microscope
SPM	Scanning probe microscopy	**STM**	Scanning tunneling microscopy
TD	Transverse direction	**TM**	Tempered martensite
TRIP	Transformation induced plasticity	**TWIP**	Twinning induced plasticity
ULSAB	Ultra Light Steel Auto Body	**UM**	Untempered martensite
XRD	X-ray diffraction		

LIST OF SYMBOLS

a	Total crack length	**a´**	Nanoindentation contact radius
a_γ	Austenite lattice parameter	**A**	Nanoindentation contact area at peak load
$A(h_c)$	Nanoindentation projected area of contact at peak load	**A_o**	Initial cross-section area
b	Ligament length	**B**	Brass component
c	Radius of plastic zone	**C**	Copper component
C'	Cube component	**C_r**	Residual function
d	Interplane distance	**d_n**	Dimensionless constant
E	Young modulus	**E_r**	Reduce modulus
F	Tensile force	**G**	Goss component
g(x)	Gray level intensity in the deformed configuration	**G(x)**	Gray level intensity in the reference configuration
h	Nanoindentation penetration depth	**$\dot{h}$**	Nanoindentation penetration rate of the indenter

h_c	Nanoindentation depth of contact	h_f	Nanoindentation final depth of the residual hardness impression
h_{max}	Nanoindentation depth at peak load	h_o	Dimple depth
H	nanohardness	I_o	Initial current
J	J contour integral	K_{1C}	Fracture toughness
L	Length	L_o	Initial gage length
m	Dimensionless constant	M_f	Martensite finish temperature
M_s	Martensite start temperature	n	Strain-hardening exponent
N	Number of cycles to failure	P	P component
P_{max}	Nanoindentation peak indentation load	R'	Radius of the Berkovich indenter tip
RC	Rotated cube component	RG	Rotated Goss component
R_{surf}	Specific plastic strain energy to form the micro-ductile structure	R_{tot}	Total crack growth resistance
S	Stress amplitude	S'	S component
S_t	Nanoindentation measured stiffness	t	Thickness
U_i	Displacement vector	V	Measured potential value
V_o	Initial potential value	W	Width
x_i	Arbitrary pixel position in the deformed configuration	X_{Al}	Aluminum concentration
X_C	Carbon concentration	X_i	Arbitrary pixel position in the reference configuration
X_{Mn}	Manganese concentration	y	One half of the potential probe span
α	Wavelength of the X-ray	Δa	Crack propagation from the fatigue pre-crack
ΔL	Change in gage length	ε	Engineering strain
ε_f	Elongation to failure	ε_U	Uniform elongation

$\dot{\varepsilon}$	Strain rate	η	Pre-factor in the R_{tot} formula to evaluate J
Θ	Scattering angle	ν	Poisson's ratio
σ	Engineering stress	σ_{UTS}	Ultimate tensile strength
σ_Y	Yield stress	$\sigma_{0.2}$	0.2 % proof stress
$\bar{\sigma}$	Flow stress of the material	τ_{max}	Maximum shear stress under the indenter
ϕ_1, Φ, ϕ_2	Bunge notation for expressing Euler angles	$\nabla(U)$	Constant displacement gradient within the subset

LIST OF FIGURES

Figure 1-1. Porsche Cayenne body structure material composition [6]..... - 3 -

Figure 1-2. Overview of tensile strength and total elongation combinations for various classes of conventional and AHSS grades [6, 9]. ..... - 6 -

Figure 1-3. Schematic illustration of the Q&P process. Redrawn from [9]. ..... - 7 -

Figure 1-4. Scheme of morphology and carbon profiles during different stages of the intercritically annealed Q&P process. (A is austenite, IF is intercritical ferrite, EF is epitaxial ferrite, and M is martensite) [20]. ..... - 15 -

Figure 1-5. Total elongation vs. tensile strength diagram obtained via Q&P for different chemical compositions following full austenitization. PT are given in the legend [58]. ..... - 18 -

Figure 1-6. Uniform elongation and ultimate tensile strength of samples subjected to Q&P processing, compared to high performance grades [56]..... - 20 -

Figure 1-7. Schematic representation of three micro-mechanisms of fracture in metals: (a) ductile fracture, (b) cleavage and (c) inter-granular fracture. Re-plotted from [102]. ..... - 30 -

Figure 3-1. Equilibrium phase diagram calculated by Thermo-Calc® of the chemistries shown in Table 3-1, expressed as a function of the percentage of C: (a) QP-0.25 and (b) QP-0.28..... - 40 -

Figure 3-2. Constructive interference in Bragg's law [135]. ..... - 44 -

Figure 3-3. SEM schematic view [138]. ..... - 46 -

Figure 3-4. Schematic representation of the typical EBSD geometry, showing the pole piece of the SEM, the electron beam, the tilted specimen, and the phosphor screen [149]. ..... - 47 -

Figure 3-5. Definition of the orientation of a coordinate system, following the conventional interpretation of the Euler angles. In order 1, 2, 3 as shown, describes the rotation between the specimen (RD, TD, ND) and crystal axes (100, 010, 001), respectively [149, 153]. ..... - 50 -

Figure 3-6. Basic AFM set-up [155]. ..... - 51 -

Figure 3-7. Schematic representation of the Berkovich indenter [157]. ..... - 54 -

Figure 3-8. A schematic representation of load versus indenter displacement for an indentation experiment [159]. ..... - 55 -

Figure 3-9. Kammrath&Weiss tensile/compression module (a) and SEM EVO MA15 (b). ..... - 58 -

Figure 3-10. Schematic representation of the working principle of the DIC technique. ..... - 59 -

Figure 3-11. Crack-tip-opening displacement (CTOD). An initially sharp crack blunts with plastic deformation, resulting in a finite displacement (CTOD) at the crack tip [102]. ..... - 61 -

Figure 3-12. Schematic illustration of the DENT specimen. ..... - 62 -

Figure 3-13. Monoscopic SEM image example image taken at (a) 0° and (b) 5°; (c) Shaded surface plot of the 3D-reconstructed object [176]. ..... - 64 -

Figure 3-14. Geometry of the specimens for fatigue testing..... - 65 -

Figure 3-15. Specimen mounted on testing device..... - 66 -

Figure 4-1. OIM maps of (a) the sample quenched at 224°C (QP-0.25-1), (b) the sample quenched at 244°C (QP-0.25-3) and (c) the sample quenched at 264°C for 500 s (QP-0.25-7); all of them were partitioned at 350°C for 500 s. (d) The sample partitioned at 300°C for 500 s (QP-0.25-2), (e) the sample partitioned at 350°C for 500 s (QP-0.25-3) and (f) the sample partitioned at 400°C for 500 s (QP-0.25-5); all of them were quenched at 244°C. (g) The sample partitioned at 400°C for 100 s (QP-0.25-4), (h) the sample partitioned at 400°C for 500 s (QP-0.25-5) and (i) the sample partitioned at 400°C for 1000 s (QP-0.25-6); all of them were quenched at 244°C. ....- 72 -

Figure 4-2. Engineering stress - engineering strain curves from tensile testing of the sample quenched at 224°C (QP-0.25-1), the sample quenched at 244°C (QP-0.25-3) and the sample quenched at 264°C for 500 s (QP-0.25-7). All of them were partitioned at 350°C for 500 s. ..... - 76 -

Figure 4-3. Engineering stress - engineering strain curves from tensile testing of the sample partitioned at 300°C for 500 s (QP-0.25-2), the sample partitioned at 350°C for 500 s (QP-0.25-3) and the sample partitioned at 400°C for 500 s (QP-0.25-5); all of them were quenched at 244°C. ..... - 78 -

Figure 4-4. Engineering stress - engineering strain curves from tensile testing of the sample partitioned at 400°C for 100 s (QP-0.25-4), the sample partitioned at 400°C for 500 s (QP-0.25-5) and the sample partitioned at 400°C for 1000 s (QP-0.25-6); all of them were quenched at 244°C. ..... - 80 -

Figure 4-5. Orientation distribution functions (ODFs) in ϕ_2 = 0°, 45° and 65° sections for RA in sample QP-0.25-2 (a) and QP-0.25-3 (b). (RC = Rotated Cube, C = Copper, RG = Rotated Goss, B = Brass and G = Goss). ..... - 82 -

Figure 4-6. Orientation distribution functions (ODFs) in $\phi_2 = 45°$ sections for martensite in sample QP-0.25-2 (a) and QP-0.25-3 (b). ..... - 83 -

Figure 4-7. (a) OIM map and (b) residual indents imaged by AFM in the sample partitioned at 400°C for 500 s (QP-0.25-5). ..... - 85 -

Figure 4-8. (a) Representative load-displacement curves from nanoindentation experiments on RA on the sample partitioned at 400°C for 100 s (QP-0.25-4) and the sample partitioned at 400°C for 500 s (QP-0.25-5). The load-displacement curves in (a) were converted into (P/h) vs. h curves of ≈1450 μN and ≈1150 μN in (b) and (c), respectively. ..... - 88 -

Figure 4-9. Representative load-displacement curves from nanoindentation experiments on TM in the studied steel. ..... - 89 -

Figure 4-10. Evolution of in-plane local plastic strain distribution during tensile deformation of the sample partitioned at 400°C for 500 s (QP-0.25-5) to the global plastic strain of (a) 5 %, (b) 10 % and (c) 15 %. The loading direction is vertical (indicated by a black arrow). ..... - 92 -

Figure 4-11. SEM images of the sample partitioned at 400°C for 500 s (QP-0.25-5): (a) initial microstructure; (b) microstructure after tensile deformation to the global plastic strain of ≈ 22 % (necking area). ..... - 93 -

Figure 4-12. Distribution of local plastic strain on surface of the sample partitioned at 300°C for 500 s (QP-0.25-2) (a) and the sample partitioned at 400°C for 500 s (QP-0.25-5) (b) after tensile deformation to a global plastic strain of 12.5 %. Histograms of plastic strain distribution for both samples (c). ..... - 95 -

Figure 4-13. Distribution of local plastic strain on surface of the sample partitioned at 400°C for 100 s (QP-0.25-4) (a) and the sample partitioned at 400°C for 500 s (QP-0.25-5) (b) after tensile deformation to a global plastic strain of 12.5 %. Histograms of plastic strain distribution for both samples (c). ..... - 96 -

Figure 4-14. OIM maps of (a) the QP-0.25-5 sample, (b) the QP-0.28-1 sample and (c) the QP-0.28-2 sample..... - 98 -

Figure 4-15. Fracture surface of (a) the QP-0.25-5 sample, (b) the QP-0.28-1 sample and (c) the QP-0.28-5 sample. Corresponding DEMs for: (d) the QP-0.25-5 sample, (e) the QP-0.28-1 sample and (f) the QP-0.28-2 sample..... - 101 -

Figure 4-16. (a and b) SEM images of corresponding regions on both specimen halves of the QP-0.25-2 sample; corresponding profiles (c) through the fracture surface element in (a) and (d) the fracture surface element in (b)..... - 102 -

Figure 4-17. Profiles through the corresponding fracture surface element of Figure 4-16 at the (a) beginning of local failure and (b) moment of local failure..... - 103 -

Figure 4-18. A schematic view of the direct approach to separate fracture energies. Redrawn from [178]. ..... - 104 -

Figure 4-19. (a and b) SEM images of corresponding midsection regions on both specimen halves of the QP-0.25-5 sample tested at room temperature; (c) profiles at the moment of fracture initiation in the PT-400 sample at room temperature $COD_i^{local} = 4.5\ \mu m$..... - 106 -

Figure 4-20. Profiles from the DEM of fracture surface showing the moment of (a) start of crack growth and (b) crack propagated to 0.2 mm. ..... - 108 -

Figure 4-21. OIM maps of the QP-0.28- sample, illustrating the microstructural heterogeneity which leads to a high scatter in the resistance against crack propagation. Close-up views of the areas within the rectangles shown in 1, 2 and 3..... ..... - 109 -

Figure 4-22. Combined gray scale band contrast and color coded phase map of the QP-0.25-5 steel grade before fatigue (top), after fatigue testing with the highest stress amplitude (bottom left) and after fatigue testing with the lowest stress amplitude (bottom right). ..... - 113 -

Figure 4-23. Combined gray scale band contrast and color coded phase map of the QP-0.28-2 steel grade before fatigue (top), after fatigue testing with the highest stress amplitude (bottom left) and after fatigue testing with the lowest stress amplitude (bottom right). ..... - 114 -

Figure 4-24. QP-0.25-5 and QP-0.28-2 steel grades *S-N* curves comparative..... - 117 -

Figure 4-25. Histograms of RA grain size (a,c) and RA aspect ratio distribution (b,d) in the QP-0.25-5 (a,b) and the QP-0.28-2 (c,d) samples before and after fatigue testing. .....- 119 -

Figure 4-26. Orientation distribution functions (ODFs) in ϕ_2 = 0°, 45° and 65° sections for retained austenite in sample QP-0.28 before and after fatigue testing. .....- 120 -

Figure 4-27. The distribution of the mechanical driving force for the martensitic transformation in orientation space, ϕ_2 = 0°, 45° and 65°. Low values of the modeled mechanical driving force correspond to low transformation potentials [95]... .....- 121 -

Figure 4-28. Fatigue fracture surface of the QP-0.28-2 grade formed after fatigue testing with high stress amplitude (600 MPa and $6 \cdot 10^3$ cycles). I stands for fatigue crack initiation area, II for fatigue crack propagation area and III for the last stage of fracture.....- 123 -

Figure 4-29. Fatigue fracture surface of the QP-0.28-2 grade formed in the fatigue crack initiation area after testing with low stress amplitude (425 MPa and $2 \cdot 10^5$ cycles). SEM image (a) and stereo image (b). Striations are marked by white arrows..... .....- 123 -

Figure 4-30. Fatigue fracture surface of the QP-0.28-2 grade formed in the final stage of fatigue after testing with high stress amplitude (600 MPa and $6 \cdot 10^3$ cycles) (a), and with low stress amplitude (475 MPa and $6 \cdot 10^5$ cycles) (b).....- 124 -

LIST OF TABLES

Table 3-1. Chemical composition of the studied steel grades (wt. %). ..... - 40 -

Table 3-2. Q&P processing parameters applied to the studied steel grades. ..... - 41 -

Table 3-3. Estimated martensite start temperature (M_s) and martensite finish temperature (M_f) for the studied compositions. ..... - 42 -

Table 4-1. Q&P processing parameters applied to the studied steel grade. ..... - 71 -

Table 4-2. Average grain size (equivalent circle diameter) for the different microconstituents of the Q&P steel. ..... - 73 -

Table 4-3. Volume fraction and carbon content (wt. %) of RA and volume fraction of UM and TM in the studied steel. ..... - 74 -

Table 4-4. Mechanical properties measured on miniature samples of the studied steel grade ($\sigma_{0.2}$, σ_{UTS}, ε_u, ε_f, n). ..... - 75 -

Table 4-5. Elasto-plastic material properties obtained from the nanoindentation tests for the RA, TM and UM (nanohardness H). ..... - 86 -

Table 4-6. Maximum shear stress in TM underneath the Berkovich indenter. ..... - 90 -

Table 4-7. Average grain size (equivalent circle diameter) for the different microconstituents of the Q&P steel grades. ..... - 99 -

Table 4-8. Volume fraction and carbon content (wt. %) of RA and volume fraction of UM and TM in the studied steel grades. ..... - 100 -

Table 4-9. Mechanical properties measured on the studied Q&P steel grades ($\sigma_{0.2}$, σ_{UTS}, ε_u, ε_f, n). ..... - 100 -

Table 4-10. The depth of dimples and the plastic strain energy to form a unit area of the dimple structure on the fracture surface (R_{surf}). ..... - 105 -

Table 4-11. The results of fracture surface analysis and estimation of fracture toughness and crack growth resistance. ..... - 107 -

Table 4-12. Average grain size (equivalent circle diameter) for the different microconstituents of the Q&P steel grades. ..... - 113 -

Table 4-13. Volume fraction and carbon content (wt. %) of RA and volume fraction of UM and TM in the studied steel grades. ..... - 115 -

Table 4-14. Fraction of RA (%) measured by EBSD before and after fatigue testing at the distance of 1 mm from the fracture surface. ..... - 115 -

1 Introduction

1. INTRODUCTION

1.1. Advanced High Strength Steels (AHSSs)

Vehicle designers must balance the objectives of better fuel economy, crash safety standards imposed by governments and stringent consumer demands [1]. The steel industry is continuously presenting innovative solutions to the automotive industry, since this material has the ability to adapt to the changing requirements. In particular, in 1994, a consortium of 35 major sheet-steel producers around the world launched the Ultra Light Steel Auto Body (ULSAB) series of programs to design and build a lightweight steel structure to meet new safety and performance targets, by decreasing fuel consumption and gas emissions at the same time [2-5]. In addition to low weight and good mechanical behavior, high levels of formability, joinability, weldability and paintability were important points to have a competitive material [1].

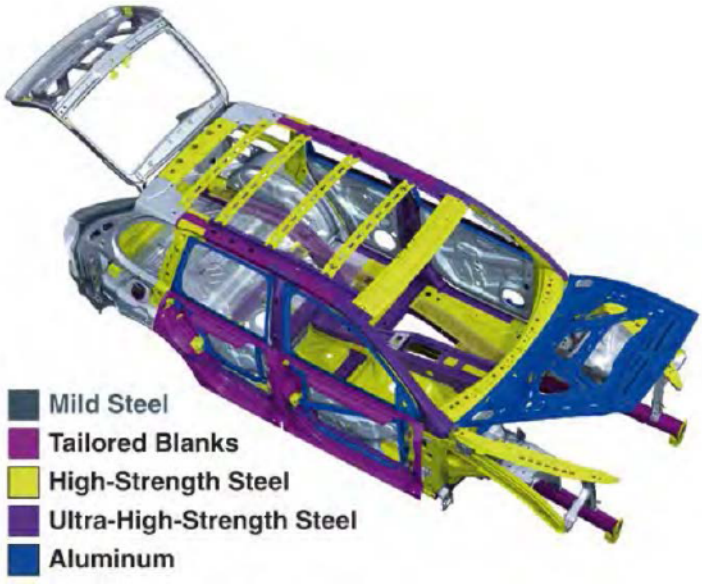

Figure 1-1. Porsche Cayenne body structure material composition [6].

The body-in-white (BIW) structural parts and panels, and in particular the materials used in car construction, offer the greatest possibilities in terms of weight reduction and determine its behavior in the event of collisions (see Figure 1-1) [1]. The first BIW unveiled in 1998, validated the ULSAB program's design concepts, and a major contributor to its success was a group of new steel types and grades called advanced

high-strength steels (AHSSs) [6, 7]. In consequence, over the past decade, with increasing demands for weight reduction in the automotive industry a significant research effort has been directed towards the development of several types of AHSSs [3], as they provide an opportunity for the development of cost-effective and light-weight parts with improved safety and optimized environmental performance [4, 8, 9].

AHSS grades are complex, sophisticated materials, with carefully selected chemical compositions and multiphase microstructures resulting from precisely controlled heating and cooling processes [1, 7]. They have been frequently used for applications that require a compromise between cost reduction, weight saving, fuel economy, higher mechanical performance and reliability of components which work under high static and particularly fatigue service loading conditions [10, 11]. Various strengthening mechanisms are employed to achieve a range of strength, ductility, toughness, and fatigue properties. The research strategies are based on the development of microstructures consisting of ultrafine microconstituents formed in non-equilibrium conditions, such as polygonal ferrite, bainitic ferrite, retained austenite (RA), stress/strain-induced martensite and athermal martensite [1, 12-14]. The tailored combination of soft and hard phases and the presence of RA provides to the AHSS grades the superior strength-ductility balance demanded by the car industry [1, 3, 15]. Some types of AHSSs have a higher strain hardening capacity resulting in a strength-ductility balance superior to conventional steels. Other types have ultra-high yield and tensile strength and show a weak hardening behavior [6]. The high strength martensitic or bainitic constituents contribute to a simultaneous increase of strength and toughness, whereas RA provides an improvement of strength and ductility through the strain-induced transformation of the metastable austenite to hard martensite, i.e., the transformation induced plasticity (TRIP) effect [15, 16]. The strain induced transformation to martensite provides an additional deformation and strain-hardening mechanism, thereby suppressing strain localization and enhancing formability [17, 18].

All AHSSs are produced by controlling the chemistry and cooling rate from the austenite or austenite plus ferrite phase, either on the run-out table of the hot mill (for hot-rolled products) or in the cooling section of the continuous annealing furnace (continuously annealed or hot-dip coated products). However, the AHSSs can be divided into three groups. The so-called “first generation” of the AHSS grades comprises dual phase (DP), transformation induced plasticity (TRIP) and complex

phase (CP) steels showing combination of high strength and good ductility. These steel grades are typically low alloyed and have ferrite based multiphase microstructure [9]. DP steels consist of a ferritic matrix containing islands of a hard martensitic second phase. An increase of the volume fraction of hard second phases generally increases its strength. DP steels are produced by controlled cooling from the two-phase ferrite plus austenite region to transform some austenite to ferrite, before a rapid cooling transforms the remaining austenite to martensite. The soft ferrite phase is generally continuous, providing excellent ductility. When these steels are deformed, strain is concentrated in the lower-strength ferrite phase surrounding the islands of martensite, creating the unique high initial work-hardening rate exhibited by these steels [6]. The microstructure of TRIP steels is made up of RA embedded in a primary matrix of ferrite. TRIP steels typically require the use of an isothermal holding at an intermediate temperature, which produces some bainite. Therefore, hard phases such as martensite and bainite are also present in varying amounts. During deformation, the dispersion of hard second phases in soft ferrite creates a high work hardening rate, as observed in the DP steels. However, in TRIP steels the RA progressively transforms to martensite with increasing strain, thereby increasing the work hardening rate at higher strain levels [6]. CP steels typify the transition to steel with very high ultimate tensile strengths. The microstructure of CP steels contains small amounts of martensite, RA and pearlite within the ferrite/bainite matrix. CP steels are characterized by high energy absorption, high residual deformation capacity and good hole expansion [6].

The “second generation” of the AHSSs consists of highly alloyed austenitic steels, such as the austenitic twinning induced plasticity (TWIP) steels. These steels are very attractive for engineering due to their superior mechanical properties, but their high cost and complexity of their industrial processing limit their applications [9]. TWIP steels usually have a high manganese content (17-24 %) that causes the steel to be fully austenitic at room temperature. A large amount of deformation is driven by the formation of deformation twins, which gives the name to this steel class. The twinning causes a high instantaneous hardening value as the microstructure becomes finer and finer. The resultant twin boundaries act like grain boundaries and strengthen the steel. TWIP steels combine extremely high strength with extremely high formability [6].

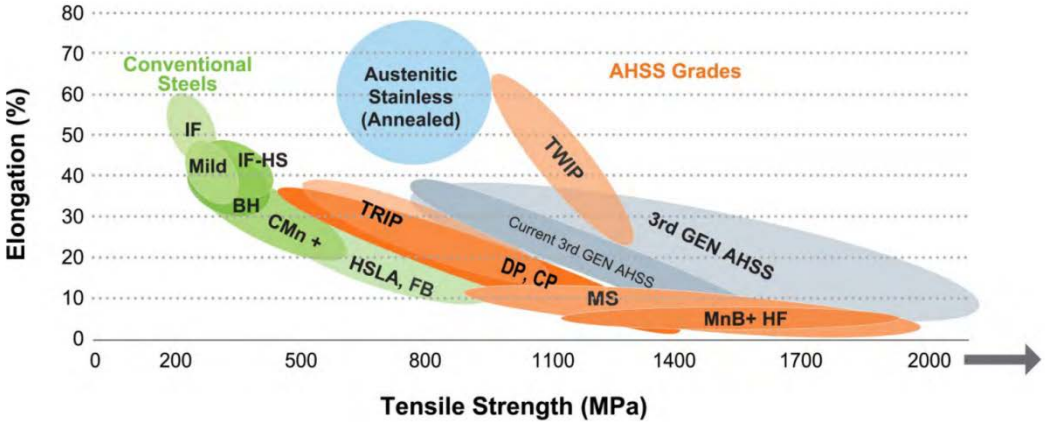

Figure 1-2. Overview of tensile strength and total elongation combinations for various classes of conventional and AHSS grades [6, 9].

These "first and second generations" of AHSS grades are uniquely qualified to meet the functional performance demands of certain parts. For example, DP and TRIP steels have already been widely used in the automotive industry as they provide good formability at room temperature and crash performance of the car for high energy absorption. For structural elements of the passenger compartment, extremely high-strength steels, such as martensitic steels result in improved safety performance [6, 9].

Nevertheless, there are limiting factors that produce a wide gap between the currently available AHSS grades of the first and second generations. The broad range of properties is best illustrated in Figure 1-2, where an overview of representative properties compared to those exhibited by conventional steel grades is depicted. Recently significant research efforts have been channeled into the development of the "third generation" of AHSSs. These steels have improved strength-ductility combinations compared to existing grades, with potential for more efficient joining capabilities, at lower costs. [12-14]. Therefore, ongoing research activities are focused on increasing strength, ductility and toughness to higher levels than exhibited by the "first generation" of the AHSSs without significant changes on their chemical composition, i.e. on the "third generation" of the AHSS grades [9, 16, 17].

1.2. Quenching and Partitioning process as an advanced approach for fabrication of AHSSs

Speer *et al.* first proposed in 2003 a novel processing route for the production of austenite-containing steels, based on a new understanding of carbon diffusion from martensite into RA, the so-called "Quenching and Partitioning" (Q&P) process [19].

Q&P appears promising as a further improvement of mechanical properties can be attained via intelligent microstructural design [20, 21].

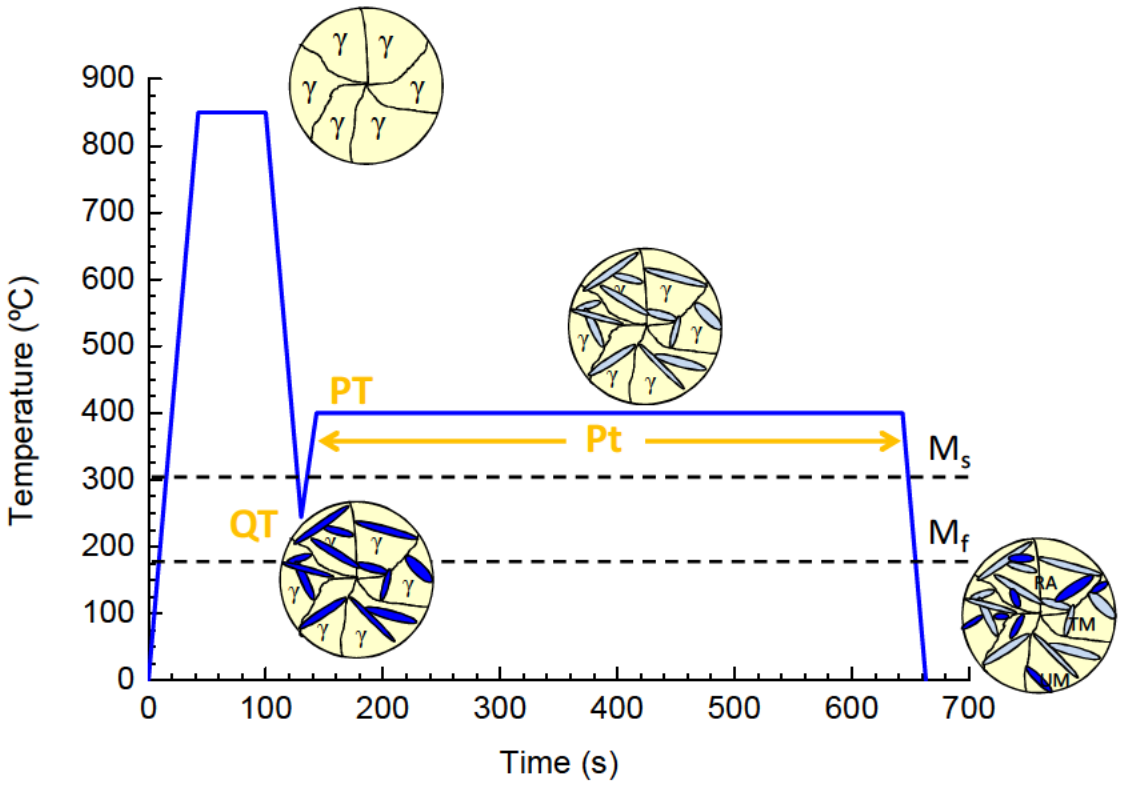

Figure 1-3. Schematic illustration of the Q&P process. Redrawn from [9].

As schematically presented in Figure 1-3, the Q&P process consists of a multi-step thermal processing route [22]:

- First, after heating so as to obtain a fully austenitic or intercritical microstructure, the steel is quenched to a suitable pre-determined temperature (quenching temperature, QT) below the martensite start (M_s) but above the martensite finish (M_f) temperatures in order to form a pre-defined amount of martensite [9, 16]. The microstructure at this QT consists of martensite and untransformed austenite if it was fully austenitized or contains additional ferrite if it was intercritically annealed.
- Then, at the second step, the steel is either isothermally held at this QT (one step Q&P) or brought to a higher (two-step Q&P) partitioning temperature (PT). The aim of the latter step is to carbon-enrich the untransformed austenite remaining at the QT through carbon depletion of the carbon supersaturated martensite [23, 24]. In this way, after final quenching to room temperature, metastable RA is obtained [23, 24].

Consequently, a complex microstructure is generated consisting of metastable RA, ferrite (in the case of partial austenitization) and martensite formed after final quenching to room temperature [9, 23]. The use of martensite rather than ferrite, has the immediate attraction of attaining potentially higher strength levels [23]. For that reason, Q&P steels exhibit desirable combinations of strength, ductility and toughness, which permit their use in a new generation of AHSSs for automobiles [6].

The Q&P heat treatment was envisioned to have application to high-strength austenite containing TRIP sheet products, replacing isothermal bainitic heat treatment of low-carbon steels. Some suggested advantages of Q&P include the potential for greater carbon enrichment of austenite, decoupling of the bainitic ferrite growth kinetics from the carbon partitioning process, and increasing strength via formation of substantial quantities of lath martensite in the microstructure [16].

1.2.1. Background and "Quenching and Partitioning" fundamentals

1.2.1.1. Carbon partitioning concept

Although the existence of carbon-enriched RA in martensitic steel microstructures has been known for some time, the concept of using carbon partitioning from martensite to stabilize RA was not previously developed towards a steel treatment process. This was mainly due to two reasons:

- The temperature which is used normally is too low for substantial amounts of carbon diffusion to occur [16].
- Carbon supersaturation in martensite is ordinarily eliminated by a different mechanism, such as carbide precipitation during tempering [16, 23].

As a consequence, whereas carbon-enriched RA has been identified in martensitic steels for some time [25], the thermodynamics of carbon partitioning between martensite and austenite has been scarcely considered [16]. Recently, a computational model has been implemented in order to address carbon partitioning from as-quenched martensite into untransformed austenite and hence to understand the carbon redistribution across the phase interfacial region during partitioning [23, 26]. Competing reactions, such as bainite, cementite or transition carbides precipitation are assumed to be suppressed. This model predicts the endpoint of partitioning, when martensite is in metastable equilibrium with austenite [16]. It is first required to define several important concepts. Paraequilibrium can be described as the metastable equilibrium between austenite and martensitic ferrite under

conditions where long-range diffusion of carbon occurs but partitioning of slow-moving substitutional elements is difficult [16, 23]. However, this concept is typically applied during transformation and, thus, when interface migration is occurring. In this model [23, 26], the interface between martensite and untransformed austenite is assumed to be stationary, i.e., constrained. In particular, it has been recently suggested that the carbon partitioning from martensite into austenite is controlled by the constrained carbon equilibrium (CCE) criterion [16, 23, 27]. In such case, the metastable martensite/austenite equilibrium reached by the completion of carbon partitioning is described by two conditions:

- One thermodynamic requirement: equal chemical potential of carbon in each phase (martensite and austenite).
- One key matter balance constraint: conservation of iron (and substitutional) atoms in each phase [16, 23].

In constraint paraequilibrium, the thermodynamic condition can be satisfied by an infinite set of possible phase compositions, but the conservation condition of the matter balance associated with the stationary interface uniquely determines the applicable phase compositions. The phase fractions are determined by the extent of the martensite reaction at the QT and not by the lever rule applied using an equilibrium or paraequilibrium tie-line. Consequently, by combining the thermodynamic requirement with the mass balance requirement, it is possible to calculate the extent of carbon partitioning and hence austenite stabilization, according to the total carbon concentration and volume fractions of martensite and untransformed austenite determined by the QT (obtainable from the Koistinen and Marburger relationship [28]). This has shown that most of the carbon in the steel is expected to partition to the austenite and thus, that quite high levels of carbon enrichment, and hence strong austenite stabilization, are possible [16, 23].

The results of the CCE model were successfully used to propose the novel Q&P process. On the other hand, austenite grain size and mechanical stability by the introduction of dislocation forests may affect both the M_S temperature [29] and phase fractions predictions [22]. Simulations have also been used to understand carbon partitioning to austenite from martensite through intercritical ferrite, resulting in austenite inhomogeneity after Q&P [30]. The austenite morphology (and size) and characteristics of the martensite, such as the carbon supersaturation and dislocation density [31, 32], may also influence carbon diffusion, along with the coupling of the

austenite with neighboring phases. Thus a variety of additional refinements could be implemented in order to improve the coming models [22].

1.2.1.2. Importance of suppressing carbide precipitation

The Q&P process, giving greater control over the respective volume fractions of martensitic ferrite and untransformed austenite, can make possible potentially very high carbon concentrations in the austenite. The escape of carbon from the martensite to the untransformed austenite during the partitioning treatment is a critical step for the Q&P process, since it competes with the formation of carbides in the martensite, the normal characteristic of the tempering process [23]. These carbon atoms are no longer available to enrich the austenite since any carbide formation effectively "consumes" carbon. It is hence necessary to understand and control all the carbide precipitation processes that may occur during partitioning [16]. The escape path of the carbon between the martensitic plate and the austenite may vary, since the exact morphology and distribution of the untransformed austenite regions within the partially transformed microstructure are not known precisely, and might be expected to differ, for example, with steel composition and whether the untransformed austenite has an interlath-lamellar or blocky morphology [23]. "Dynamic stabilization" of austenite may also occur during quenching [33], associated with carbon partitioning during epitaxial ferrite (EF) growth upon cooling after intercritical annealing [12, 30, 34].

In martensite, fine transition carbides are usually not considered detrimental, whereas cementite can be of more concern. Thus, usually, the greater emphasis has been on understanding when transition carbides are replaced by cementite formation [35, 36], rather than on the initiation of transition carbide precipitation. Nevertheless, for Q&P processing any transition carbide diminishes the potential for carbon enrichment of austenite [16]. Carbon trapping at crystallographic defects, and austenite decomposition to ferrite and cementite as a result of martensite tempering during Q&P will also reduce the amount of available carbon for partitioning to austenite [19, 37-39]. Precipitation of transition carbides within RA has not been documented. Since the chemical potential of carbon is much higher in the as-quenched martensite than in the RA, it is reasonable to conclude that carbide nucleation would be more likely in BCC ferrite than in austenite. The α/γ interface is also a favored site for carbide formation [40]. Carbon trapping, along with carbon supersaturation of the martensite is consistent with the lower experimental austenite

fractions often achieved compared with predictions [31, 32]. Opportunities clearly exist to better understand how carbon supersaturation is relieved in the martensite and how martensite substructure evolves to result in the availability of carbon to diffuse to austenite during partitioning [22]. In any event, the extent to which carbide formation is suppressed will be a critical factor influencing the microstructures that are achievable using the Q&P process [16].

1.2.1.3. Selection of suitable chemical compositions for the Q&P steels

Carbide precipitation in martensite is often observed during the partitioning step in high-carbon steels [41] and even in low-carbon steels [34]. In order to expand the Q&P heat treatment window to lower PTs, the transitional carbide reaction within the martensitic ferrite must be suppressed. This attracts special interest in the case of industrial applications [23]. Therefore, as pointed out by Speer *et al.* [19], it is important to choose appropriate chemical compositions in order to avoid carbide precipitation in realizing an ideal Q&P conditions. The role of alloying elements on transition carbides (e.g. epsilon or eta) is less clear with respect to martensite tempering, but knowing how alloying elements influence the transition carbide formation and their evolution is critical for improving the understanding of martensite tempering and advancing Q&P.

The approach described by Wever [42] indicates that alloying elements can influence the iron equilibrium diagram in two different ways:

- By expanding the γ-field, and encouraging the formation of austenite over wider compositional limits. These elements are called γ-stabilizers. Important steel alloying elements such as C, N, Ni and Mn, as well as Cu, Co and some inert metals, belong to this group [42, 43].
- By contracting the γ-field, and encouraging the formation of ferrite over wider compositional limits. These elements are called α-stabilizers. Si, Al, Be, P and B fall into this category, together with strong carbide-forming elements such as Ti, V, Mo, Cr and Ta [42, 43].

During martensite tempering, Si was probed to efficiently retard cementite formation [44]. In particular, Si delays the transition from early-stage tempering (where ε or η carbides are present) to later-stage tempering (where θ-Fe_3C is present) as well as the formation of cementite during the bainite transformation, resulting in "carbide-free" bainite [23, 43]. The suppression of cementite is usually explained by its low solubility in cementite, and thus a need to diffuse away from the growing

carbide [45]. Then, cementite formation may be delayed or even suppressed through additions of Si [41, 44]. Al and even P are thought to behave similarly to Si in retarding tempering reactions [16]. Such elements thus play a critical enabling role in the Q&P process.

Alternative reactions affecting carbon enrichment and retention of the untransformed austenite, such as the formation of ferrite, pearlite or bainite during the partitioning step are also to be avoided [23, 30]. Otherwise, the formation of new phases would reduce the amount of austenite available for stabilization. For this reason, the selected chemical composition should also contain γ-stabilizing elements, so as to reduce the temperature window for bainite formation as well as to delay ferrite and bainite incubation times for the longest possible time [30]. Alloying elements such as Mn and Ni have been proven effective in reaching those targets [23, 30].

Finally, during Q&P processing the steel must be quenched at a sufficiently rapid rate to avoid the decomposition of austenite during cooling to such products as ferrite, pearlite and bainite [30]. The effectiveness of the quench will depend primarily on two factors: the geometry of the specimen and the composition of the steel. Hardenability is, therefore, of greatest importance, and an interesting approach is based on selection of the appropriate concentration of alloying elements [43]. C has a strong influence on hardenability, but its use at higher levels is limited, because of the lack of toughness as well as the greater difficulties in fabrication [43]. Cr is widely used as an alloying element in wrought steel due to its relatively low cost and to its effectiveness as an alloying element. Cr has many interesting effects on steel [43], but it is considered amongst the cheapest alloying additions per unit of increased hardenability. Especially when combined with Mn [46, 47], a substantial improvement in hardenability can be seen [43].

Thus it is clearly seen that the Q&P processing route cannot be applied to every steel. All these alloying elements have already been extensively used in AHHSs [9, 14]. As an example, in DP steels, C enables the formation of martensite at practical cooling rates by increasing the hardenability of the steel. Mn, Cr, Mo, V and Ni either added individually or combined also help to increase hardenability. C and Si also act as ferrite solute strengtheners. These additions must be carefully balanced, not only to produce unique mechanical properties, but also to maintain the generally good resistance to spot welding capability [6]. TRIP steels use higher quantities of carbon than DP steels to obtain sufficient C content for stabilizing the RA to room

temperature. Suppressing the carbide precipitation during bainitic transformation appears to be crucial for TRIP steels. Si and Al are used to avoid carbide precipitation in the bainite region. These elements also assist in maintaining the necessary carbon content within the RA [6]. Low carbon "lean alloy" TRIP steel compositions, such as the 0.2C-1.5Mn-1.5Si (wt. %) alloy, have been used to successfully generate martensitic microstructures with substantial RA levels through Q&P processing [22, 48]. Some TRIP steel alloy modifications have also been investigated, including partial replacement of Si by Al [15, 34] which has been shown to yield slightly inferior RA stabilization.

1.2.1.4. Design of heat treatment

A schematic diagram summarizing the sequence of microstructural evolution from homogeneous austenite during Q&P processing is presented in Figure 1-3. Following austenitization the steel is quenched to a QT estimated so as to produce a pre-determined fraction of martensite and balancing fraction of untransformed austenite. The steel temperature is then raised to the PT, when carbon escapes into the untransformed austenite. Therefore, following partitioning, the chemical stability of austenite is raised, so after subsequent cooling to room temperature it is retained [23].

The QT determines the fraction of martensite that undergoes carbon partitioning to the neighboring austenite during the partitioning step. A QT closely above the M_f temperature leads to the formation of an elevated fraction of martensite, which leaves a small fraction of austenite available for carbon enrichment. On the contrary, a QT closely below the M_s temperature produces a small fraction of martensite, so the C available for partitioning might not be sufficient for the stabilization of the austenite. This trade-off leads to the determination of an optimal QT for a maximum volume fraction of RA. Theoretical selection of this optimum QT requires previous knowledge of the martensite kinetics in the steel [30]. In particular, a QT selection methodology was developed by Speer *et al.* [49] to predict stable austenite fractions as a function of QT. This methodology is based on the following assumptions [19, 23, 30, 50]:

- There is full carbon partitioning from the martensite to the austenite at the end of the partitioning step.
- Martensite/austenite interface is fixed.

- Any other phenomena such as bainite formation or carbide precipitation are precluded.

First, the relative fractions of martensite and untransformed austenite at the QT are calculated from the undercooling below M_s, based on the Koistinen-Marburger relationship [28]. Then, by applying the Koistinen-Marburger relationship [28] to the carbon-enriched untransformed austenite fraction after full partitioning, the final phase fractions after final cooling can be predicted [23, 50]. This methodology has been proved to be effective for calculating optimum QTs for yielding the maximum amount of RA [23, 51]. The appropriate QT can be defined as the temperature where just the right amount of martensite is formed during the initial quench to enrich the untransformed austenite after full partitioning, in order to reduce its M_s temperature to room temperature [23].

The second and third statements above imply that the austenite fraction does not change during partitioning. Although these assumptions can lead to a good approximation of the optimal QT, the amount of carbon that actually partitions from the martensite to the austenite also depends on the PT and Pt: the Pt must be long enough to lead to considerable carbon partitioning, but also be restricted, since the risk of formation of carbides as a consequence of the martensite and austenite tempering also increases at longer times [16, 30]. It is important to consider that increasing PT can accelerate the carbon partitioning from martensite to austenite. However, the risk of carbide precipitation and the formation of other phases, such as bainite, is increased at higher temperatures [12].

Consequently, the different heat treatment schedule for processing steels by Q&P would lead to modified behavior. The design of adequate Q&P heat treatments requires an understanding of the phenomena that may affect to the final microstructure of the material during this processing route [34].

1.2.2. **Microstructural changes during Q&P process**

Assuming that all possible overlapping processes were successfully inhibited, the final Q&P steel grade will consist of a complex multiphase microstructure. In general terms, two distinct microstructures are expected, whether the Q&P processing route starts with full or partial austenitization [12, 30, 34].

First, steels produced by Q&P processing with full austenitization have some morphological similarities with the microstructures present in carbide-free bainitic steels [52]. They are formed by microstructures containing [24]:

- Carbon-depleted martensite laths (i.e. tempered martensite (TM)), formed during the first cooling to QT and which underwent carbon partitioning to the austenite. In some cases, carbide precipitation in these phases can be observed, due to the auto-tempering of the martensite.
- RA and untempered martensite (UM), formed during the last quench to room temperature. This martensite will be different to that previously formed as it will normally be expected to inherit a higher carbon concentration.
- Occasionally, islands of bainite can be present, as well, depending on the chemistry and Q&P parameters.

In such case, the final volume fraction of martensite and austenite at room temperature will be related to the martensite and austenite grain sizes before the partitioning step, whereas the carbon concentration gradient within the martensite and austenite grains will determine the thermal stability of the austenite [30, 50].

Second, the microstructures resulting from intercritical annealing usually consist of a ferritic matrix and islands of TM (formed during the first cooling), UM and RA (formed during the last quench) embedded in the matrix [12]. At longer Pts, decomposition of austenite into bainite has also been reported [34]. For illustrative purposes, microstructural changes during Q&P processing of the steel with intercritically annealing until the QT is reached are schematically presented in Figure 1-4.

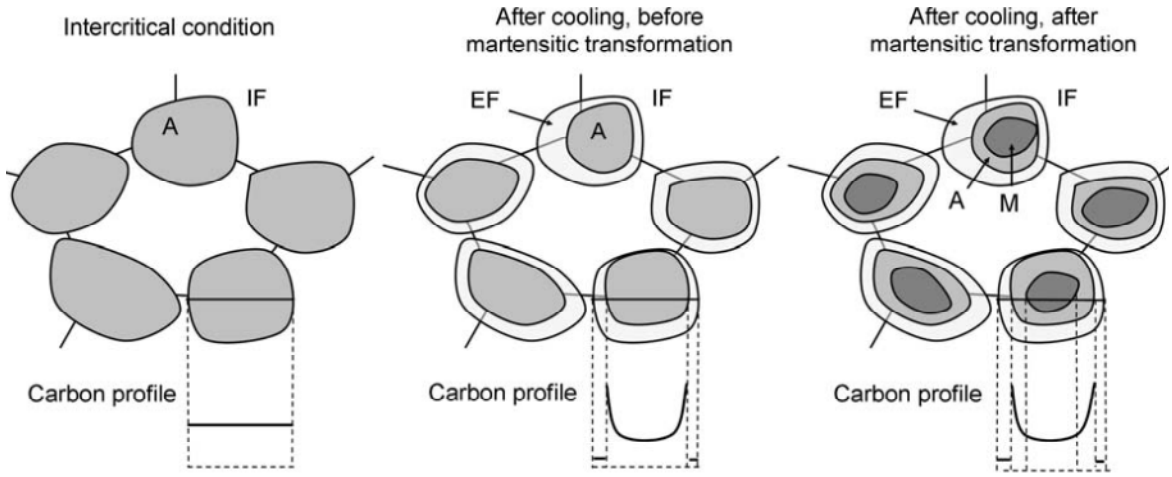

Figure 1-4. Scheme of morphology and carbon profiles during different stages of the intercritically annealed Q&P process. (A is austenite, IF is intercritical ferrite, EF is epitaxial ferrite, and M is martensite) [20].

Frequently, the ferritic areas that are closer to the austenite/martensite grains correspond to ferrite that has grown from the ferrite present after the intercritical treatment during the first cooling, the so called EF [12, 30]. Thus, in this case, carbon partitioning into austenite may also occur through the ferrite present in the microstructure prior to the partitioning step. EF formation introduces carbon gradients in the remaining austenite during the first cooling step. This will lead to an enhanced carbon enrichment close to austenite boundaries and an inferior carbon concentration in areas well inside austenite grains. As a result, the formation of martensite at the quenching step takes place in the carbon-depleted interior zones of the former austenite grain. After the second quench, the surrounding austenite will be either transformed (UM) or retained (RA) [12, 30].

In any case, it is clear that the resulting multiphase microstructure of the Q&P processing will consist of a combination of RA, TM and UM, together with, in some cases ferrite and bainite. The different Q&P heat treatment routes would lead to different microstructures and hence, to different mechanical behaviors. The complex combination of different phases makes the understanding of the microstructures obtained by classical etching techniques not directly applicable to Q&P structures. A more accurate description of the microstructure is essential for better understanding of the microstructure formation and better control of the final properties of the material [12].

1.3. Strength and ductility of Q&P steels

It was suggested for long time that strength and ductility are mutually exclusive in steels, i.e. strengthening of steel results in decrease of its ductility, thus dramatically limiting its practical utility [52-54]. Significant research activities have been focused on improvement of low ductility of high-strength steels. Below, the effect of steel chemistry and microstructure on strength and ductility of Q&P steels is considered in detail.

1.3.1. Effect of alloying elements and the Q&P processing route on mechanical properties

The effect of alloying elements on the microstructure and mechanical properties of the Q&P steels has been reported in literature: i.e. for C [24, 54-56], Mn [24, 57], Si [24, 58, 59], Al [58], Mo [58], and Ni [55, 56].

De Moor *et al.* examined mechanical properties in different Q&P steels subjected to different Q&P processing routes [58]. Five different steels with different chemical compositions were subjected to the Q&P process at different PT (300, 350, 400, and 450°C) following full austenitization. The chemical compositions of the steels were:

- CMnSi: 0.2C-1.63Mn-1.63Si
- CMnSi: 0.24C-1.61Mn-1.45Si-0.30Al
- CMnAlSi: 0.25C-1.70Mn-0.55Si-0.69Al
- MoCMnAl: 0.24C-1.60Mn-0.12Si-1.41Al-0.17Mo
- MoCMnSi: 0.21C-1.96Mn-1.49Si-0.25Mo

It was found that the partial replacement of Si by Al (CMnSi) leads to significantly lower fractions of RA at the same partitioning conditions, whereas some addition of Mo (MoCMnSi) results in somewhat higher fractions of RA as well as in its reduced sensitivity to increased holding at the PT. Alloying with both Al and Mo (MoCMnAl) also results in lower volume fractions of RA. The effect of alloying elements on the tensile mechanical properties was studied, as well. The stress-strain curves displayed a strong dependence on the partitioning conditions. For example, the ultimate tensile strength of the CMnSi was found to be in the range of 1100 to 1390 MPa and decreased with increasing partitioning time, whereas the yield strength showed the opposite trend. Uniform elongation was in the range of 5 to 12 % and total elongation was in the range of 5 to 18 %. Tensile strengths of 1280-1510 MPa and yield strengths of 1050-1200 MPa were obtained with uniform elongations of 4-11 % and total elongations of 4-15 %, for the MoCMnSi grade obtained by the Q&P processing following full austenitization. Higher yield and tensile strength were obtained for the MoCMnSi grade rather than for the CMnSi alloy. Tensile strength of the MoCMnSi grade decreases with increasing partitioning temperature. No clear trend with temperature or time was observed for the yield strength. A significant improvement in elongation was obtained especially given the higher strength levels. In addition, the highest PT results in the highest ductility [58].

The tensile properties obtained for the MoCMnAl grade, yield strength values of 1030-1150 MPa and tensile strength of 1170-1420 MPa were obtained with total elongations of 4-9 % and uniform elongations of 3-5 %. Although much lower Si content, higher yield strength values were obtained compared to the strength of the CMnSi alloy. It should also be noted that the Al-grade containing the lowest RA fractions exhibits also the lowest ductility levels, whereas the highest combinations of strength and ductility were obtained for the Mo-grade with the greatest amount of

RA. The tensile mechanical properties are summarized in Figure 1-5. It was shown that the most effective contribution of the TRIP mechanism to the increased strain hardening was obtained for longer Pt and/or higher PT leading to higher volume fraction of RA [58].

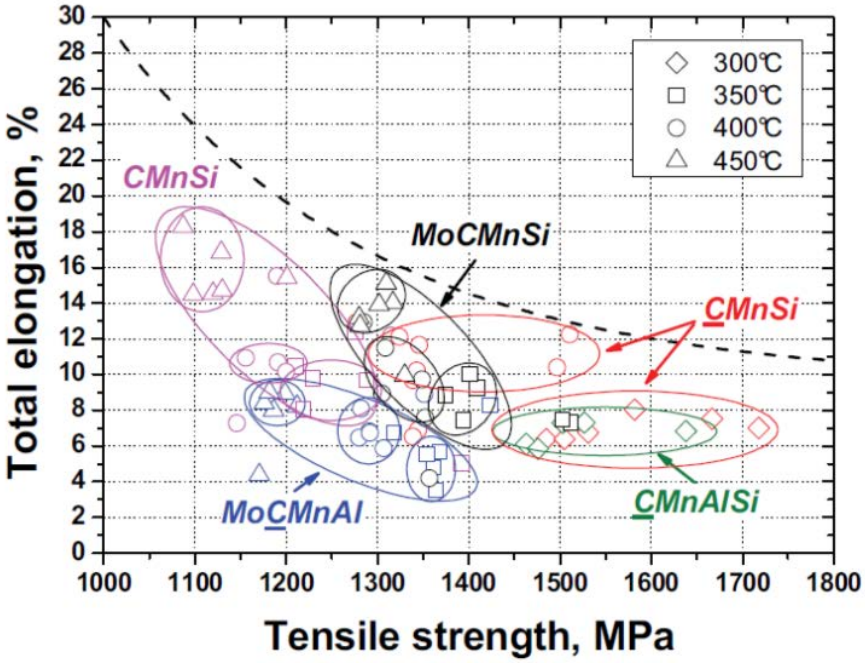

Figure 1-5. Total elongation vs. tensile strength diagram obtained via Q&P for different chemical compositions following full austenitization. PT are given in the legend [58].

In [24], the effect of C and Mn on the Q&P response of CMnSi steels was studied. Three CMnSi steel grades with C contents ranging from 0.2 to 0.3 wt. % and Mn contents of 3 and 5 wt. % were subjected to the Q&P processing with intercritical annealing and with full austenitization. The results of this study can be roughly generalized as follows. For the steels after the Q&P processing with intercritical annealing:

- Yield strength increases with increasing C content from 0.2 to 0.3 wt. %, whereas the ultimate tensile strength shows the opposite trend.
- Both uniform elongation and total elongation slightly decrease with increasing C content.
- Strain hardening ability decreases with increasing C content (ultimate tensile strength / yield strength ratio can be considered as an indirect measure of strain hardening ability).

- Both yield strength and ultimate tensile strength increase with increasing Mn content from 3 to 5 wt. %, whereas uniform elongation and total elongation show the opposite trend.
- No any clear correlation between the volume fraction of RA and mechanical properties (strength and ductility) is seen.

For the steels after Q&P with full austenitization:

- Yield strength decreases with increasing C content from 0.2 to 0.3 wt. % whereas the ultimate tensile strength shows the opposite trend.
- Strain hardening ability increases with increasing C content.
- Both uniform elongation and total elongation slightly increase with increasing C content for the materials quenched to the temperature below 230°C.
- There is a significant effect of partitioning time on strength and ductility of both 0.2C-3Mn-1.6Si and 0.3C-3Mn-1.6Si grades.
- An increase of Mn content from 3 to 5 wt. % leads to degradation of ductility due to the presence of UM in the microstructure of the 0.3C-5Mn-1.6Si steels.
- No any clear correlation between the volume fraction of RA and mechanical properties (strength and ductility) is seen.

It should be noted that the steels after Q&P processing with full austenitization generally show much higher strength properties and somewhat lower ductility compared to the same steels after Q&P processing with intercritical annealing.

In [57], the effect of Si and Mn on the microstructure and mechanical properties of steel grades with 0.43 wt. % C was studied. An increase of Si content from 2.03 to 2.6 wt. % results in higher volume fraction of RA after partitioning at 300°C and 350°C. The material with increased Si content showed lower strength properties and higher ductility. The enhanced Mn content (from 0.59 to 1.17 wt. %) slightly increased ductility without significant change of strength.

The effect of the Q&P processing on the microstructure and mechanical properties of Ni added high strength steels was studied in [55, 56]. In [56], three different steel grades:

- $\mathbf{H_CL_{Ni}}$ 0.37C-2.45Si-2.27Mn-1.47Ni-0.8Cr-0.58Mo; M_s =273°C.
- $\mathbf{H_CH_{Ni}}$ 0.39C-2.64Si-2.39Mn-4.83Ni-0.78Cr-0.5Mo; M_s =202°C.
- $\mathbf{L_CH_{Ni}}$ 0.28C-3.0Si-2.37Mn-5.3Ni-0.71Cr-0.6Mo; M_s =242°C.

were subjected to the Q&P processing. The austenitization temperature varied (870°C and 930°C). PT included 350, 400, and 450°C with partitioning times 10,

30, 100, and 1000 s at each temperature. Microstructural studies showed that the samples austenitized at 930°C have a higher volume fraction of RA than the samples austenitized at 870°C for the same Q&P conditions.

Higher RA fractions were obtained in the samples partitioned at the highest temperature, 450°C. The steel grade H_CH_{Ni}, demonstrated higher volume fractions of RA (15-32 % depending on the partitioning parameters) compared to other grades. Data on uniform elongation and ultimate tensile strength of the studied materials are presented in Figure 1-6 in comparison with other high performance steels. It is seen that the H_CL_{Ni} grade has the highest strength (1500-1900 MPa) and uniform elongation (5-15 %), whereas the H_CH_{Ni} grade shows much lower strength (500-900 MPa) and very low uniform elongation (1-3 %).

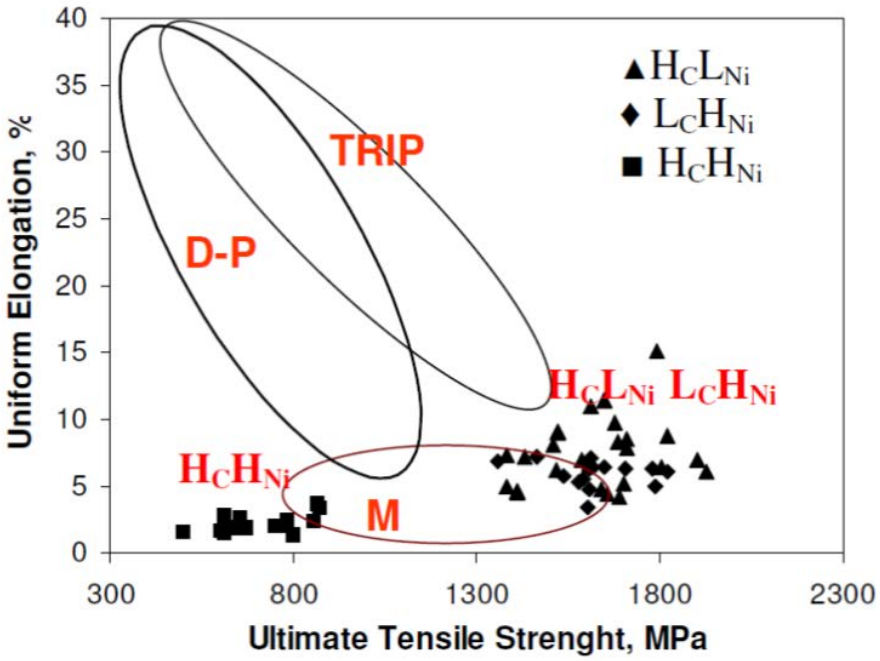

Figure 1-6. Uniform elongation and ultimate tensile strength of samples subjected to Q&P processing, compared to high performance grades [56].

Low carbon Q&P steels containing film-like intercritical ferrite were developed in [59]. Santofimia *et al.* demonstrated that both uniform and total elongation in a low carbon steel after Q&P processing increased with volume fraction of RA [59]. Two low carbon steels with the varying content of Si (1.54 and 0.45 wt. %) and Al (0.006 and 0.22 wt. %) were used. The materials were subjected to the Q&P processing route with intercritical annealing. The obtained microstructures in both steels contained ferrite grains separated by films of RA and/or martensite. It was found that the volume fraction of RA increases with increasing Si content. Volume fraction

of RA dramatically increased with increasing partitioning time up to 100 s and nearly saturated at the reached values. The samples partitioned for 10 s showed higher strength, whereas the higher ductility was obtained in the samples partitioned for 100 s. Strength of both materials decreased with increasing volume fraction of RA, whereas ductility showed the opposite trend.

In [54], Cao *et al.* investigated the effect of C on the microstructure and mechanical response of the low alloyed steels after Q&P processing. Three steel grades with varying C content (0.21, 0.37, and 0.41 wt. %) were subjected to Q&P processing [54]. It was demonstrated that the volume fraction of RA significantly increases from 12 % to 27 % with increasing carbon content. Similar trend can be noted for tensile strength increasing from ≈1300 MPa to ≈1800 MPa and for uniform elongation increasing from 10 % to 14 % whereas total elongation did not change (≈20 %).

In addition, the fine substructure in the Q&P heat treated condition is apparently responsible for the elevated strength levels [16]. Nevertheless, the deformation behavior at the micro- scale with respect to the local microstructure has not been investigated so far. Therefore, there is a need for fundamental understanding of the local deformation behavior of the Q&P steels with respect to the local microstructure, since manipulation of the microstructure via optimization of their chemical composition and Q&P processing parameters can lead to further increase of mechanical properties.

1.3.2. **Mechanical properties of individual Q&P phases and their deformation behavior**

The first requirement for a deep understanding of the property - microstructure relationship in Q&P steels is the knowledge of the flow properties of each of the phases of the microstructure. Since it is not possible to reproduce the same phases in single phase microstructures (especially in the case of RA), the properties of the individual phases have to be directly characterized in the fine grained multiphase microstructures. The only technique which allows hardness measurements at such fine scale is nanoindentation [60].

In [60], Furnémont *et al.* measured the nanohardness of the different phases present in the microstructure of two TRIP-assisted multiphase steels differing from their Si content. According to their results, it appears that the softest phase in both steels was the ferritic matrix, followed by bainite, austenite and martensite, which was found to

be the hardest phase of the microstructure [60]. The observed high hardness values of the martensite may be explained by the high levels of carbon in martensite (≈0.6–1 wt. %), since the heat treatment aims at concentrating all the carbon in a small volume fraction of austenite that transforms afterwards into martensite [60]. In addition, in [20] de Diego-Calderón *et al.* reported that RA in Q&P intercritically annealed steels is also enriched by carbon atoms diffused from martensite during the partitioning process, leading to an extra solution hardening of this phase [20]. Therefore, despite RA has usually been considered to have lower strength and higher formability compared to ferrite [61], the authors found that RA should have increased strength comparable to that of ferrite [20]. This agrees well with the results of He *et al.* [62] which shows that the hardness of RA is higher than that of the ferrite in a TRIP-assisted steel. On the other hand, in [63, 64] nanoindentation techniques were used to evaluate the matrix strength of Fe-C binary martensitic steels with various carbon contents and tempering temperatures. The matrix strength was found to decrease with increasing tempering temperature for all sample compositions [63, 64].

It should be noted that the local properties of some individual microconstituents may vary at nanoscale (≈10…100 nm) within their interior. For example, carbon diffusion from martensite into RA during partitioning process should lead to inhomogeneous distribution of C atoms within both martensite and RA [34], thus, leading to variations of the local strength within these microconstituents [60]. For instance, in [65], nanoindentation measurements were performed in commercially produced DP steels in order to quantify the hardness of the individual constituents, i.e., ferrite and martensite. The authors observed a significant range of hardness values for each constituent which reflects the inhomogeneous distribution of chemical content within grains, dislocation density variation within grains and/or potential contributions of the microstructure below the indented plane [65]. This effect has also been reported for TRIP-assisted steels. For example, in [62] it is interesting to note that although a small variation in hardness was reported for ferrite, a large scatter in RA was observed. The authors claim that the large scatter among RA grains could be due to a different mechanical stability and grain boundary structure in different RA grains [62].

1.3.3. Strain partitioning in Q&P steel grades during plastic deformation

Although there are already works on characterization of the steel microstructure after Q&P and on the relationship between the microstructure and the obtained mechanical properties [12, 20, 21, 53, 66], there is still a lack of knowledge about the strain distribution between the microstructural constituents in Q&P structures during loading in the plastic range. During plastic deformation, the microstructural heterogeneity in materials with multiphase microstructures can result in significant stress and strain partitioning among phases, that may be greatly affected by the difference in strength of the individual microconstituents [67, 68]. It was already demonstrated that global deformation behavior and global mechanical properties of DP steels strongly depend on mechanical properties, morphology and spatial distribution of individual phases [69-71]. Factors such as the martensite volume fraction, its grain orientation and morphology, all influence the micro-deformation behavior on a local scale [68]. The ferritic regions which develop high localized plastic strain are determined by the morphology of the surrounding microstructure, since they are usually highly constrained by close martensite blocks [69, 70], rather than by the ferrite grain orientation or the interphase boundaries [68, 69]. This suggests that quite different deformation behaviors could be exhibited by similar steel grades, depending on the microstructure that is developed during processing [68].

Q&P steel grades have more complex microstructures compared to DP steels, and, thus, their plastic deformation at the micro-scale should have more complex character too. However, investigations of the relation between the local microstructure and local plastic deformation in Q&P steels have just begun. Therefore, there is a need for fundamental understanding of the local deformation behavior of the Q&P steels with respect to the local microstructure since microstructural design via optimization of their chemical composition and Q&P processing parameters can lead to further increase of mechanical properties.

Very recently in [20], de Diego-Calderón et al. have reported the effect of the microstructure on the local mechanical behavior of an intercritically annealed Q&P steel. A strong partitioning of plastic strain between the microconstituents was observed at all deformation steps. The plastic strain accommodated by a given phase or constituent was observed to be inversely proportional to its nanohardness [20]. Besides, the degree of strain partitioning between 'hard' and 'soft' phases was strongly increased with increasing the global plastic strain.

During deformation of Q&P intercritically annealed processed steels [20], a network-like structure of interconnected bands of localized plastic flow develops, whereas a significant fraction of little or non-deformed areas remains present. These bands initiate in RA and ferrite leading to their hardening, as plastic yielding starts in the soft phases, whereas the hard martensite remains in the elastic state [20]. During the plastic deformation of the soft phases, stress is transferred to the martensite. However, it should be noted that martensite also provides significant contribution to plastic deformation. The martensite starts to deform plastically when the transferred stress is large enough to reach its elastic limit. As a result, deformation bands can also cross hard phase islands when high global plastic strains are applied and the local shear stress is sufficient to cause localized plastic flow in the harder phases [20]. It should be noted that the experimental observation of plastic deformation in martensite was already reported earlier in [15, 72]. Moreover, the amount of plastic strain accommodated by individual martensite grains does not depend on their orientation with respect to the loading axis. However, soft phases such as retained austenite and ferrite elongated along tensile axis have lower amount of plastic strain compared to the soft phases inclined at 45° or perpendicular to the loading axis [20].

The network-like structure described in [20] for intercritically annealed Q&P steels, has also been observed in other works for DP steels [69-71, 73] and single phase aluminum alloys [74, 75]. However, a comparison of deformation maps for Q&P intercritically annealed processed steels [20] and DP steels [69-71, 73] with those for the Al based metal matrix composites (MMCs) reinforced with ceramic particles [74, 76] shows more significant strain partitioning in the MMCs. This is due to much higher difference in Young's modulus and mechanical strength of phase microconstituents.

It is, hence, clear that in multiphase AHSSs, including Q&P steels, the difference in mechanical properties of individual phases may lead to inhomogeneous local plastic deformation behavior [12, 34, 52, 55]. Nevertheless, variations in the local microstructural architecture, i.e., disparity in size, shape, orientation and spatial distribution of individual microconstituents within the multiphase Q&P steel grade can significantly affect strain partitioning during plastic deformation, as well. It should be also taken into consideration that transformation of the RA may also lead to increased strain hardening in these AHSSs if the TRIP effect is operating [15, 77, 78], so the volume fraction and stability of RA strongly affect mechanical properties of Q&P steels [60, 77, 79, 80].

1.4. Stability of retained austenite during plastic deformation and its effect on mechanical properties

According to Section 1.2, the common feature of all Q&P processed steels is that a considerable volume fraction of RA remains stable after the last quench to room temperature. As a result, it is reasonable to believe that the excellent ductility of these advanced high-strength steels may be determined to some extent by the combination of a strong matrix (TM and UM) and the presence of RA grains in the final microstructure [81, 82].

The stability of RA refers to its resistance to transformation with stress, strain as well as with temperature [83, 84]. It is well known for TRIP steels that not only the volume fraction of RA, but also its transformation stability plays an important role in determining mechanical properties [60, 77, 79, 80]. This transformation provides a localized work hardening effect, that delays the onset of local necking and provides improved elongation [83]. Besides, the local increase in specific volume caused by the TRIP effect can help to close propagating cracks. In fact, mechanical properties (strength and ductility) and mechanical behavior (strain hardening) of Q&P steels have also been reported to depend on their microstructure [20, 21, 52, 53, 66, 85]. As is shown in literature, the mechanical stability of individual RA grains is determined by a complex interplay of microstructural parameters [86], among others the local carbon concentration in the RA grains [84, 87-90], the RA grain size [88, 91], the constraining effect of the surrounding phases [21, 83, 92], the morphology of the RA grains [77, 93, 94] and their orientation [90, 95], which are considered more in detail in the subsections below.

During the initial stages of tensile plastic straining in Q&P steels, the local plastic deformation is mainly accommodated in the TM and RA grains. Once the critical strain stage for austenite has been reached, the RA grains transform, thereby reducing the local internal strains in the TM grains. In the last stages of deformation, strain accommodation processes in the TM and UM microconstituents take place, along with the TRIP-effect in the RA [86] and the latter becomes dominant to the former with increasing strain [86].

1.4.1. Grain size of the retained austenite

In [91] the effect of a thermal load on the stability of RA was assessed. Three different forms of transformation behavior were observed. Most of the austenite

grains completely transformed into martensite in a single step. However, a few showed an incomplete transformation, where only part of the austenite grains transformed into martensite. Finally, a significant amount of austenite grains did not show any transformation at all. Accordingly, the authors found a minimum RA grain size below which the martensitic transformation does not occur [91]. In addition, in [88] only smaller austenite grains have been reported to be successfully retained at room temperature for short bainitic holding times, since bigger grains were too unstable and did transform into martensite even above room temperature [88]. Smaller grains of RA have been found to be more stable against deformation due to a resultant lowering of the M_s and a decrease in the number of nucleation sites in each grain [92, 96].

During straining of Q&P steels, the average RA grain size has also been reported to decrease [86]. Largest grains have been described to transform rapidly and therefore they only contribute to strain hardening in the initial stages of the tensile test. On the contrary, smallest grains can sustain plasticity at larger strains, due to their high stability. For this reason, smallest RA grains contribute most during the TRIP effect in the last stages of plastic elongation [20, 86]. Partial transformation of austenite grains has also been observed in Q&P steels during tensile testing [86].

1.4.2. **Morphology of the retained austenite**

Another parameter that determines the RA transformation stability is its morphology. In the case of TRIP steels, RA was observed to exist in different morphologies, such as the blocky morphology [77, 88], as thin layers between martensite laths (film-like type) [77, 88, 96] or in a thicker interlath-lamellar shape [97]. As proved in [98], different morphologies of RA provide different mechanical stabilities [94]. The largest "blocky type" austenite grains usually show a relatively low mechanical stability during tensile testing [84, 98]. The interlath-lamellar type shows intermediate stability and steadily transforms throughout the entire test, whereas the film-like type has been reported to be the most resistant morphology against transformation [98]. In addition, interlath-lamellar RA grains with a large aspect ratio between width to length have been reported to be less stable compared to other grains with inferior aspect ratio values [86].

1.4.3. **Local carbon concentration in the retained austenite**

Another factor that affects the stability of RA is the local concentration of stabilizing alloying elements. The most important stabilizing element in low-alloy TRIP-assisted steels is carbon [99]. Therefore, the strain level at which RA begins to transform to martensite can be controlled by adjusting the local carbon content. At lower carbon levels, the RA begins to transform almost immediately upon deformation, increasing the work hardening rate and formability of the material. At higher carbon contents, the RA seems to be more stable and begins to transform only at higher strain levels [7]. However, the mechanical stability of RA grains depends simultaneously on the carbon content, the grain orientation and the grain size [84]. This was confirmed in [88], where only austenite grains with a combination of a small size and a high carbon content were stable enough not to transform into martensite. On the other hand, in [91] the austenite grains with the lowest carbon content and the highest grain volume were found to show the lowest stability against martensitic transformation.

Furthermore, the differences of RA volume fraction and carbon content between measured values in Q&P steels and the CCE model predicted values are mainly attributed to the different grain size of the austenite formed in the first quenching process and the different carbon partitioning behaviors during the partitioning step [82]. During plastic deformation of Q&P steels, the overall C-content of the more stable RA grains is observed to increase, due to transformation of RA grains with low C-concentrations [66]. Intrinsic to the slow C-diffusion in austenite [85], larger grains are generally linked with lower C-contents compared to the smaller counterparts with higher C-contents. This can be observed as well as from their partial transformation to UM due to incomplete stabilization during partitioning [82]. Therefore, the effect of low C-content in large austenite grains reinforces the influence of grain size on its transformation stability. Recent investigations revealed, however, that stabilized blocky RA grains were enriched more in C than their thin film-like counterparts [26, 77], which combined with the fact that larger, blocky RA grains transform at lower strains [80] would suggest that size and morphology are strong determining factors in controlling the RA stability [86]. On the contrary, if smaller film-like austenite grains have lower C-contents than the larger, blocky RA grains [26, 77], then the combined effect of grain size and morphology on RA stability may exceed that of the C-content [86].

1.4.4. Constraining effect of the surrounding phases

RA grain stability has also been reported to depend on the resistance to plastic flow of the surrounding microstructure [84], as one of the most complex contributions to the RA stability comes from the interaction of the austenite with its surroundings. The mechanical properties of the surrounding matrix affect the stress and strain carried by the austenite at a given total strain level, as it would do in a composite material [83]. Consequently, the size, shape and composition of the phases located in the environments of the RA grains play a major role in the global level of strain required for transformation [83, 84, 86]. The resulting "apparent" stability of RA will, thus, depend not only on the austenite properties but also on the properties of the other phases [92]. During straining, this effect is enhanced in the case of multiphase steels due to the induced stress and strain partitioning (Section 1.3.3). For instance, when the austenite phase is surrounded by soft ferrite, it experiences more of the global stress and strain than if it would be surrounded by a harder phase [100]. On the other hand, the presence of a hard phase such as martensite or bainite around the interlath-lamellar RA introduces hydrostatic pressure and enhances the stabilization of RA, by decreasing its local M_s temperature [93].

Particularly in Q&P processed steels, UM was reported [21] to play a significant role in:

- The strain distribution in the microstructure by inhibiting the amount of deformation that could be accommodated in the TM matrix.
- The fracture mechanism by triggering void formation

Hence, in Q&P steels, the UM microconstituent has a constraining effect on the strain accommodation processes which decreases the austenite transformation stability [21, 86].

1.4.5. Orientation of the retained austenite

The dependence of the austenite crystallographic orientation on its stability is defined by the theory of martensite crystallography. This theory describes the influence of the crystallographic orientation on the austenite transformation stability. Austenite grains with a high transformation potential should have a low crystallographically based transformation stability [86].

In the initial deformation stages, grains with their longest axis at an angle of ± 45° have reported to be the less stable of all the orientations during tensile loading [86].

Tensile deformation is usually accommodated by dislocation slip which begins when the critical value of the shear stress on the slip plane is reached [101]. The shear stress is maximum at an angle of 45° with respect to the loading axis. For this reason, the grains oriented with their longest axis parallel to this direction experience the highest shear component, and as a result, transform first [86]. Then, due to the depletion of the ± 45° oriented austenite grains, the strain in the subsequent deformation steps is accommodated mainly by the transformation of the austenite grains having long axes parallel and perpendicular to the tensile axis [86].

Subsequent to deformation and transformation, the RA grains rotate to accommodate part of the imposed plastic straining. Orientations with high transformation potentials transform to martensite instead of rotating significantly. In contrast, orientations with low transformation potentials rotate in the range between 2° to 6° prior to the transformation [86]. These rotations may act as a barrier to the movement of dislocations inside the martensite grains, and hence reduce the back-stress on dislocations and postpone crack initiation processes [101].

1.5. Fracture behavior of Q&P steels

Fracture can be defined as the separation or fragmentation, of a solid body into two or more parts under an applied stress. In materials science, fracture toughness is the property that describes the ability of a material containing a crack to resist fracture. It also is one of the most important properties of any material for many design applications [101].

The process of fracture can be considered to be made up of two components, crack initiation and crack propagation. Macroscopically, fracture can be classified into two general categories: ductile and brittle fracture, depending on the stable or unstable character of crack propagation, respectively. A ductile fracture is characterized by appreciable plastic deformation prior to and during the propagation of the crack. An appreciable amount of gross deformation is usually present at the fracture surfaces. On the contrary, brittle fracture in metals is characterized by a rapid rate of crack propagation, with no gross deformation and very little micro-deformation [102]. Microscopically, three of the most common fracture mechanisms in metals and alloys are schematically presented in Figure 1-7. Ductile materials (Figure 1-7 (a)) usually fail as the result of nucleation, growth and coalescence of microscopic voids that initiate from various internal free surfaces [102]. However, the ductile crack growth resistance is usually not only determined by the nucleation process of voids. The

plastic energy is also needed for their linking, which is controlled by other microstructural factors [103]. Cleavage fracture (Figure 1-7 (b)) involves separation along specific crystallographic planes. The major characteristic of cleavage is the orientation relationship between the plane of the crack and the crystal structure through which the crack passes. This orientation relationship causes the several microscopic fracture features usually associated with cleavage, the most evident being the flatness of facets and the cleavage steps [104]. Inter-granular fracture (Figure 1-7 (c)), as its name implies, occurs when grain boundaries are the preferred path in the material [102]. In many cases, especially in the case of multiphase materials, attention must be paid to the inhomogeneity of the fracture surface. Mixtures of different failure mechanisms are expected in such cases [104].

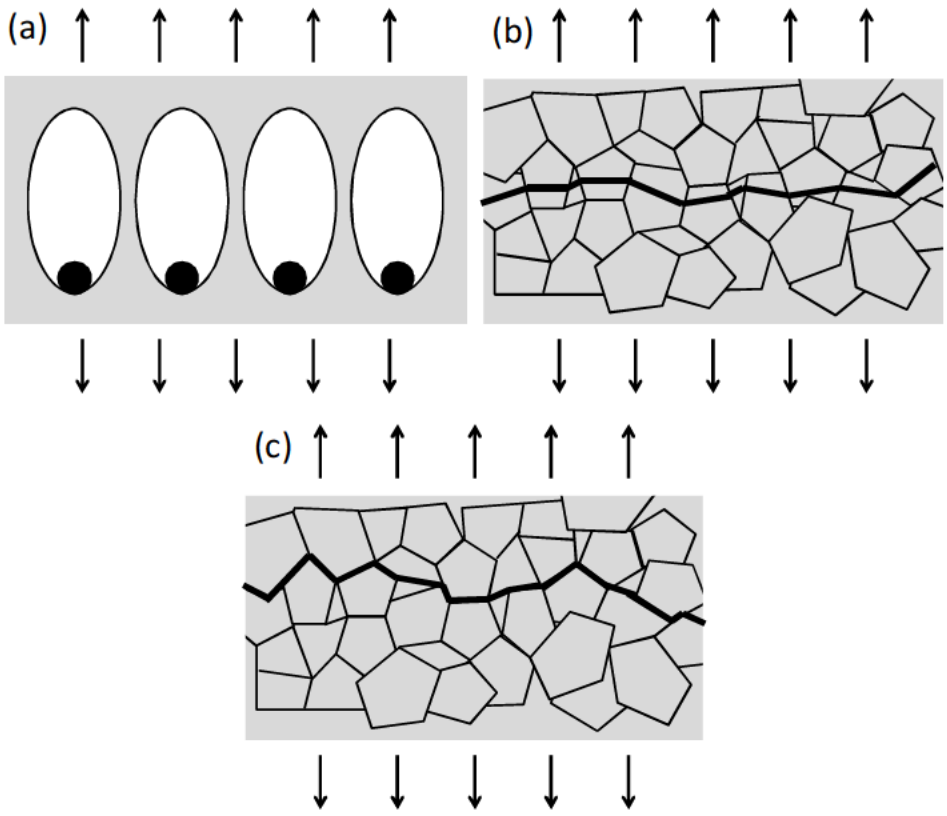

Figure 1-7. Schematic representation of three micro-mechanisms of fracture in metals: (a) ductile fracture, (b) cleavage and (c) inter-granular fracture. Re-plotted from [102].

In spite of the growing interest to the Q&P processed steels, the research on fracture behavior of these steel grades very limited. There is only one work published by R. Wu *et al.* [105]. Despite their results are questionable, the authors claim that the stability of RA determines the toughness of Q&P-treated sheet steels containing appreciable amount of RA, due to the TRIP effect. Besides, TRIP effect occurring on

less stable RA grains further improves the toughness of Q&P steels [105]. On the contrary, the fracture resistance of DP steels [106, 107] and TRIP-aided steels [108-110] has already been systematically investigated by several authors. Some authors have reported that in both DP and TRIP steels, the damage process starts by cracking of the interphase between hard phases and the ferrite matrix [110]. In such composite materials consisting of mixtures of brittle and ductile components the most important influence factor for the crack growth resistance is the arrangement of the brittle and ductile domains, and not the volumetric fraction of the components. The toughest arrangement is that of isolated brittle domains surrounded by a network of ductile components [107]. Then, the coalescence of voids nucleated on second phases dictates the crack path [110]. It has also been reported that the TRIP effect can significantly improve the fracture resistance, by bringing additional work-hardening capacity in the neck zone developing in front of the propagating crack [110, 111]. In addition, in DP steels grain refinement has been reported to promote ductile fracture mechanisms. The formation of martensite cracks and cleavage fracture in ferrite is suppressed in the fine grained steels due to the small size, the more homogeneous distribution and more spherical shape of martensite islands [112, 113]. The same tendency has been reported for the hard martensite microconstituent in TRIP-assisted steels: martensite will not crack easily if its size is reduced below a critical value [111].

Therefore, it seems clear that it is essential to determine and understand the relationship between local fracture properties and local microstructure of Q&P processed steels, since manipulation of the microstructure can lead to further improvement of the global fracture properties.

1.6. Effect of microstructure on cyclic behavior of Q&P steels

It has been recognized since 1830 [101] that a metal subjected to a repetitive or fluctuating stress will fail at a much lower stress than that required to cause fracture on a single application of load. Failures that occur under conditions of dynamic loading are called fatigue failure. Therefore, the fatigue behavior of a component can be defined as its ability to resist degradation during a series of repetitive loads. Three basic factors are necessary to cause fatigue failure [101]:

- A maximum stress of sufficiently high value.
- A large enough variation or fluctuation in the applied stress.
- A sufficiently large number of cycles of the applied stress.

As it is well known, fatigue failure proceeds in three distinct stages [101]:

- Crack initiation in the areas of stress concentration (near stress raisers).
- Stable fatigue crack propagation in direction normal to maximum tensile stress.
- Unstable crack growth and ultimate ductile failure, which occurs when the crack reaches sufficient length, so that the remaining cross section cannot withstand the applied load.

While the development of the Q&P steels often focuses on microstructural characterization [12, 20, 21, 53, 66] and on the improvement of mechanical strength and ductility [20, 21], it is also vital to understand the fatigue behavior and impact of cyclic loading on the microstructure of these materials to ensure good performance in service. On the other hand, the effect of RA on the fatigue behavior of AHSSs has been a controversial issue for long time. Some authors have reported that in the case of steels with high volume fraction of RA, its transformation into martensite under certain number of cycles will accelerate crack propagation and therefore decrease fatigue life [114-118]. In such cases, the newly formed martensite may provide a path for fast crack propagation [10]. On the contrary, in a number of other studies, the improvement in fatigue life for multiphase steels with RA was associated with the transformation of RA to martensite in front of the crack tip [10, 119, 120] due to the crack closure effect [121]. This transformation is triggered by the strain energy in front of the crack tip and has been linked with a delay of crack initiation, as well as retardation of stage I of crack propagation [117]. Consequently, while it is evident that RA typically transforms in front of a propagating crack tip, the impact of RA on fatigue performance is not clear [10]. In addition, the fatigue life of DP steels has been recently reported to be connected to the martensite volume fraction, and it is significantly reduced by an increase in the volume fraction of the hard phase [122]. Therefore, it is essential to gain fundamental understanding of microstructure - fatigue behavior relationship in multiphase AHSSs, as cyclic loading constitutes one of the major causes for failure of auto parts. It should also be noted that research on the fatigue behavior of Q&P steels is very limited [11], and no studies on mechanisms of fatigue crack initiation and propagation have been carried out so far.

2 Motivation and objectives

2. MOTIVATION AND OBJECTIVES

There are several important challenges that have to be overcome before Q&P processed steels can replace the current DP and TRIP assisted-steels in many applications. There are currently a lot of reports on microstructure, strength and ductility of Q&P steels. While much progress has been made, the field provides rich opportunities for further understanding and development. There is no systematic study where the effect of Q&P parameters on microstructure and tensile properties along with fatigue and fracture behavior, is analyzed. A requirement for further improvement of mechanical properties via intelligent microstructural design is, thus, to achieve fundamental understanding of the processing - property - microstructure relationships in this type of steels.

Therefore, the main goal of this work is to develop a concept of microstructural design in Q&P steels to improve a wide range of mechanical properties, as well as to relate them with microstructure (phase composition, size of microconstituents, carbon content in RA, *etc.*) and Q&P parameters. The following partial objectives can be derived from the previous general one:

- To relate the micromechanics of the deformation of a Q&P steel grade with its phase composition, Q&P processing conditions and mechanical properties of its individual phases.
- To study the effect of microstructure on fracture behavior of Q&P steels. The study of crack propagation conditions and the knowledge of the relations between microstructural parameters, failure micro-mechanisms, and the processes which enhance the formation of fracture surfaces may play a key role in this issue and hence will be thoroughly discussed in this study.
- To explore the effect of microstructure on fatigue properties of Q&P steels and the role of RA in their cyclic behavior.

3 Experimental procedures

3. EXPERIMENTAL PROCEDURES

This chapter details the basis of the main materials and techniques used in this work. Justification for the choice of the selected chemical compositions is provided, along with the description of the Q&P processing routes applied to the materials. The experimental methods and techniques used for the microstructural and mechanical characterization are described in detail. For this purpose, the facilities used in this investigation are briefly introduced.

3.1. Materials and processing

As described in Section 1.3.1, three main requirements were considered in order to select the appropriate chemical composition [30, 85]:

- avoiding ferrite, pearlite or bainite during quenching and bainite during partitioning.
- suppressing carbide precipitation during partitioning.
- stabilizing the austenite during final quenching.

The effect of appropriate alloying elements is of great importance on this issue. Mn is effective in fulfilling the first requirement [123]: it has been demonstrated that Mn can be utilized for stabilization of retained austenite at room temperature [24, 57-59]. However, high Mn concentrations result in segregation banding, and therefore, the Mn content was limited to 3 wt. % [124]. Besides, during Q&P processing, any transition carbide precipitation diminishes the potential for carbon enrichment of austenite. It is known that cementite formation can be eliminated or suppressed through additions of Si, and also that Al can produce a similar effect [16, 23, 41]. According to literature [59, 72], around 2 wt. % Si is sufficient to suppress cementite formation during partitioning, since it changes the carbide precipitation kinetics from carbon diffusion control to silicon diffusion control, away from the carbide interface [45, 85]. Finally, Cr can enhance the response to heat treatment. When Cr is used in conjunction with Mn, the critical quenching speed is reduced and therefore hardenability is improved [125-127]. However, Cr content should be controlled in order to avoid the formation of stable hard carbides [125-127]. For this reason, the Cr content was limited to 0.15 wt. %. The carbon content was chosen

between 0.25 and 0.3 wt. % so as to ensure austenite stability [24]. As it was reported in [85], different concentrations of these elements influence the time temperature transformation diagram [128]. Increasing the Mn concentration from 2.5 to 3 wt. % shifts the ferrite/pearlite transformation to the right and decreases the bainite onset temperature. The influence of increasing the carbon content from 0.25 to 0.3 wt. % is similar; however, the effect is less pronounced [85].

Based on the above, steel grades with the nominal composition presented in Table 3-1 were chosen as materials for this investigation.

Table 3-1. Chemical composition of the studied steel grades (wt. %).

Specimen	C	Si	Mn	Al	Cr
QP-0.25	0.25	1.5	3	0.023	0.015
QP-0.28	0.28	2	2.5	0.03	0.15

Thermodynamic calculations were performed in order to evaluate the phase equilibrium diagram for the selected chemistries using the Thermo-Calc® Software (Thermo-Calc Software, Stockholm, Sweden) in combination with the TCFE5 database (Thermo-Calc Software, Stockholm, Sweden) [129]. As it was predicted, the addition of the selected alloying elements results in the stabilization of the γ-field for both compositions (see Figure 3-1).

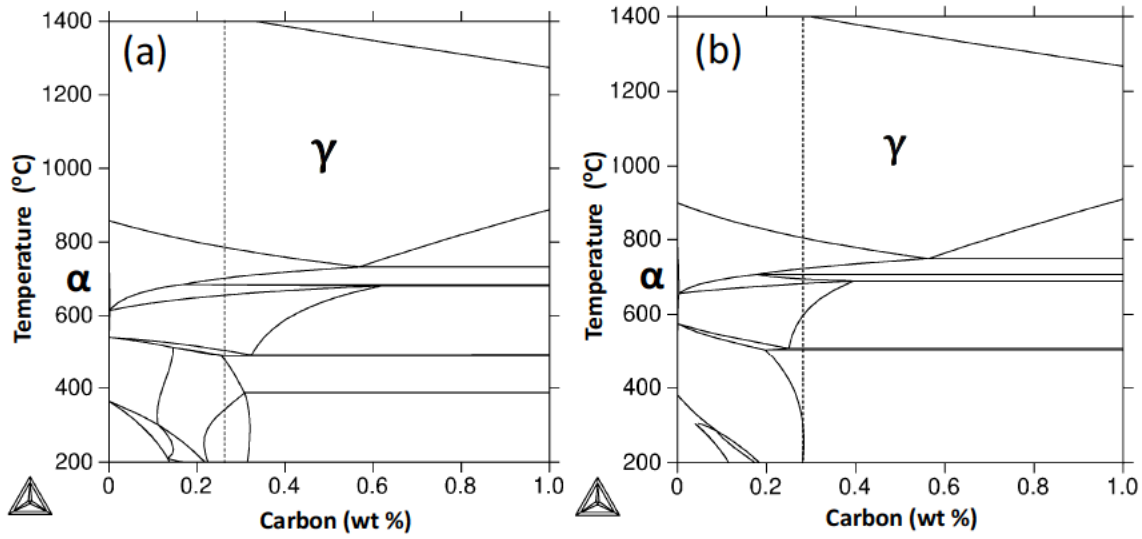

Figure 3-1. Equilibrium phase diagram calculated by Thermo-Calc® of the chemistries shown in Table 3-1, expressed as a function of the percentage of C: (a) QP-0.25 and (b) QP-0.28.

The materials were cast in a laboratory vacuum induction furnace. After casting, the steel slabs were hot rolled to a final thickness of 2.5 mm, accelerated cooled by water jets to 600°C and transferred to a furnace for coiling simulations at 560°C. The hot rolled plates were pickled and cold rolled to a thickness of 1 mm imposing a total reduction in thickness of 60 %. The obtained strips were cut and subsequently subjected to Q&P heat treatment cycles. Smaller strips were processed in the thermo-mechanical simulator Gleeble™ 3500 (Dynamic Systems Inc., Poestenkill, NY, USA), whereas bigger ones were processed in a reactive annealing process simulator. The specimens were heated to 850°C, above the A_{c3} temperature (see Figure 3-1), for full austenitization. Then, they were quenched to varying QT at a quenching rate of 20°Cs^{-1} in order to obtain microstructures consisting of martensite and austenite, and to completely avoid bainite formation [85]. After that the samples were reheated with a heating rate of 10°C s^{-1} and kept isothermally at different PTs for varying Pts. Final quenching to room temperature was also performed with a cooling rate of 20°C s^{-1}. The Q&P processing parameters applied to the studied steel grades are summarized in Table 3-2, where the labeling of the samples is also indicated. The QP-0.28-1 and the QP-0.28-2 samples underwent heating to a peak PT of 280°C and 450°C, respectively. The materials used in the present investigation were provided by Ghent University of Technology (Belgium), Arcelor Mittal Global R&D Gent (Belgium) and ThyssenKrupp Steel Europe AG (Germany), respectively.

Table 3-2. Q&P processing parameters applied to the studied steel grades.

Specimen		QT (°C)	PT (°C)	Pt (s)
QP-0.25-	1	224	350	500
	2	244	300	500
	3	244	350	500
	4	244	400	100
	5	244	400	500
	6	244	400	1000
	7	264	350	500
QP-0.28-	1	280	280	-
	2	240	450	-

Formulas having an exponential carbon dependence were considered in the calculation of theoretical martensite start temperature (M_S), according to the work of van Bohemen [130]:

$$M_S = 565 - \sum K_i \cdot x_i - 600 \cdot (1 - e^{-0.96 \cdot X_c}) \quad \textbf{(Eq. 3-1)}$$

with,

$$\sum K_i \cdot x_i = 31 \cdot x_{Mn} + 13 \cdot x_{Si} + 10 \cdot x_{Cr} + 18 \cdot x_{Ni} + 13 \cdot x_{Mo} \quad \textbf{(Eq. 3-2)}$$

And describes how substitutional elements influence M_s. On the other hand, M_f was determined by means of dilatometer experiments for the two studied compositions [85]. Results of the M_s and M_f calculation are summarized in Table 3-3, respectively.

Table 3-3. Estimated martensite start temperature (M_s) and martensite finish temperature (M_f) for the studied compositions.

Specimen	M_s (°C)	M_f (°C)
QP-0.25	325	≈200
QP-0.28	319	≈200

The optimum QT within the M_s and martensite finish M_f temperature range was then pursued, in order to maximize the final volume fraction of RA [85]. The subsequent partitioning stage consisted of reheating the partially quenched steel to the PT and isothermal holding, for the carbon diffusion from the martensite into the untransformed austenite [85]. Regarding the QP-0.25 chemistry, the lowest PT was selected in order to ensure the dissolution of ε carbides [23, 123], whereas the upper limit of the PT was set at 400°C to minimize competing reactions such as decomposition of the austenite into ferrite and coarse carbides [123], carbide precipitation [131] or decomposition of austenite to bainite [85]. Varying Pts for the different PTs were selected. On the other hand, for the QP-0.28 composition, all these requirements were also taken into consideration. However, in this case the focus of interest was set on the effect on the final microstructure of the one step Q&P processing route (QP0.28-1) and the ramping partitioning (QP0.28-2) to a slightly superior PT.

Both the optimization of the Q&P processing route as well as the production of the Q&P processed strips were performed by Ghent University of Technology (Belgium),

Arcelor Mittal Global R&D Gent (Belgium) and ThyssenKrupp Steel Europe AG (Germany).

3.2. Microstructural characterization

3.2.1. X-ray diffraction (XRD)

X-rays are electromagnetic radiation with typical photon energies in the range of 100 eV - 100 keV. For diffraction applications, only short wavelength X-rays (hard X-rays) in the range of a few angstroms to 0.1 Å (1 keV - 120 keV) are used. Because the wavelength of X-rays is comparable to the size of atoms, they are ideally suited for probing the structural arrangement of atoms and molecules in a wide range of materials. The energetic X-rays can penetrate deep into the materials and provide information about the bulk structure [132-134].

X-rays are usually produced by X-ray tubes. In a X-ray tube, which is the primary X-ray source used in laboratory X-ray instruments, X-rays are generated when a focused electron beam accelerated across a high voltage field bombards a stationary or rotating solid target. As electrons collide with atoms in the target and slow down, a continuous spectrum of X-rays are emitted, which are termed "Bremsstrahlung" radiation. The high energy electrons also eject inner shell electrons in atoms through the ionization process. When free electrons fill the shell, a X-ray photon with energy characteristic of the target material is emitted. Common targets used in X-ray tubes include Cu and Mo, which emit 8 keV and 14 keV x-rays with corresponding wavelengths of 1.54 Å and 0.8 Å, respectively [132-134].

X-rays primarily interact with electrons in atoms. When X-ray photons collide with electrons, some photons from the incident beam will be deflected away from the direction where they originally travel. If the wavelength of these scattered X-rays did not change (meaning that X-ray photons did not lose any energy), the process is called elastic scattering (Thompson Scattering) in that only momentum has been transferred in the scattering process. These are the X-rays that are measured in diffraction experiments, as the scattered X-rays carry information about the electron distribution in materials. On the other hand, in the inelastic scattering process (Compton Scattering), X-rays transfer some of their energy to the electrons and the scattered X-rays will have different wavelength than the incident X-rays. Diffracted waves from different atoms can interfere with each other and the resultant intensity distribution is strongly modulated by this interaction. If the atoms are arranged in a

periodic manner, as it happens in crystals, the diffracted waves will consist of sharp interference maxima (peaks) with the same symmetry as that in the distribution of atoms. Measuring the diffraction pattern allows to deduce the distribution of atoms in a material [132-134].

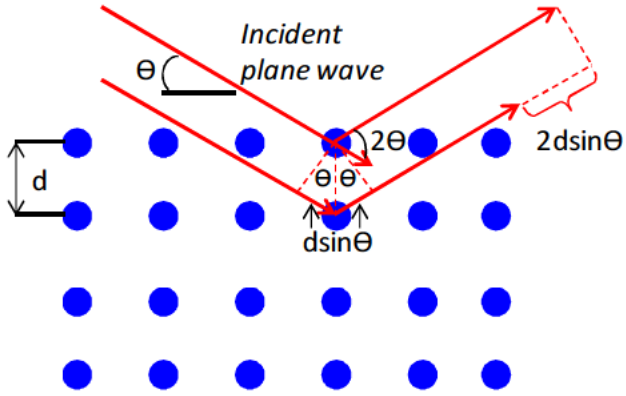

Figure 3-2. Constructive interference in Bragg's law [135].

The peaks in a X-ray diffraction pattern are directly related to the atomic distances. An incident X-ray beam interacts with the atoms arranged in a periodic manner, as shown in Figure 3-2. The atoms, represented as spheres in the graph, can be viewed as forming different sets of planes in the crystal. For a given set of lattice planes with an inter-plane distance of *d*, the condition for a diffraction (peak) to occur can be simply written as [132-134]:

$$2dsin\theta = n\lambda \qquad \textbf{(Eq. 3-3)}$$

which is known as Bragg's law [135]. In the equation, λ is the wavelength of the X-ray, θ the scattering angle, and *n* an integer representing the order of the diffraction peak. Bragg's Law is one of most important laws used for interpreting X-ray diffraction data [132-134].

In the present study, the volume fractions of RA and its average carbon content at room temperature were measured by XRD experiments performed on a Siemens Kristalloflex D5000 diffractometer (Bruker Corporation, Coventry, United Kingdom) equipped with a Mo-Kα source operating at 40 kV and 40 mA. A 2θ-range of 25° to 45° was scanned using a step size of 0.01°, dwell-time of 2 s and a rotation speed of 15 rpm. The data were post-processed by subtracting the background radiation and $K\alpha_2$ influence. The volume fractions of RA were determined by the Cullity formula [133], and the austenite lattice parameter was determined from the extrapolation function of the lattice parameter a_γ vs. $\cos^2(\Theta)/\sin(\Theta)$ of the (200),

(220) and (311) austenite peaks [59, 136]. The carbon concentration X_C was obtained according to the procedure proposed in [21, 59] where the link between the lattice parameter of the austenite is presented as:

$$a_\gamma = 0.3556 + 0.00453 \cdot X_C + 0.000095 \cdot X_{Mn} + 0.000563 \cdot X_{Al} \quad \textbf{(Eq. 3-4)}$$

where a_γ is the austenite lattice parameter in nm and X_C, X_{Mn} and X_{Al} are the concentrations of carbon, manganese and aluminum in austenite in wt. %. Volume fractions of TM and UM were estimated from Orientation Imaging Micrograph (OIM) images using the free ImageJ software [137].

3.2.2. Scanning electron microscopy (SEM)

Scanning electron microscopy (SEM) can be defined as a microscopy technique that uses electrons instead of light to form an image. Since its development in the early 1950's, the SEM has been a powerful instrument widely used in materials science [6]. In SEM, a beam of electrons is produced by the electron gun. Then, it is focused on a specimen and scanned along a pattern of parallel lines. The purpose of the electron gun is to provide a stable beam of electrons of adjustable energy, which is held within vacuum. The beam travels through electromagnetic fields and lenses, which focus the beam down towards the sample. Once the beam hits the sample, electrons and X-rays are ejected from the sample. Various signals are generated as a result of the impact of the incident electrons: secondary electrons, high-energy backscattered electrons and characteristic X-rays (Figure 3-3). Detectors collect these X-rays, backscattered electrons, and secondary electrons and convert them into a signal that is sent to a screen in order to produce the final image [138]. Useful information can be obtained from the interaction between electrons and sample surface, such as the surface topography, composition and crystallography.

Specimens for microstructural characterization were ground and polished to a mirror-like surface using standard metallographic techniques. For SEM characterization, specimens were etched with 2 vol. % HNO_3 in ethanol (nital 2 %) solution. Examination of the microstructure was performed using a SEM EVO MA15 (Carl Zeiss, Oberkochen, Germany) operating at an accelerating voltage of 20 kV.

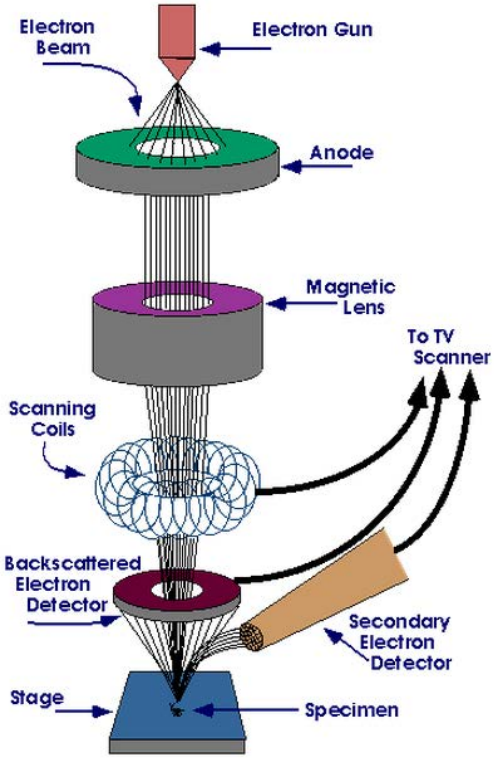

Figure 3-3. SEM schematic view [138].

3.2.3. Electron backscatter diffraction (EBSD)

Electron backscatter diffraction (EBSD) is a SEM based technique very useful for microstructural characterization and analysis of crystalline materials [139, 140]. It allows the micro-texture [141], grain and phase boundary characterization [142, 143], phase identification [144] and strain determination [145] in crystalline materials of any crystal structure.

The heart of the EBSD technique is the indexation of diffracted patterns, that are obtained by focusing an electron beam on a crystalline sample. The sample is usually oriented at 70° (see Figure 3-4) with respect to the horizontal plane which allows more electrons to be scattered and to be registered by the detector [139]. The electrons disperse beneath the surface, subsequently diffracting among the crystallographic planes [135], according to Bragg's law [135]. The diffracted signal is collected and viewed via a low-light video camera interfaced to a phosphor screen [140]. If the sample produces good diffraction patterns, orientation determination is a three step process consisting of (i) Kikuchi band detection, (ii) Kikuchi band identification and (iii) determination of orientation. In the first step, Kikuchi band detection is carried through Hough Transform [146, 147], by converting Kikuchi lines from recorded image into single points in the Hough space. In the second step,

Kikuchi band identification is related to correct identification of the particular lattice plane associated with the reconstructed Kikuchi band. The width of detected bands is a function of the spacing of diffracting planes (Bragg's law) and is compared with a theoretical list of diffracting lattice planes. Additionally, the angles between bands have to be determined and compared with theoretical values. This is done by comparison with a stored table in the database consisting of all interplanar angles between the low Miller indices [148] planes (hkl) present in the crystal structure, including every individual plane in the family of planes {hkl}. In the third step, orientation determination is based on the calculation of the orientation of the corresponding crystal lattice with respect to the reference frame [139].

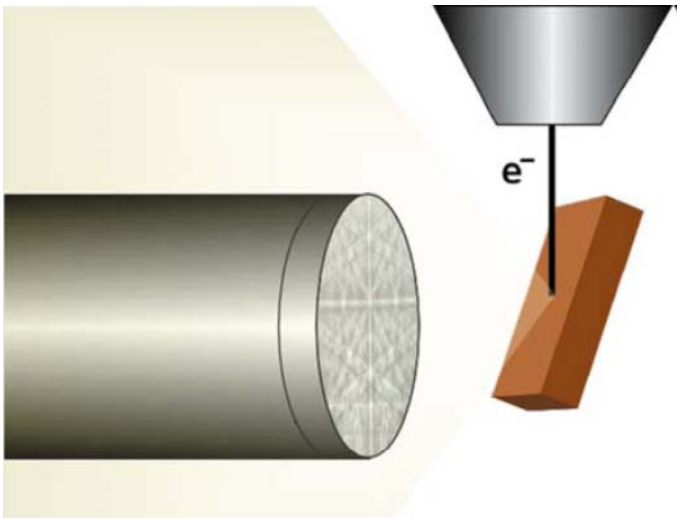

Figure 3-4. Schematic representation of the typical EBSD geometry, showing the pole piece of the SEM, the electron beam, the tilted specimen, and the phosphor screen [149].

The diffraction patterns provide crystallographic information that can be related to their origin position in the specimen. Evaluation and indexing of the diffraction patterns is performed in most cases automatically and the data is output in a variety of both statistical and pictorial formats. The most versatile and revealing of these outputs is the OIM map which is a quantitative depiction of an area of the microstructure in terms of its crystallographic constituents [140]. One common map constructed from EBSD data is the image quality (IQ) map. In such cases, electrons are diffracted from near the surface of the sample and the IQ can be considered as a metric describing the quality of a diffracted pattern. An IQ map is constructed by mapping the IQ value measured for each diffraction pattern obtained during an OIM scan to a gray or color scale. Both the "perfection" of the crystal lattice and the atoms present within the diffracting volume affect the IQ [139, 150]. Therefore, IQ

provides useful complementary information about these features to the indexed crystallographic orientations [150].

Optimum specimen preparation is a fundamental requirement for an EBSD experiment. Inadequate specimen preparation will result in degraded diffraction patterns which feed through loss of data quality [140]. In this work, specimens for EBSD analysis were prepared using standard metallographic techniques with final polishing with OP-U (colloidal silica) for 40 minutes. Due to low availability reasons, Orientation imaging microscopy (OIM) studies were performed using two different equipments: first, a FEI Quanta™ 450 FEG-SEM (FEI Corporate, Oregon, USA) equipped with a Hikari detector controlled by the EDAX-TSL OIM-Data Collection (version 6.2®) software (EDAX, Mahwah, USA). The data were acquired at an accelerating voltage of 20 kV, a working distance of 16 mm, a tilt angle of 70° and a step size of 40 nm. The orientation data were post-processed with TSL-OIM Analysis 6.2© software (EDAX, Mahwah, USA). Secondly, a FEI Quanta™ Helios NanoLab 600i (FEI Corporate, Oregon, USA), equipped with a NordlysNano detector controlled by the AZtec Oxford Instruments Nanoanalysis (version 2.4®) software (Oxford Instruments, Abingdon, United Kingdom) was used. The data were acquired at an accelerating voltage of 18 kV, a working distance of 10 mm, a tilt angle of 70° and a step size of 55 nm. The orientation data were post-processed with HKL Post-processing Oxford Instruments Nanotechnology (version 5.1©) software (Oxford Instruments, Abingdon, United Kingdom).

Data clean-up routines can compensate in part for unsolved patterns [140]. The post processing of the raw orientation data can be described as follows. First, a IQ standardization with a minimum grain size of 4 pixels was applied. This clean up algorithm changes the IQ of all points in a grain to the maximum IQ found among all points belonging to that grain. Afterwards, the neighbor IQ correlation algorithm was employed, which implies that if a particular point has v below 0.1, then the IQ of the nearest neighbors are checked to find the neighbor with the highest IQ. The orientation and IQ of the particular point are reassigned to match the orientation and IQ of the neighbor with the maximum IQ. Finally, if the majority of neighbors of a particular grain smaller than 4 pixels with a grain tolerance angle of 5° belong to the same grain, then the orientation of the particular grain is changed to match that of the majority grain, i.e. a grain dilation algorithm was applied [95]. It should be noted that clean-up procedures must never be used as an alternative to obtaining the best and most representative diffraction patterns [140].

3.2.4. Representation of textures

Most of engineering materials are polycrystalline in nature. In such cases, microstructure can be considered as the combination of morphology and orientation of the constituents [151]. The orientation changes that take place during deformation, such as rolling, are not random. They are a consequence of the fact that deformation occurs on the most favorably oriented slip or twinning systems and it follows that the deformed metal acquires a preferred orientation or texture. If the metal is subsequently recrystallized, nucleation occurs preferentially in association with specific features of the microstructure. The ability of the nucleus to grow may also be influenced by the orientations of adjacent regions in the microstructure. Together these features, nucleation and growth, ensure that a texture also develops in the recrystallized metal [152]. Texture can thus be defined as the arrangement of building blocks in the polycrystalline material [151].

A remarkable feature of EBSD microscopy, is that microstructural design is dramatically enhanced in order to control the materials properties, by providing extensive crystallographic orientation information of a given two-dimensional section of a microstructure. In this sense, EBSD measures the discrete crystallographic orientations of volume elements arranged in a regular manner on the surface of the material [149].

The purpose of texture representation is to preferentially examine the orientation of the crystallites without concern for their spatial characteristics, e.g., their arrangement, size and morphology. Therefore, the analysis of material texture begins with the correct definition of the sample orientation [149]. The axes of the sample or specimen coordinate system are chosen according to important surfaces or directions associated with the external form or shape of the specimen. For example, for a manufactured material there are obvious choices defined by the processing geometry. One of the most common of these relates to a rolled product, and hence the directions associated with the external shape are the rolling direction (RD), the through-thickness direction, i.e. the direction normal to the rolling plane (ND) and the transverse direction (TD) [153].

There are numerous alternatives for the representation of texture information. The Euler angle parametrization is one of the most conventionally used for the analysis and presentation of texture information. The Euler angles refer to three rotations which, when performed in the correct sequence, transform the specimen coordinate

system onto the crystal coordinate system [149, 153]. There are several different conventions for expressing the Euler angles. The most commonly used are those formulated by Bunge [154], as shown in Figure 3-5. The rotations are:

- φ_1 about the normal direction ND, transforming the transverse direction TD into TD' and the rolling direction RD into RD'
- Φ about the axis RD' (in its new orientation)
- φ_2 about ND' (in its new orientation)

where (φ_1, Φ, φ_2) are the three Euler angles (Bunge notation). The effect of the operation sequence of these three rotations can be followed on Figure 3-5. Applying these rotations into the determined sense and order brings one of the coordinate systems into coincidence with the other [139, 149].

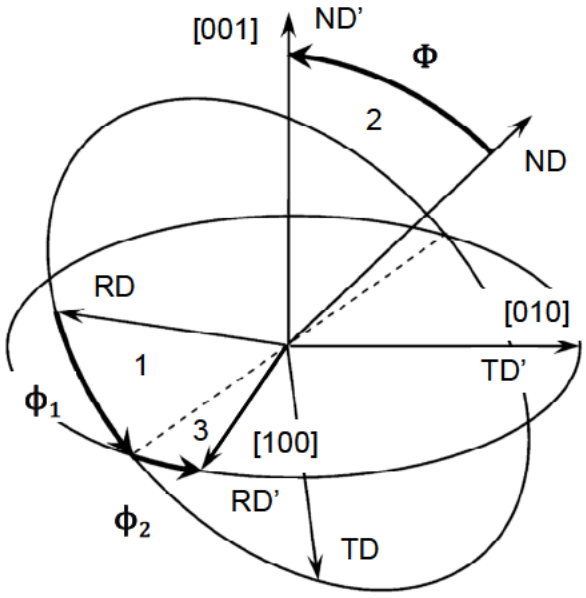

Figure 3-5. Definition of the orientation of a coordinate system, following the conventional interpretation of the Euler angles. In order 1, 2, 3 as shown, describes the rotation between the specimen (RD, TD, ND) and crystal axes (100, 010, 001), respectively [149, 153].

Any orientation expressed in terms of its Euler angles can be represented unequivocally as a point in a three-dimensional coordinate system whose axes are given by the three Euler angles. The resulting space is referred to as the Euler space [153]. Plotting the Euler angles on orthogonal axes forms a group space that is 2π-periodic along all three axes. Since, in this space, a cube of edge length 2π contains two points for every orientation, the Euler angles are generally restricted to the values $0 \leq \phi_1 < 2\pi$, $0 \leq \Phi < \pi$, $0 \leq \phi_2 < 2\pi$ in order to remove the redundant points. Cubic crystal symmetry and orthorhombic sample symmetry reduce the fundamental

zone still further. For this reason, the region defined by $0 \leq \phi_1 < \pi/2$, $0 \leq \Phi < \pi/2$, $0 \leq \phi_2 < \pi/2$ is often selected instead for these symmetries [149]. The benefit of this choice is that the planar surfaces permit a natural presentation in two dimensions by a series of parallel sections, conventionally selected perpendicular to the ϕ_2 axes. This information can be used to construct an orientation distribution function (ODF), indicating the probability of finding a volume element within the material with a particular crystalline orientation [149, 151].

3.2.5. Atomic force microscopy (AFM)

The atomic force microscopy (AFM), is part of a larger family of instruments termed the scanning probe microscopes (SPMs). These also include the scanning tunneling microscope (STM) and scanning near field optical microscope (SNOM), amongst others. The common factor in all SPM techniques is the use of a very sharp probe, which is scanned across a surface of interest, with the interactions between the probe and the surface being used to produce a very high resolution image of the sample, depending upon the technique and sharpness of the probe tip. In the case of AFM, the probe is a stylus that interacts directly with the surface, probing the repulsive and attractive forces which exist between the probe and the sample surface to produce a high resolution three-dimensional topographic image of the surface [155].

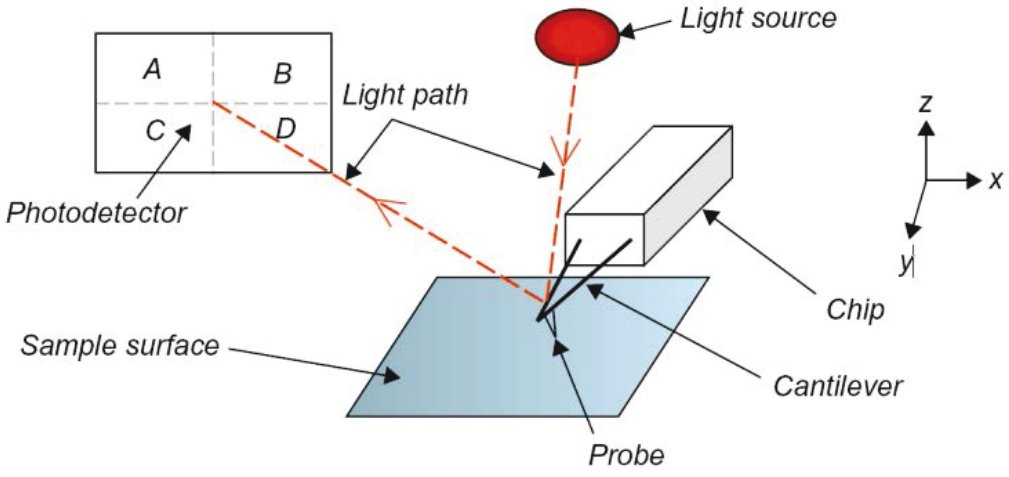

Figure 3-6. Basic AFM set-up [155].

The core of an AFM instrument is a sharp probe mounted near the end of a flexible cantilever arm. Figure 3-6 shows the basic set-up of a typical AFM. The probe is brought into and out of contact with the sample surface by the use of a piezocrystal upon which either the cantilever chip or the surface itself is mounted, depending upon the particular system being used. Movement in this direction is conventionally

referred to as the *z*-axis. A beam of laser light is reflected from the reverse side of the cantilever onto a position-sensitive photodetector. Any deflection of the cantilever will produce a change in the position of the laser spot on the photodetector, allowing changes to the deflection to be monitored. The most common configuration for the photodetector is a quadrant photodiode divided into four parts with a horizontal and a vertical dividing line. By raster-scanning the probe across a surface of interest and simultaneously monitoring the deflection of this arm, as it meets the topographic features present on the surface, a three-dimensional picture can be built up of the surface of the sample to a high resolution. The forces of interaction between the probe and the sample may also be measured as a function of distance by the monitoring of the deflection of the cantilever, provided that the spring constant of the lever arm is sufficiently calibrated [155].

Many different variations of this basic technique are currently used to image surfaces using the AFM, depending upon the properties of the sample and the information to be extracted from it. Usually, when a hard and relatively flat surface has to be imaged, 'static' techniques, such as the contact mode are used, mainly due to its simplicity of operation. The probe remains in constant contact with the sample at all times and thus the probe–sample interaction occurs in the repulsive regime [155]. Particularly, in the present work AFM topography scans were performed in contact mode on selected residual imprints using a Park XE150 instrument (Park Systems Corp., Suwon, South Korea).

3.3. Mechanical behavior

3.3.1. Uniaxial tensile testing

The engineering tensile test is widely used to provide basic design information on the strength of materials. In such test, a specimen is subjected to an increasing uniaxial tensile force while simultaneous observations are made of the elongation of the specimen until failure. The tensile force is recorded as a function of the change in gage length. An engineering stress-strain curve can be subsequently constructed from the load-elongation measurement [101, 156], where engineering stress is defined as:

$$\sigma = {}^{F}/_{A_0} \qquad \textbf{(Eq. 3-5)}$$

where F is the tensile force and A_0 the initial cross-sectional area of the gage section. Engineering strain can be defined as:

$$\varepsilon = {\Delta L}/{L_0} \qquad \textbf{(Eq. 3-6)}$$

where L_0 is the initial gage length and ΔL is the change in gage length (L - L_0). The advantage of dealing with stress versus strain rather than load versus elongation is that the stress-strain curve is independent of the specimen dimensions [101, 156]. For most metals, the initial elastic portion of the curve is linear. The slope of this linear region is called the elastic modulus or Young's modulus [101, 156]:

$$E = {\sigma}/{\varepsilon} \qquad \textbf{(Eq. 3-7)}$$

When the stress rises high enough values, the strain hardening behavior ceases to be linear and the strain behavior does not fully disappear after unloading. The remaining strain is called plastic strain. Once plastic deformation has begun, there will be both elastic and plastic contributions to the total strain.

The onset of the plastic plasticity is usually described by an offset yield strength, $\sigma_{0.2}$, which can measured with great reproducibility. It can be measured by constructing a straight line parallel to the initial linear portion of the stress-strain curve, i.e. at 0.2 % offset. The offset yield strength, $\sigma_{0.2}$, is the stress at which this line intersects the stress-strain curve. The tensile strength (or ultimate strength) , σ_{UTS}, can be defined as the maximum value of the engineering stress-strain curve, i.e. the maximum load which is achieved divided by the original cross-sectional area of the specimen. Up to the maximum load, the deformation is uniform all along the gage section. In the case of ductile materials, such as steel alloys, the tensile strength corresponds to the point at which the deformation starts to localize, forming a neck [101, 156].

Two common parameters are used in order to describe the ductility of a material. First, the uniform elongation, ε_u, is the percentage of elongation at the point (stress) at which necking begins. Second, the elongation or engineering strain to fracture, ε_f, is the final strain value reached during test before failure [101, 156].

Another key property that can be determined from the engineering stress-strain curve is the strain hardening exponent (n). The n-value is given by the slope of the graph which plots the logarithm of the true stress versus the logarithm of the true strain in the region of uniform elongation [101, 156].

Miniature tensile specimens having a gauge length of 4 mm, a gauge width of 1 mm and a thickness of 1 mm were machined from the Q&P processed strips. Tensile specimens were loaded at room temperature using a Kammrath&Weiss (Kammrath & Weiss GmbH, Dortmund, Germany) tensile/compression module. Tensile specimens were deformed to failure with the constant cross-head speed corresponding to the initial strain rate of 10^{-3} s^{-1}.

3.3.2. Nanoindentation tests

Indentation testing is a simple method that consists essentially of marking the material whose mechanical properties are unknown with another material whose properties are known. In particular, nanoindentation is an indentation test in which the length scale of the penetration is measured in nanometers (10^{-9} m) rather than microns (10^{-6}m) or millimeters (10^{-3}m), the latter being common in conventional hardness tests [157]. Apart from the displacement scale involved, the distinguishing feature of most nanoindentation testing is the indirect measurement of the contact area, i.e. the area of contact between the indenter and the specimen. In nanoindentation tests, the size of the residual impression is of the order of microns and too small to be conveniently measured directly. Thus, the depth of penetration beneath the specimen surface is measured as the load is applied to the indenter. This, together with the known geometry of the indenter, allows the size of the contact area to be determined at full load [157].

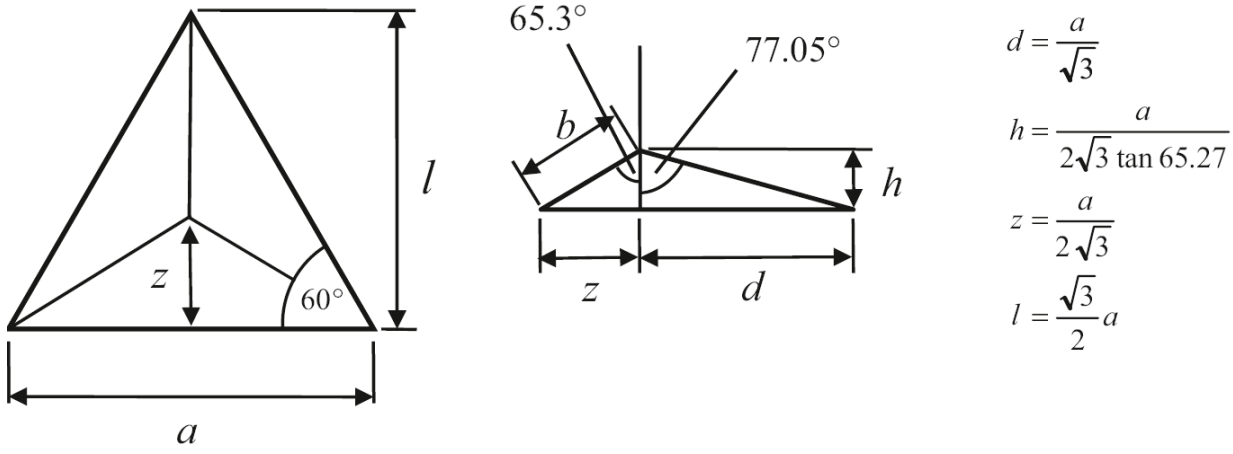

Figure 3-7. Schematic representation of the Berkovich indenter [157].

The Berkovich indenter [158] in Figure 3-7, is frequently used in small-scale indentation studies. It has the advantage that the edges of the pyramid are more easily constructed to meet at a single point, rather than the inevitable line that occurs

in the four-sided Vickers pyramid. The face angle of the Berkovich indenter normally used for nanoindentation testing is 65.27°, which gives the same projected area-to-depth ratio as the Vickers indenter. The typical tip radius for a new Berkovich indenter is in the range between 50 to 100 nm. This can increase to ≈450 nm with use [157].

The two mechanical properties measured most frequently using load and depth sensing indentation techniques are the Young modulus values, E, and the nanohardness, H. Both the nanohardness and the Young modulus are determined from the analysis of the load-displacement curves using the method developed by Oliver and Pharr [159]. The effect of non-rigid indenters on the load-displacement behavior can be accounted for by defining a reduced modulus, E_r, through [159]:

$$\frac{1}{E_r} = \frac{(1-\nu^2)}{E} + \frac{(1-\nu_i{}^2)}{E_i} \qquad \textbf{(Eq. 3-8)}$$

Where E and ν are the Young Modulus and Poisson's ratio for the specimen and E_i and ν_i are the same parameters for the indenter. In this work, $E_i = 1050\ GPa$ and $\nu_i = 0.07$, corresponding to a diamond tip.

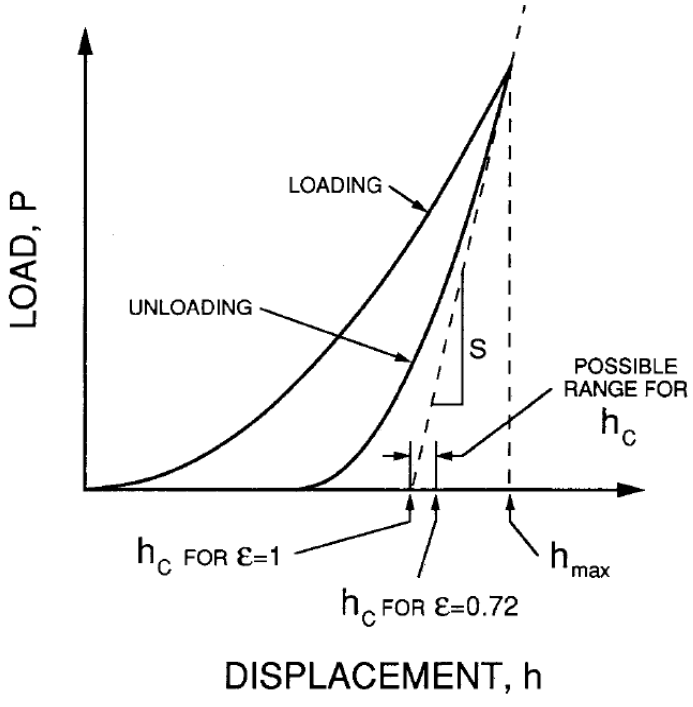

Figure 3-8. A schematic representation of load versus indenter displacement for an indentation experiment [159].

The experimentally measured stiffness, S_t, of the unloading part of the indentation load - displacement curve (Figure 3-8), can be obtained through:

$$S_t = \frac{dP}{dh} \quad \textbf{(Eq. 3-9)}$$

The reduced modulus of the sample can be derived by measuring the initial unloading stiffness, through [159]:

$$E_r = \frac{\sqrt{\pi}}{2} \cdot \frac{S_t}{\sqrt{A(h_c)}} \quad \textbf{(Eq. 3-10)}$$

where A is the contact area at peak load. This area of contact is determined by the geometry of the indenter at the depth of contact, h_c, which is the vertical distance along which contact is made. From the load - displacement data it is also easy to determine the depth at peak load, h_{max}, and the final depth of the residual hardness impression, h_f [159]. In order to calculate the contact depth from the experimental data, it should be noted that:

$$h_c = h_{max} - \epsilon \cdot \frac{P_{max}}{S_t} \quad \textbf{(Eq. 3-11)}$$

where $\epsilon = 0.72$ for a Berkovich indenter. With the determined contact area, the modulus can be computed from (Eq. 3-10) and the hardness from its definition:

$$H = \frac{P_{max}}{A(h_c)} \quad \textbf{(Eq. 3-12)}$$

where P_{max} is the peak indentation load and $A(h_c)$ is the projected area of contact at peak load of the hardness imprint. $A(h_c)$ is usually calibrated by indenting reference materials, mostly used silica.

During the nanoindentation test, certain phenomena controlled by plasticity around the indenter, such as pile up or sink in, might take place. The presence of these events has a negative effect on the determination of the projected area of contact, since they are not taken into account in the method developed by Oliver and Pharr [159]. Consequently, this causes inaccuracies in the Young modulus and hardness values provided by nanoindentation tests. For this reason, AFM topography scans were performed in contact mode on selected residual imprints in order to estimate the projected area of contact. Then, the nanohardness and the Young modulus

values were recalculated from the peak indentation load and the measured projected area of contact.

The existence of the indentation size effect (ISE), where the material appears to be harder at small indentation depths [160] was reported in the present work for the studied materials. However, due to the expected small size of the microconstituents, a maximum depth of 100 nm was chosen in order to keep the plastic zone within the individual microconstituent.

In the present work, nanoindentation tests were performed after EBSD sample preparation and characterization. This way, surfaces had a low roughness (≤5 nm), suitable for performing nanoindentation measurements at the prescribed maximum depth of 100 nm. Nanoindentation tests were performed on a Hysitron TI950 Triboindenter (Hysitron, Minneapolis, USA) using a Berkovich tip on square areas having a size of ≈12x12 μm^2, which were *a priori* analyzed by EBSD. Five areas were subjected to testing for each material's condition. In order to target specific phases within well-defined grains, these square areas were scanned, prior to nanoindentation, using the SPM mode of the instrument. Nanoindentation tests were carried out in displacement control mode, at a constant strain rate ($\dot{\varepsilon} = \dot{h}/h$) of 0.07 s^{-1}, where h is the penetration depth and $\dot{h}$ the penetration rate of indenter. At least 20 indents were performed on each phase, at an imposed maximum depth of 100 nm. At least 8 indentation tests were found to be located strictly within each individual microconstituent with good quality load-displacement depth curves.

3.3.3. *In situ* tensile testing and digital image correlation analysis

More precise quantitative information about the deformation at the micrometer scale can be obtained through the application of full-field measurement methods, e.g., digital image correlation (DIC) technique in combination with in situ tensile testing inside a SEM [161].

Miniature tensile specimens having a gauge length of 4 mm, a gauge width of 1 mm and a thickness of 1 mm were machined from the Q&P processed strips. *In situ* tensile tests were carried out in the SEM EVO MA15 (Carl Zeiss, Oberkochen, Germany) operating at an accelerating voltage of 20 kV. Tensile specimens were loaded at room temperature using a Kammrath&Weiss tensile/compression module (Kammrath&Weiss GmbH, Dortmund, Germany) embedded in the SEM chamber. Tensile specimens were deformed to failure with the constant cross-head speed

corresponding to the initial strain rate of 10^{-3} s^{-1}. Tensile deformation was stopped periodically, the tensile specimens were unloaded and secondary electron micrographs with 1024x768 pixel resolution were taken from the central area of the miniature tensile specimens after each deformation step. The cross-head displacement steps were 100 μm corresponding to a global strain of 2.5 %. The analyzed areas had dimensions of 20 x 25 μm^2.

The DIC technique was used to determine local in-plane plastic strain distribution after tensile deformation of the Q&P steels. For that purpose, SEM images of the specimens before deformation and after each deformation step were uploaded into the Vic-2D 2009 Digital Image Correlation software (VicSNAP, Correlated Solutions Inc., Columbia, SC, USA) for full-field strain analysis and generation of deformation maps.

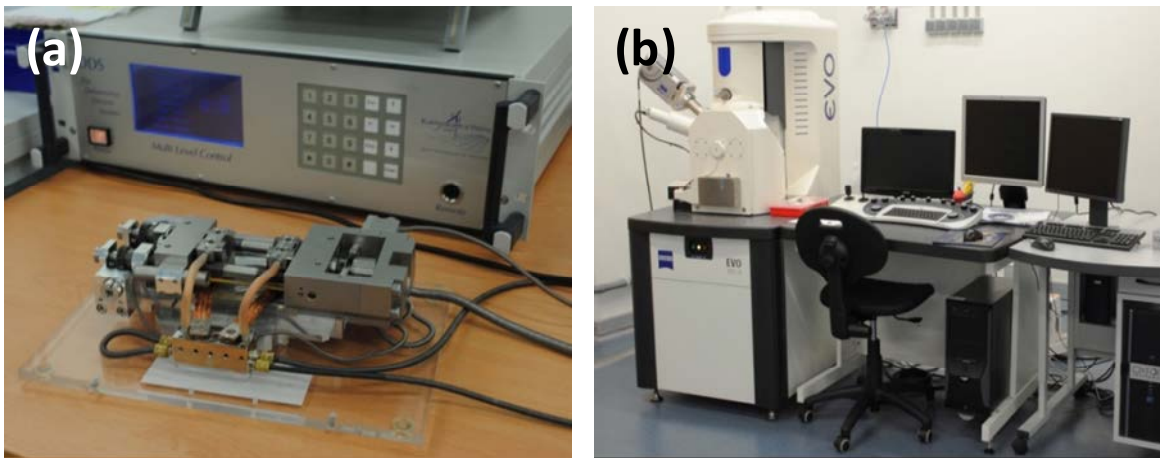

Figure 3-9. Kammrath&Weiss tensile/compression module (a) and SEM EVO MA15 (b).

DIC is a non-contacting optical technique to measure the displacement field on the surface of a specimen at different stages of deformation, widely used in the field of experimental mechanics. Accordingly, DIC has been applied in recent years for revealing the deformation and fracture mechanisms in Q&P inter-critically annealed steels [20], Q&P fully austenitized steels [162], DP steels [69-71, 163] and MMCs [76], by analyzing secondary electron images obtained during in situ testing. Displacement correlation in DIC is based on the presence of a random speckle pattern on the specimen surface whose movement is tracked and compared with the initial, reference pattern (see Figure 3-10). In the case of secondary electron images, this pattern is produced naturally by the microstructural features [161].

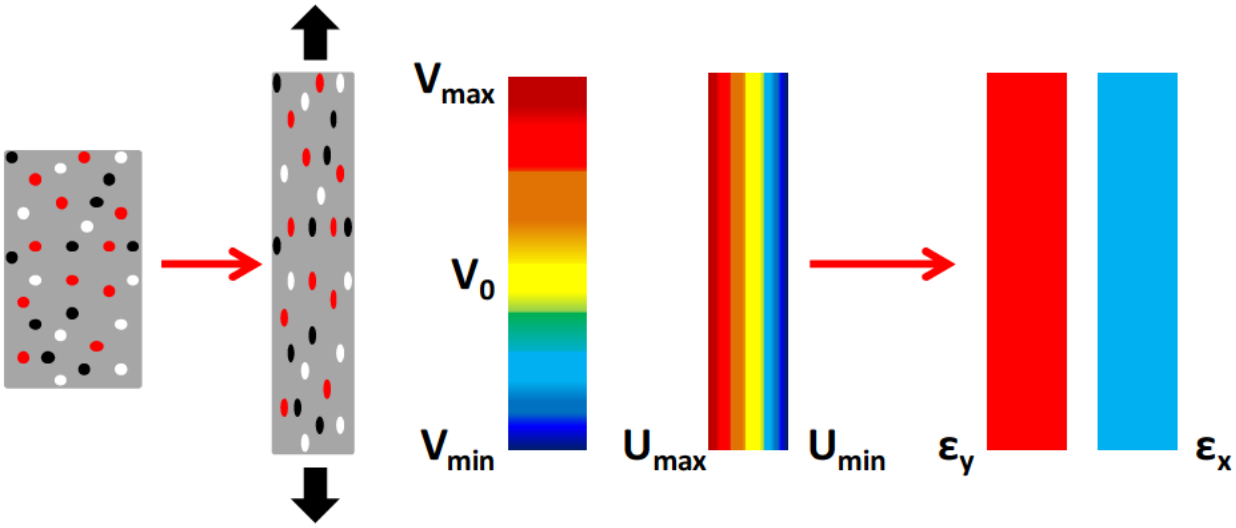

Figure 3-10. Schematic representation of the working principle of the DIC technique.

The full strain field on the surface can be obtained afterwards as the derivative of the displacement field. Briefly, the basic principles of the technique can be explained as follows: the displacement field is computed by tracking the distribution of grey intensity on the specimen surface in images acquired at different stages upon loading. The position of an arbitrary pixel i of the image in the undeformed specimen can be expressed in terms of its coordinates X_i in the reference configuration. This pixel will be displaced to a new position given by the coordinates x_i in the deformed configuration. Both coordinates are related by:

$$x_i = X_i + U_i \qquad \text{(Eq. 3-13)}$$

where U_i is the displacement vector. Let G(X) and g(x) be the intensity of the grey level in each pixel of the images corresponding to the undeformed and deformed configurations, respectively. If it is assumed that the intensity pattern deforms but it does not change its local value during deformation (i.e., g(x) = G(X + U)), it is possible to track the displacement of every point of the specimen surface by identifying the displacement field which minimizes a residual function C_r over the whole region of interest, where C is expressed as:

$$C_r(X,x) = 1 - \frac{\sum G(X)g(x)}{\sqrt{\sum G(X)^2 \sum g(x)^2}} \qquad \text{(Eq. 3-14)}$$

This minimization problem is, however, too complex to be solved in a general case and it has been simplified by introducing two main approximations. First, the displacement of an arbitrary point is obtained from the evaluation of the gray

intensity in its neighborhood. This set of pixels around the central one is called the subset. Second, the deformations are constant within this subset. Under these assumptions, the coordinates X_i and x_i of a point of the subset in the reference and deformed configurations can be related with the coordinates of the central point of the subset (X_c and x_c) by:

$$x_i = X_C + U_C + \nabla(U)(X_i - X_C) \quad \textbf{(Eq. 3-15)}$$

where $\nabla(U)$ stands for the constant displacement gradient within the subset. Therefore, the subset is limited to capture homogeneous deformations. Both U_c and $\nabla(U)$ are obtained from the iterative minimization of the correlation function C (Eq. 3-14) within the subset.

Once the displacement of the central pixel has been obtained, the subset is shifted along X- and Y-directions to calculate the next point. The shift of the subset is determined by the step size, which defines how many pixels the subset was moved. Finally, the strains are computed according to the Lagrangian approach by taking the numerical derivative of the displacement field with a spacing defined by the strain window. A detailed overview of displacement and deformation measurements through digital image correlation, and its application to practical cases can be found in [164]. Deformation maps of the plastic strains in the loading direction ε_{yy} are presented in the Section 4.2: a subset of 60 pixels and a step size of 3 pixels have been used.

3.3.4. Fracture characterization

In order to characterize the fracture behavior of materials, linear elastic fracture mechanics (LEFM) is only valid as long as nonlinear deformation is confined to a small region that surrounds the crack tip. However, in many materials it is virtually impossible to characterize the fracture behavior with LEFM and, consequently, the fracture toughness, K_{1C} cannot be determined. In such cases, an alternative fracture mechanics model is thus required. In this context, elastic-plastic fracture mechanics (EPFM) can be applied to all materials that exhibit time-independent, non-linear behavior (i.e., plastic deformation) [102]. Two elastic-plastic parameters must then be introduced: the crack-tip-opening displacement (CTOD) and the J contour integral. Both parameters define the crack-tip conditions in elastic-plastic materials, and can therefore be used as a fracture design critera. Critical values of CTOD or J give

nearly size-independent measurements of fracture toughness, even for relatively large amounts of crack-tip plasticity [102].

When Wells [165] attempted to measure the K_{1C} values in a number of structural steels, he found that these materials were too tough to be characterized by LEFM. While examining fractured test specimens, Wells noticed that the crack tip had moved apart prior to fracture; plastic deformation had blunted an initially sharp crack. The degree of crack blunting increased proportionally to the toughness of the material. This observation led Wells to propose the opening at the crack tip as a measure of fracture toughness (see Figure 3-11). Today, this parameter is known as the CTOD or δ [102].

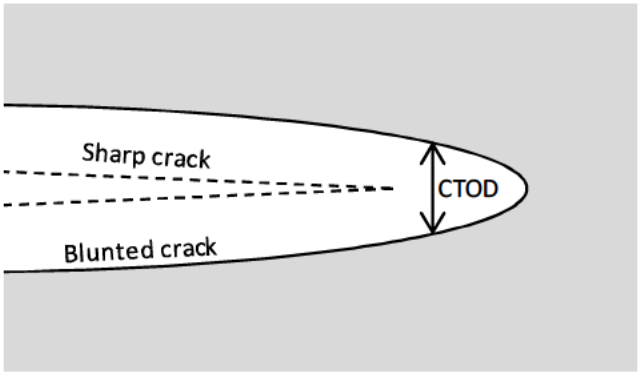

Figure 3-11. Crack-tip-opening displacement (CTOD). An initially sharp crack blunts with plastic deformation, resulting in a finite displacement (CTOD) at the crack tip [102].

On the other hand, the J contour integral has enjoyed great success as a fracture characterizing parameter for nonlinear materials. By idealizing elastic-plastic deformation as nonlinear elastic, Rice [166] provided the basis for extending fracture mechanics methodology well below the validity limits of LEFM. Rice applied deformation plasticity (i.e. nonlinear elasticity) to the analysis of a crack in a nonlinear material. He showed that the nonlinear energy release rate J could be written a path-independent line integral. Hutchinson [167] and Rice and Rosengren [168] also showed that J uniquely characterizes crack-tip stresses and strains in nonlinear materials. Thus, the J integral can be viewed as both an energy parameter and a stress intensity parameter [102].

For linear elastic conditions, the relationship between CTOD and J are given by [169]:

$$J = m \cdot \sigma_Y \cdot CTOD \qquad \textbf{(Eq. 3-16)}$$

where m is a dimensionless constant that depends on the stress state and material properties.

The main obstacle for the analysis of the fracture behavior of Q&P steels is that they are produced as thin strips, due to strict requirements on the applied heat treatment. In the case of thin sheets, the double edge-notched tensile (DENT) specimen is particularly suitable as the transverse stress between the notches is tensile and there are no buckling problems [170]. Unfortunately, the DENT geometry is not specified in the standards, but the validity of the test has already been carefully assessed by finite element simulations [109, 170] as well as validated by experimental tests [105, 110, 171]. Therefore, DENT specimens (Figure 3-12) were used for the evaluation of the fracture toughness, consisting of rectangular plates with a length (L) of 100 mm (parallel to the rolling direction), a width (W) of 50 mm and a thickness (t) of 1 mm [109, 110, 170, 171]. All the conventional requirements in fracture mechanics standards were respected. The notches were first machined by electrical discharge machining (EDM) followed by wire cut and additional sharpening with razor blade. This way, the root radius of pre-crack was conveniently minimized, and it is estimated to be around several microns.

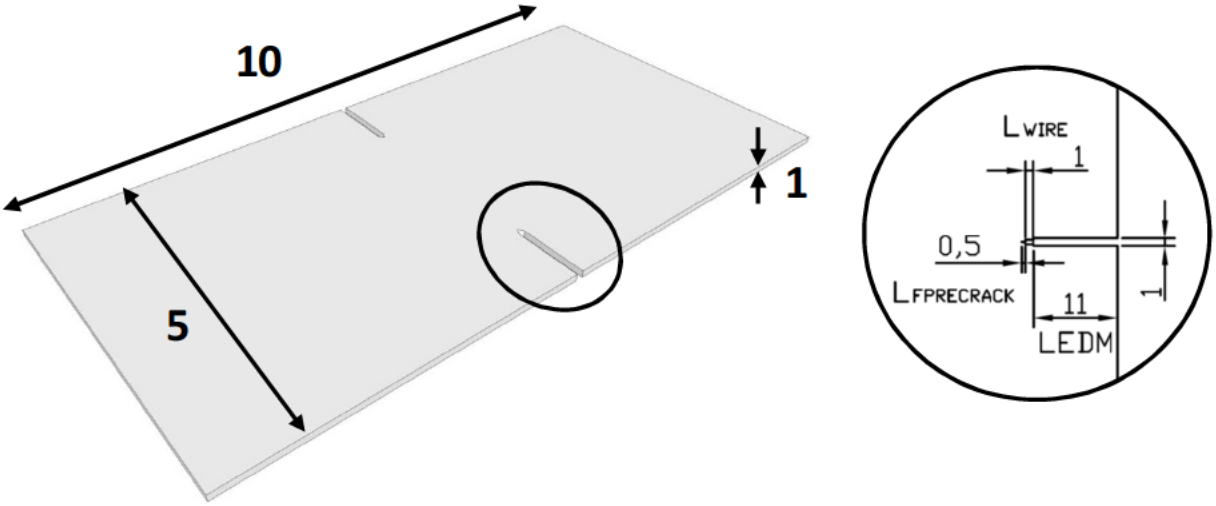

Figure 3-12. Schematic illustration of the DENT specimen.

Fatigue pre-cracking was subsequently performed under the following conditions:

$$K_{min}/K_{max} = 0.1 \qquad \text{(Eq. 3-17)}$$

and,

$$\text{ratio}\left({}^{a}/_{W}\right) \approx 0.5 \qquad \textbf{(Eq. 3-18)}$$

Where *a* is the total crack length. The fatigue pre-cracks were symmetrical and longer than 300 μm on each side. The samples were subjected to tensile testing after fatigue pre-cracking. Tensile tests up to failure were carried out at room temperature with constant cross head speed of $\dot{\varepsilon} = 1\ {}^{mm}/_{min}$ using a INSTRON 3384 (Norwood, MA, USA) testing system. DIC technique equipped with a Vic-2D 2009 software (VicSNAP, Correlated Solutions Inc., Columbia, SC, USA) was employed for precise estimation of deformation strain during testing. The DC potential drop technique [172] was used to measure crack propagation during fracture testing. It relies upon the passage of a constant current ($I_o = 0.24\ A$) through the body of the specimen. The voltage generated across the specimen due to the constantly changing resistance as the crack propagates, is measured by a pair of potential probes mounted on the front edge of the specimen. The measured DC potential drop at any crack length is then converted into the corresponding crack length by the Johnson formula [172]:

$$a = \frac{2 \cdot W}{\pi} \cdot \arccos\left[\frac{\cos\frac{\pi}{2 \cdot W}}{\frac{V}{V_o} \cdot arccos\frac{\cosh\frac{\pi \cdot y}{2 \cdot W}}{\cos\frac{\pi \cdot a_o}{2 \cdot W}}}\right] \qquad \textbf{(Eq. 3-19)}$$

where *V* and *Vo* (*Vo* = 0.1 mV) are the updated and initial measured potential values and *y* is one half of the potential probe span. At least four specimens were tested for each material and the results were found to be reproducible.

Fracture surfaces on both halves of the DENT specimens were subsequently analyzed. In order to reconstruct the depth information from SEM images, stereographic methods were used [173]. For this purpose, an automatic fracture surface analysis system was utilized [74, 174, 175]. Stereoscopic electron microscopy provides several advantages compared with other methods for the 3D-reconstruction of microscopic objects. Since the "sensor" has no mechanical contact with the observed specimen, SEM is well suited for very rough objects such as fracture surfaces. Furthermore the depth of focus as well as the lateral resolution is significantly better than with optical methods [173].

The key part of this system is an algorithm which is able to automatically find homologue points (points in the two images that belong to the same physical point on the specimen), in the stereo pair taken in the SEM. This means, that points which are projections of the same object on the specimen in the two images, have to be identified (see Figure 3-13). In the field of image processing, extensive research has been done to cope with this problem and the solution procedure is generally called matching. Due to the rich contrast and the good signal to noise ratio SEM images are an appropriate basis for an automatic matching procedure [173, 176]. Prerequisite for the reconstruction of the topography is the knowledge of the parameters tilt angle, working distance and magnification. Typical tilt angles are 5° to 10°.

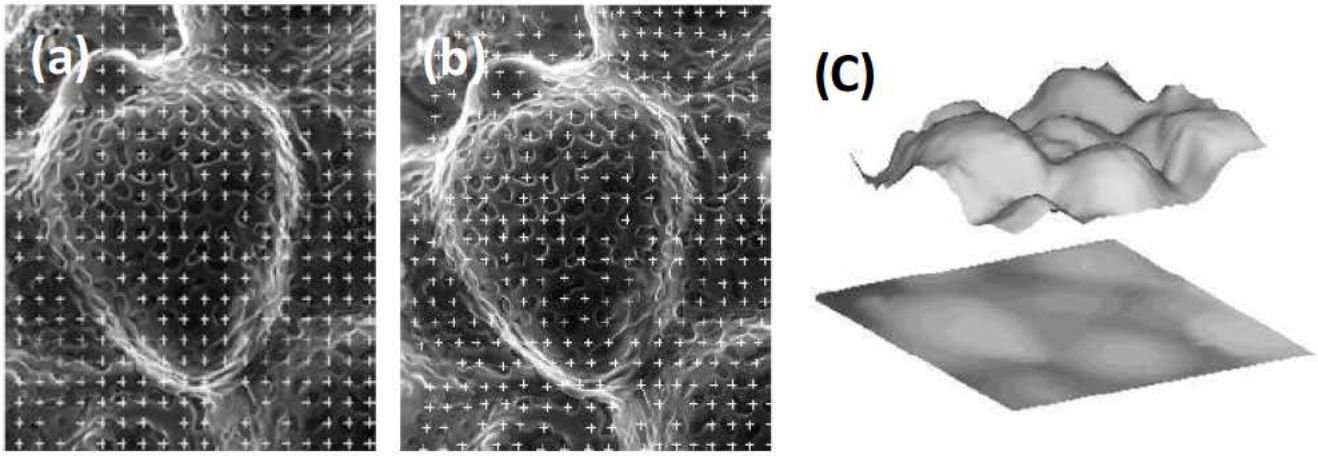

Figure 3-13. Monoscopic SEM image example image taken at (a) 0° and (b) 5°; (c) Shaded surface plot of the 3D-reconstructed object [176].

In this work, examination of the fracture surfaces of the QP-0.25-5 and QP-0.28-2 samples was performed using a SEM EVO MA15 (Carl Zeiss, Oberkochen, Germany) operating at accelerating voltage of 20 kV. The stereo image pair is produced by tilting the specimen in the SEM: images taken at 0° and 5° tilting angles were used as the input to the automatic fracture surface analysis system. The SEM images consist of 1024 x 768 pixels at 256 gray levels. From the homologue points and the three image parameters (pixel size, working distance and tilt angle) a three-dimensional digital elevation model (DEM) of the depicted fracture surface is generated with the MeX software (Alicona, Graz, Austria). The DEM can be arbitrarily cut to extract fracture surface profiles. The system has been widely used for the experimental study of fracture surfaces of pure metals [177], steels [176, 178, 179] and MMCs [180, 181].

3.3.5. Fatigue characterization

Specimens for fatigue testing were machined from Q&P processed strips and their geometry is displayed in Figure 3-14. Then, the surface of the specimens was prepared using standard metallographic techniques and final polishing, in order to remove the superficial defects that could have been induced during the machining process and to improve the quality of the surface.

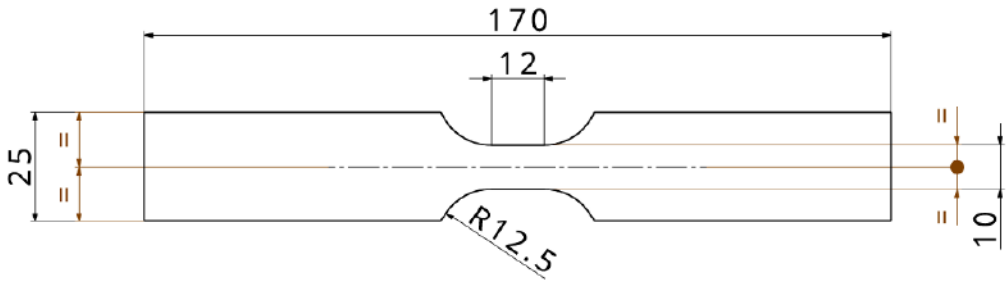

Figure 3-14. Geometry of the specimens for fatigue testing.

After sample preparation, cyclic loading tests were performed using a RUMUL TESTRONIC (RUMUL, Neuhausen am Rheinfall, Switzerland) fatigue resonant testing machine (Figure 3-15). The considerations listed below were followed:

- Imposed axial stress;
- Stress ratio 0.1;
- Load frequency between 75 and 100 Hz;
- Failure criteria: specimen fracture.

The basic method for presenting engineering fatigue data at high number of cycles is by means of the *S-N* curve, a plot of stress amplitude (S) against the number of cycles to failure (N). The usual procedure for determining an *S-N* curve is to test the first specimen at high stress where failure is expected in a fairly short number of cycles, i.e. at about two-thirds the static tensile strength of the material. Cycles to failure are counted and the test is repeated at decreasing amplitudes. The test stress is then decreased for each succeeding specimen until one or two specimens do not fail in the specified number of cycles, which is usually $\approx 10^7$ cycles. The highest stress at which a run-out (non-failure) is obtained is taken as the fatigue limit [101].

As the number of cycles increase, the response of the part evolves, thus:

- At high stresses, the material withstands a limited number of cycles before fracture. Under these conditions, the fatigue regime is commonly defined as Low-Cycle Fatigue (LCF).

- At lower stresses, the fatigue life increases and the fatigue failure is reported after an increased number of cycles. In this case, the fatigue regime is commonly defined as High-Cycle Fatigue (HCF).

Usually, a logarithmic or semi-logarithmic scale is used for N [101]. It will be noted that this *S-N* curve is mainly concerned with fatigue failure at high number of cycles ($N > 10^4 - 10^5$ cycles). Under this conditions, the stress on a gross scale is elastic, but the metal deforms plastically in a highly localized way. With increasing stresses, the fatigue life is progressively decreased [101].

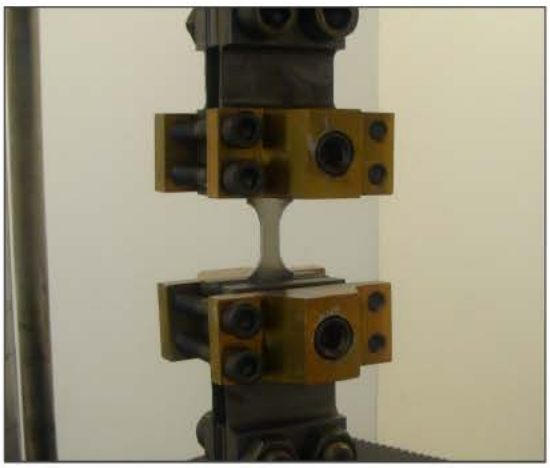

Figure 3-15. Specimen mounted on testing device.

In the present work, the *S-N* curves were plotted according to the ISO 1099:2006(E) standard [182]. At least 10 samples were tested per each Q&P steel. The fatigue strength was estimated from the *S-N* curves.

3.3.5.1. Analysis of fatigue fracture surfaces

Fatigue fracture surfaces of the broken specimens were subsequently studied. Specimens were carefully analyzed using a SEM EVO MA15 (Carl Zeiss, Oberkochen, Germany) operating at accelerating voltage of 20 kV, in order to identify mechanisms of fatigue crack initiation and propagation.

Reconstruction of fracture surfaces (as described in Section 3.3.4) was performed if it was necessary. Two images at 0° and 10° tilting, a working distance of 10 mm and constant magnification were used as the input for the automatic fracture surface analysis system.

3.3.5.2. Microstructural evolution of RA during fatigue testing

In order to study the effect of cyclic deformation on microstructure and the role of RA in cyclic behavior, the microstructure of samples from both steel grades after fatigue testing with the highest stress amplitude (i.e. the lowest number of cycles before failure) and with the lowest stress amplitude (i.e. with the highest number of cycles before failure) was carefully analyzed. A FEI Quanta™ Helios NanoLab 600i (FEI Corporate, Oregon, USA) equipped with a NordlysNano detector controlled by the AZtec Oxford Instruments Nanoanalysis (version 2.4®) software (Oxford Instruments, Abingdon, United Kingdom) was used for the microstructural characterization. The OIM scans were taken from areas located at 1 mm distance from the fracture surface of the broken specimens: thus, the measurements were performed inside the homogenously cyclically deformed zone, i.e., in the gauge length area, which was not affected by microscopic plastic deformation in front of the propagating crack.

4 Results and Discussion

4. RESULTS AND DISCUSSION

4.1. Effect of Q&P parameters on microstructure development and mechanical behavior of the Q&P steels

This section focuses on the influence of Q&P parameters on the microstructure with attention to phase composition, size, volume fraction and morphology of microconstituents as well as to texture and carbon content in RA. The steel with the QP-0.25 chemistry was subjected to Q&P processing with varying parameters (QT, PT and Pt) resulting in formation of multiphase microstructure, which was thoroughly studied in the present work using XRD and EBSD. Mechanical properties of the Q&P steel were measured by tensile testing and are discussed below.

4.1.1. Effect of Q&P parameters on microstructure and mechanical properties

Data on the Q&P parameters applied to the studied steel grade are presented in Table 4-1. Justification for the selection of these parameters is provided in Section 3.1.

Table 4-1. Q&P processing parameters applied to the studied steel grade.

Specimen		QT (°C)	PT (°C)	Pt (s)
QP-0.25-	1	224	350	500
	2	244	300	500
	3	244	350	500
	4	244	400	100
	5	244	400	500
	6	244	400	1000
	7	264	350	500

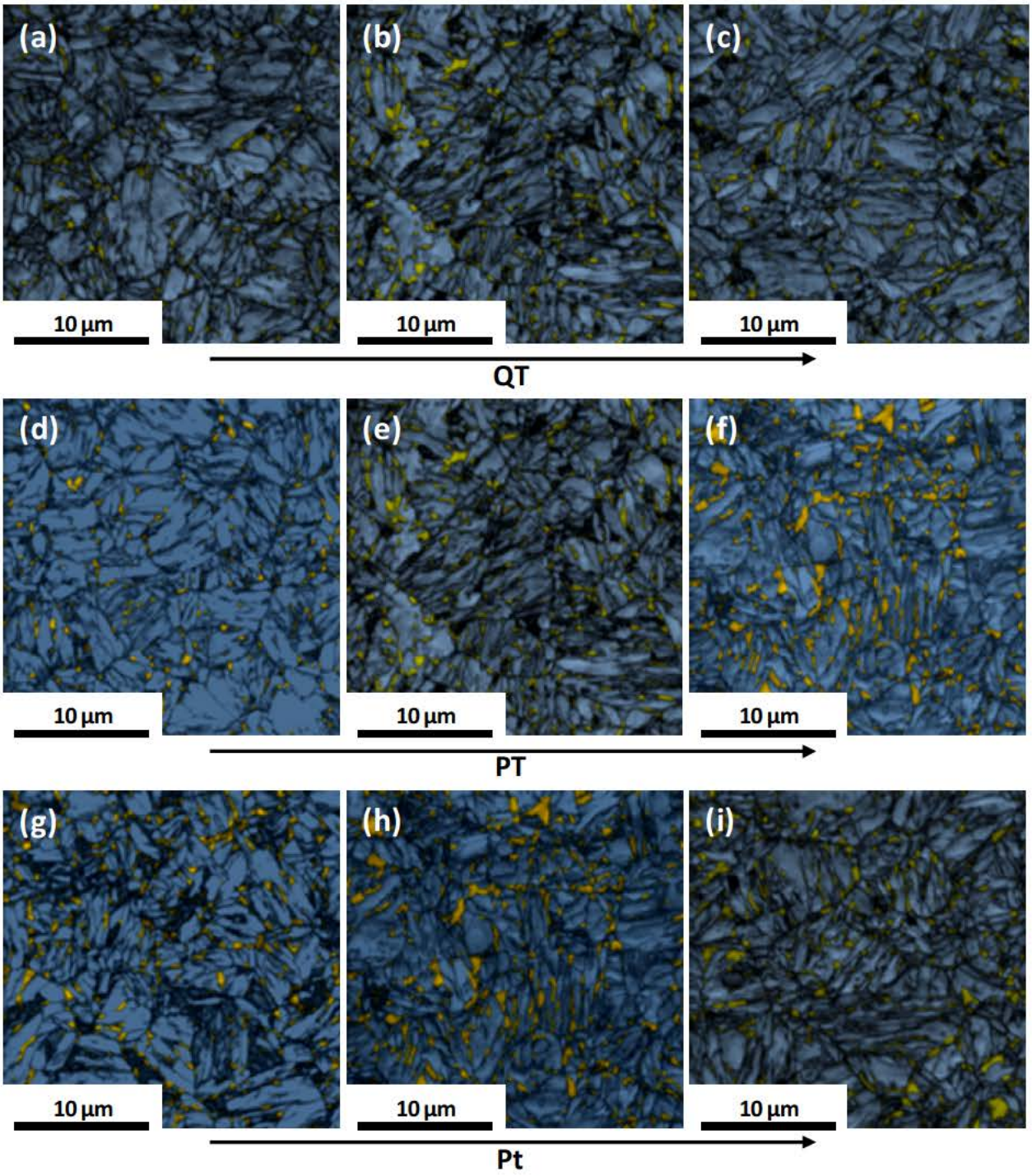

Figure 4-1. OIM maps of (a) the sample quenched at 224°C (QP-0.25-1), (b) the sample quenched at 244°C (QP-0.25-3) and (c) the sample quenched at 264°C for 500 s (QP-0.25-7); all of them were partitioned at 350°C for 500 s. (d) The sample partitioned at 300°C for 500 s (QP-0.25-2), (e) the sample partitioned at 350°C for 500 s (QP-0.25-3) and (f) the sample partitioned at 400°C for 500 s (QP-0.25-5); all of them were quenched at 244°C. (g) The sample partitioned at 400°C for 100 s (QP-0.25-4), (h) the sample partitioned at 400°C for 500 s (QP-0.25-5) and (i) the sample partitioned at 400°C for 1000 s (QP-0.25-6); all of them were quenched at 244°C.

OIM phase maps with BCC (martensite) in blue and FCC (RA) in yellow superimposed with the image quality maps of the studied samples are shown in Figure 4-1. After the applied Q&P treatment, irregular-shaped blocks of TM constitute the major phase of the microstructure, whereas the others (i.e. UM and RA) are dispersed in the matrix. The size of the microconstituents (TM and RA) is provided in Table 4-2. The average size of TM for all specimens is in the same range. Nevertheless, the Q&P parameters have a slight effect on the RA average grain size. Due to a less perfect BCC lattice, UM regions formed during the last quench to room temperature can be identified as the darkest ones and can be found in the vicinity of the yellow RA grains. The size of the UM can be roughly estimated but could not be accurately measured from the available OIM maps, since lattice distortion leads to a low pattern quality and indexation of the UM zones in the OIM scans.

Various RA morphologies are present in the microstructure (Figure 4-1): film-like RA, lamellar RA and blocky RA. A thorough analysis of the available OIM micrographs shows the growth of interlath RA from film-like to a blocky type as a function of partitioning parameters. Although the spatial resolution of the EBSD technique is reasonably high (step size is ≈ 40 nm), the smallest austenite laths formed between the martensite plates, as observed with TEM, have sizes in the range of 20–100 nm [21, 77]. The smallest laths can therefore not be resolved by EBSD but are detectable with XRD.

Table 4-2. Average grain size (equivalent circle diameter) for the different microconstituents of the Q&P steel.

Specimen		Tempered martensite (TM) (µm)		Retained austenite (RA) (µm)	
QP-0.25-	1	2.7	± 0.3	0.5	± 0.1
	2	2.3	± 0.1	0.4	± 0.1
	3	2.2	± 0.4	0.6	± 0.1
	4	2.2	± 0.2	0.5	± 0.2
	5	2.2	± 0.3	0.7	± 0.1
	6	2.4	± 0.1	0.7	± 0.2
	7	2.5	± 0.3	0.5	± 0.1

Table 4-3 lists the measurements of volume fraction and carbon content of RA, as well as the volume fraction of TM and UM which were determined by XRD combined with EBSD analysis.

Table 4-3. Volume fraction and carbon content (wt. %) of RA and volume fraction of UM and TM in the studied steel.

Specimen		Retained Austenite (RA)		Untempered Martensite (UM)	Tempered Martensite (TM)
		(%)	%C (wt.)		
QP-0.25-	1	14.2	0.91	13.8	72
	2	14.7	1.05	17.7	67.6
	3	14.4	0.99	14.1	71.5
	4	18.3	0.84	9.9	71.8
	5	17.9	1.03	12.2	69.9
	6	20.2	1.01	10.5	69.3
	7	13.5	1.11	15.8	70.7

Figure 4-2, Figure 4-3 and Figure 4-4 show typical engineering stress – engineering strain curves for the Q&P processed steel grades. From these curves, $\sigma_{0.2}$, σ_{UTS}, ε_u, and ε_f were determined and are summarized in Table 4-4. In order to estimate the strain hardening exponent n, true stress – true strain curves were fitted by a single power law (for $\sigma > \sigma_y$) [20, 21]:

$$\sigma = \alpha \cdot \sigma_y \cdot \left(\frac{\varepsilon}{\varepsilon_o}\right)^n \qquad \textbf{(Eq. 4-1)}$$

where σ_y is the yield stress, $\varepsilon_o = {}^{\sigma_y}/_{E}$, E the Young modulus and α a dimensionless parameter. The n-values are also given in Table 4-4 and show that the mechanical properties strongly depend on the applied Q&P parameters.

Table 4-4. Mechanical properties measured on miniature samples of the studied steel grade ($\sigma_{0.2}$, σ_{UTS}, ε_u, ε_f, n).

Specimen		$\sigma_{0.2}$ (MPa)	σ_{UTS} (MPa)	ε_U (%)	ε_f (%)	n
QP-0.25-	1	900	1357	10	22	0.19
	2	721	1419	10	21	0.25
	3	803	1471	11	21	0.26
	4	621	1462	17	26	0.24
	5	821	1267	16	28	0.19
	6	681	1275	16	29	0.20
	7	761	1354	13	24	0.24

Below, the effect of each Q&P parameter (QT, PT, Pt) on microstructure and mechanical properties is analyzed.

4.1.1.1. Influence of QT

The EBSD phase maps of the three samples quenched at different temperatures (QP-0.25-1, QP-0.25-3 and QP-0.25-7) are shown in Figure 4-1 a, b and c. By comparing these samples it can be observed that the QT affects neither the TM, nor the RA average size (Table 4-2). In addition, it can be seen that the average volume fraction of RA ranges from 13.5 % to 14.4 %, whereas its carbon content ranges from 0.91 to 1.11 wt. % and appears to increase with increasing QT (Table 4-3).

Various RA morphologies are present in the microstructure (Figure 4-1). In the QP-0.25-3 sample mostly blocky RA can be found, whereas in the QP-0.25-1 and QP-0.25-7 samples the prevalent type is the interlath lamellar one, but some blocky RA is also observed. As it was already reported in literature [21, 183], localized EBSD scans yield significantly lower RA fractions, being 5.9 %, 8.8 % and 5.0 % for the QP-0.25-1, QP-0.25-3 and QP-0.25-7 samples, respectively. Therefore, the fraction of smallest austenite laths (film-like type), which are not detected by EBSD, is higher in the samples quenched at 224°C and 264°C, respectively. The volume fraction of UM is 13.8 %, 14.1 % and 15.8 % for the samples quenched at 224°C, 244°C and 264°C respectively. Finally, the volume fraction of TM tends to slightly decrease with the QT: values of 72.0 %, 71.5 % and 70.7 % were obtained for the samples quenched at 224°C, 244°C and 264°C, respectively.

A hypothetical explanation for these observations can be offered: the fraction of martensite that undergoes carbon partitioning to the neighboring austenite during the partitioning step is determined to a large extent by the QT. The stabilized RA fraction is less dependent on higher QTs due to kinetic effects related to lower carbon diffusion in austenite creating pile-ups close to the grain boundaries resulting in local stabilization of austenite. Thus, a QT closely below the M_s temperature results in a small fraction of martensite, so the carbon available for partitioning might not be sufficient for the stabilization of the austenite. This indeed leads to a high fraction of relatively unstable austenite that transforms to martensite in the final quench. On the other hand, lower QT results in the formation of a higher fraction of martensite in the first quench. Therefore, a higher fraction of austenite is consumed during the initial quench, that will not be available for carbon enrichment during the partitioning step [16, 30].

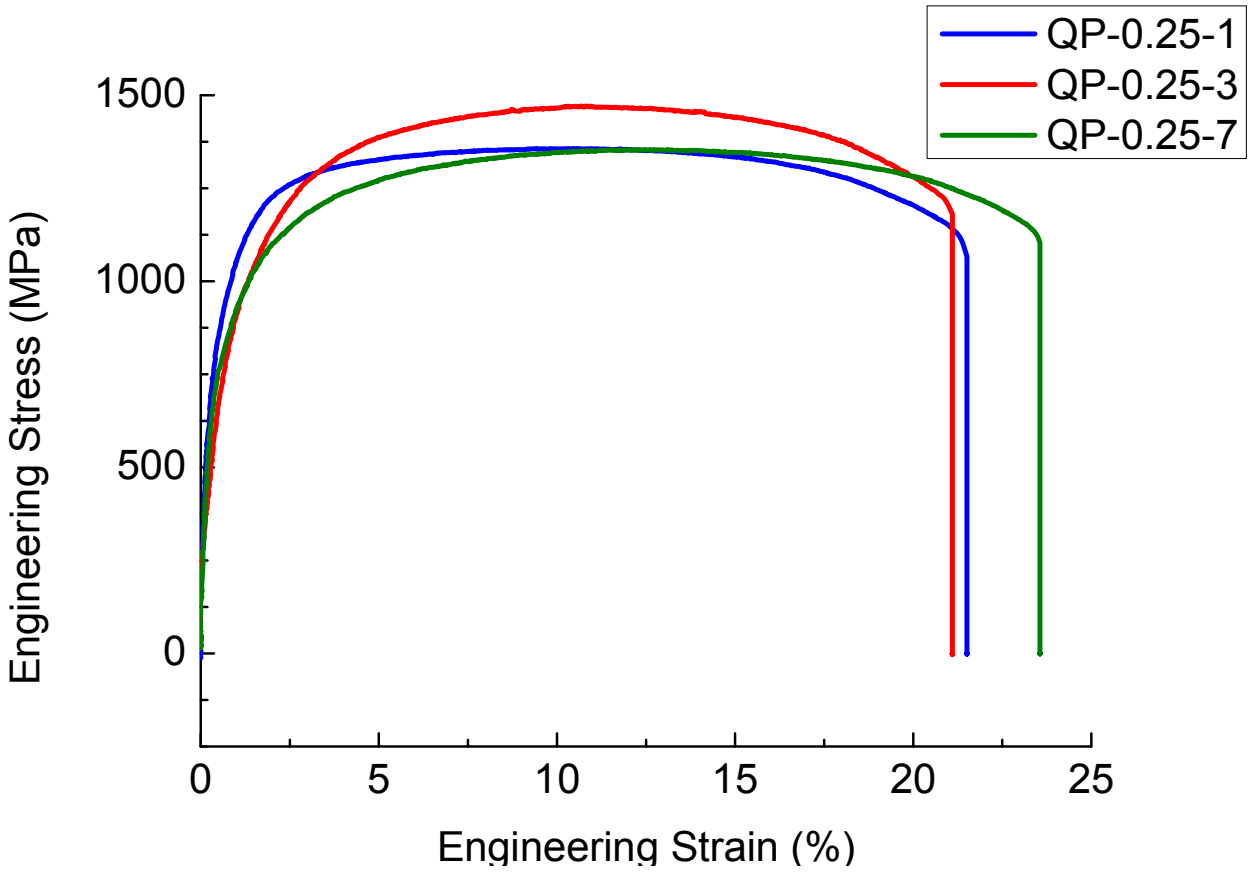

Figure 4-2. Engineering stress - engineering strain curves from tensile testing of the sample quenched at 224°C (QP-0.25-1), the sample quenched at 244°C (QP-0.25-3) and the sample quenched at 264°C for 500 s (QP-0.25-7). All of them were partitioned at 350°C for 500 s.

Figure 4-2 shows the engineering stress – engineering strain curves from tensile testing of the QP-0.25-1, QP-0.25-3 and QP-0.25-7 samples. In addition, their mechanical properties are summarized in Table 4-4. In TRIP steels, it is known that not only the volume fraction of RA, but also its transformation stability plays an important role in determining the global mechanical properties [60, 77, 79, 80]. In fact, similar behavior has also been reported in Q&P steels [20, 21]. It has also been already shown in literature that transformation stability of austenite is affected by many factors, among others the carbon concentration in the austenite grains [84, 87], its grain size [88], the constraining effect of the surrounding phases [92] and its morphology [77]. In this case, carbon content, grain size and the surrounding phases of RA (fractions of TM and UM) are very similar for the QP-0.25-1, QP-0.25-3 and QP-0.25-7 samples. Therefore, RA morphology should be the main factor explaining the difference in mechanical properties for the three studied conditions. RA presenting film-like or interlath lamellar morphologies have better transformation stability compared with a blocky type, which tends to transform to martensite under a small strain and contributes little to the TRIP effect [15, 16, 77, 78], as it is 'consumed' during the early stage of plastic deformation [20]. Thus, in the QP-0.25-3 sample containing mostly blocky type, RA suddenly transforms after yielding to martensite via TRIP effect [15, 16], whereas this might be not the case for interlath-lamellar RA or film-like RA. Therefore, after yielding the amount of UM, which contributes to the material's strength, is increased. This martensite will be different to that previously formed as it will normally be expected to inherit a higher carbon concentration [23, 184]. For this reason, the σ_{UTS} value for the QP-0.25-3 sample might be the highest one.

Slightly inferior $\sigma_{0.2}$ values are found for the QP-0.25-3 and the QP-0.25-7 samples. Yielding in these two steel grades should start earlier, considering that the blocky RA is deformed plastically before its transformation via TRIP effect. Besides, this agrees well with the observed strain hardening behavior. The more stable RA progressively transforms during the whole straining process, resulting in higher work hardening rate [60, 109], that, in turn, delays the onset of necking. After necking, ductility may be enhanced due to the contribution of the high volume fraction of film-like RA that is presented in the three steel grades. For this reason, both ε_u and ε_f are very similar for the three samples (Table 4-4).

4.1.1.2. Influence of PT

In order to determine the effect of PT, the target QT was set to 244°C, followed by isothermal holding during 500 s at different PT (300°C, 350°C and 400°C). The RA average size is enlarged with increasing PT (0.4 ± 0.1 µm, 0.6 ± 0.1 µm and 0.7 ± 0.1 µm, respectively). However, the PT does not have any influence on the TM average size (Table 4-2), as it is determined by the prior austenite grain size [185, 186] and, to some extent, by the QT (Section 4.1.1.1). The RA volume fraction obtained for the sample partitioned at 400°C is nearly 4 % higher than for the other two samples (Table 4-3). The effect of PT on microstructure has already been studied in previous works. Increasing PT accelerates the carbon partitioning from martensite to austenite [12]. For example, it was reported in [184] that for the same QT and Pt, the maximum RA volume fraction is reached at shorter times for higher PTs, i.e. carbon diffusion during partitioning is controlled more effectively by PT rather than Pt. These observations are in good agreement with the obtained results.

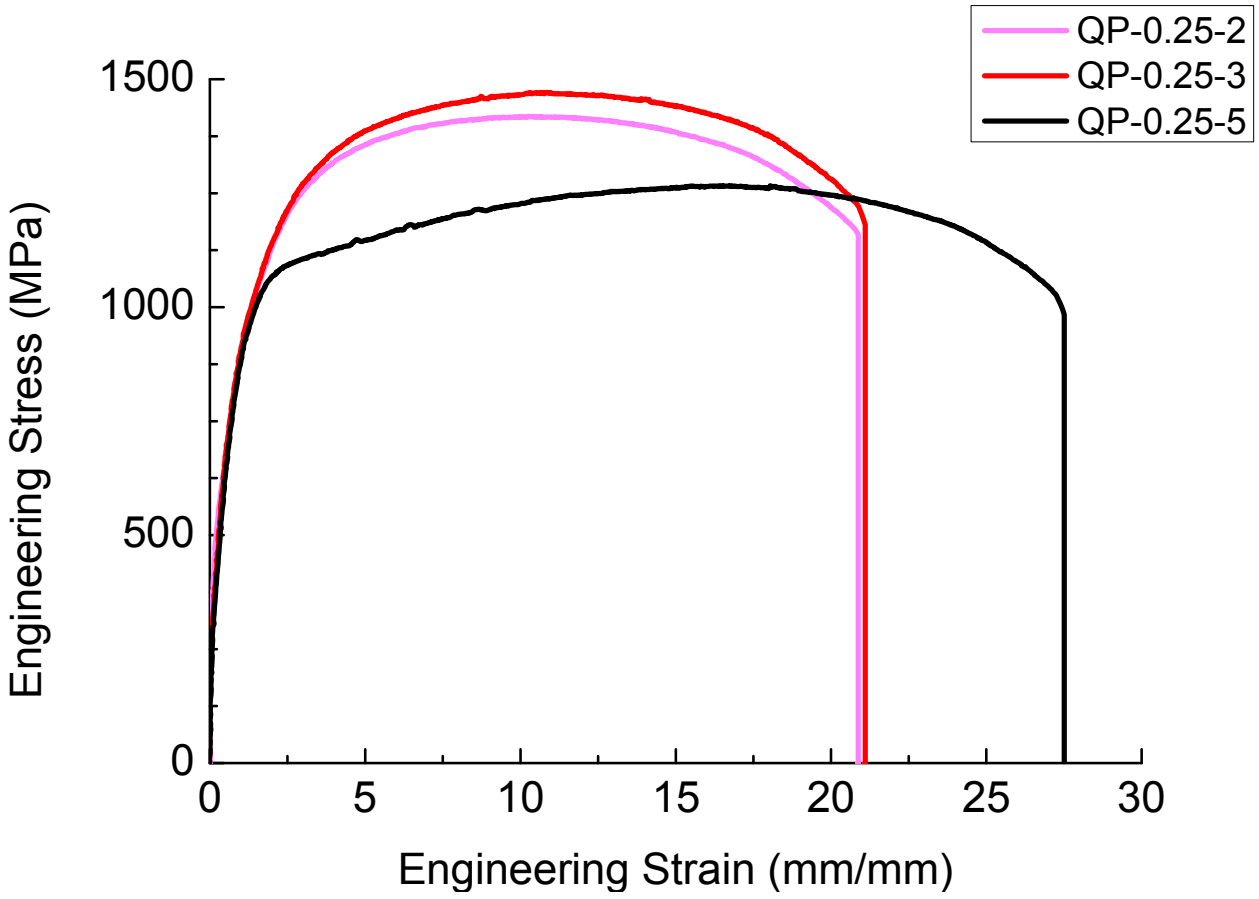

Figure 4-3. Engineering stress - engineering strain curves from tensile testing of the sample partitioned at 300°C for 500 s (QP-0.25-2), the sample partitioned at 350°C for 500 s (QP-0.25-3) and the sample partitioned at 400°C for 500 s (QP-0.25-5); all of them were quenched at 244°C.

Engineering stress - engineering strain curves in Figure 4-3 show the effect of PT on mechanical behavior of the Q&P processed steel. It is seen that the mechanical behavior of the samples partitioned at 300°C and 350°C (σ_{UTS}, ε_f and n) is very similar. For temperatures above 350°C, ultimate tensile strength and strain hardening exponent decrease with increasing PT, whereas ductility shows an opposite trend (Table 4-4). Higher volume fraction of RA (Table 4-3) and larger RA grains (Table 4-2) in the QP-0.25-5 sample result in softening of the material and improvement of its ductility, compared to the Q&P steel grades with the lowest RA content (QP-0.25-2 and QP-0.25-3 samples).

4.1.1.3. Influence of Pt

The influence of Pt on microstructure and mechanical properties of a Q&P steel was also investigated in this work. Samples were partitioned at 400°C for 100 s, 500 s and 1000 s (QP-0.25-4, QP-0.25-5 and QP-0.25-6, respectively) (Table 4-1). The EBSD phase maps of the three samples partitioned for different times are shown in Figure 4-1 g, h and i. Regarding the RA morphology, a mixture of interlath lamellar and blocky type can be found in the three conditions. The RA average size is enlarged from 0.5 µm to 0.7 µm, when Pt is raised from 100 s to 500 s (Table 4-2); however, it seems to stabilize with further partitioning until 1000 s. Apparently, increasing Pt does not have any influence on the TM grain size (Table 4-2). When Pt is increased from 100 to 500 s, the fraction of RA remains almost constant but its carbon content shows an increment from 0.84 % to 1.03 %. With further partitioning until 1000 s, there is an increment in the RA fraction of up to ≈ 20 %, but its carbon content remains approximately constant around 1 % (Table 4-3).

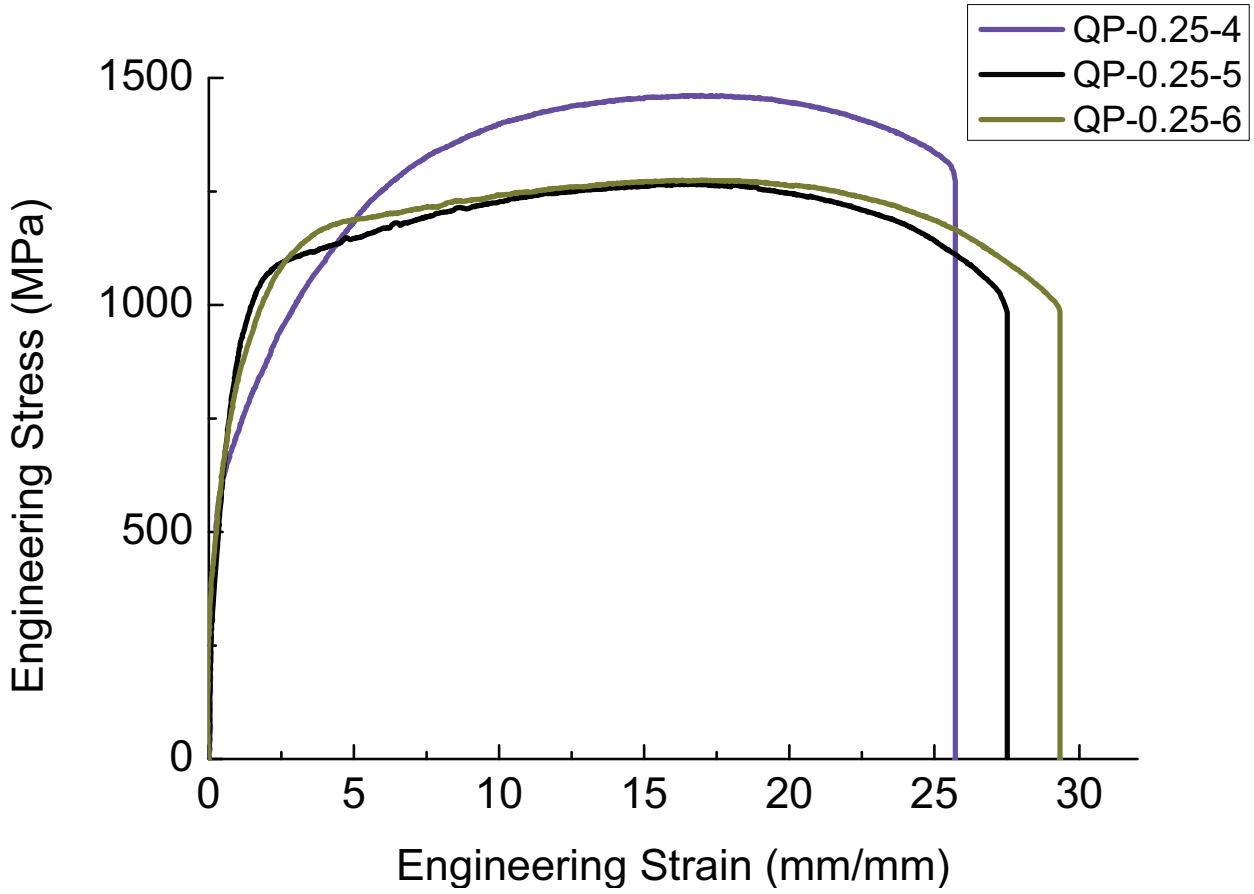

Figure 4-4. Engineering stress - engineering strain curves from tensile testing of the sample partitioned at 400°C for 100 s (QP-0.25-4), the sample partitioned at 400°C for 500 s (QP-0.25-5) and the sample partitioned at 400°C for 1000 s (QP-0.25-6); all of them were quenched at 244°C.

Figure 4-4 displays the engineering stress – engineering strain curves from tensile testing of the QP-0.25-4, the QP-0.25-5 and the QP-0.25-6 samples. Mechanical properties are also summarized in Table 4-4. Ductility seems to be directly related to Pt: increasing ε_f values of 26 %, 27 % and 29 % are reported for partitioning during 100 s, 500 s and 1000 s, respectively (Table 4-4). The highest $\sigma_{0.2}$ value is obtained for the QP-0.25-5 sample, with a value of ≈ 820 MPa. This could be explained as this sample contains the highest UM fraction (Table 4-4). It is well known that steels with martensitic microstructure offer an excellent yield strength of about 1000 MPa [187]. Regarding σ_{UTS}, the highest values are found in the sample with smaller RA grain sizes (QP-0.25-4), following the same tendency reported in Section 4.1.1.2. Finally, the strain hardening behavior is very similar for the QP-0.25-5 and the QP-0.25-6 samples. The same RA morphology, average grain size and carbon content is found in both samples, so they present a weaker transformation stability compared to the QP-0.25-4 sample [188]. This correlates well with the recent study in [77], where

higher carbon, blocky RA in a Q&P steel transformed to martensite at the onset of deformation, whereas lower carbon film-like RA remained stable up to 12.5 % global strain.

4.1.2. Textures after Q&P treatment

Figure 3 represents the orientation distribution functions (ODFs) in ϕ_2 = 0°, 45° and and 65° sections of Euler space for samples QP-0.25-2 (a) and QP-0.25-3 (b). The textures are calculated only for RA in the material after hot rolling, cold rolling and subsequent Q&P heat treatment. For the sake of simplicity, two samples with similar RA fractions (Table 4-3) but different grain sizes (Table 4-2) are shown.

The textures of RA (Figure 4-5 a and b) are similar and rather weak, with maxima of 2.85 and 3.63 mrd (multiples of a random distribution) occurring for the Brass (B) {011} ⟨112⟩ component in samples (a) and (b) respectively. Goss (G) {110} ⟨001⟩, Rotated Goss (RG) {110} ⟨110⟩, S {123} ⟨634⟩ and Copper (C) {211} ⟨111⟩ also occur in both samples, while the weak rotated cube (RC) {001} ⟨110⟩ is only present in the QP-0.25-2 sample. A slight rotation of the S' {123} ⟨634⟩ component can be observed for the QP-0.25-2 sample as well. In summary, the major difference in the texture components of austenite between both samples is the presence of the RC texture component in the QP-0.25-2 sample. The transformation potential of this component is between 0.05 and 0.08 with a minimum and maximum of 0.03 and 0.13 respectively [95]. A high transformation potential indicates low transformation stability related to the texture of the RA grain. Therefore, RA grains having this crystallographic orientation are relatively stable (not taking into account other effects such as RA grain size, carbon concentration, morphology, etc...). Hence in this sample, there are more austenite grains which will transform at higher strains resulting in more strain hardening. This can be observed experimentally by the higher σ_{UTS} in the stress-strain curves (Figure 4-3).

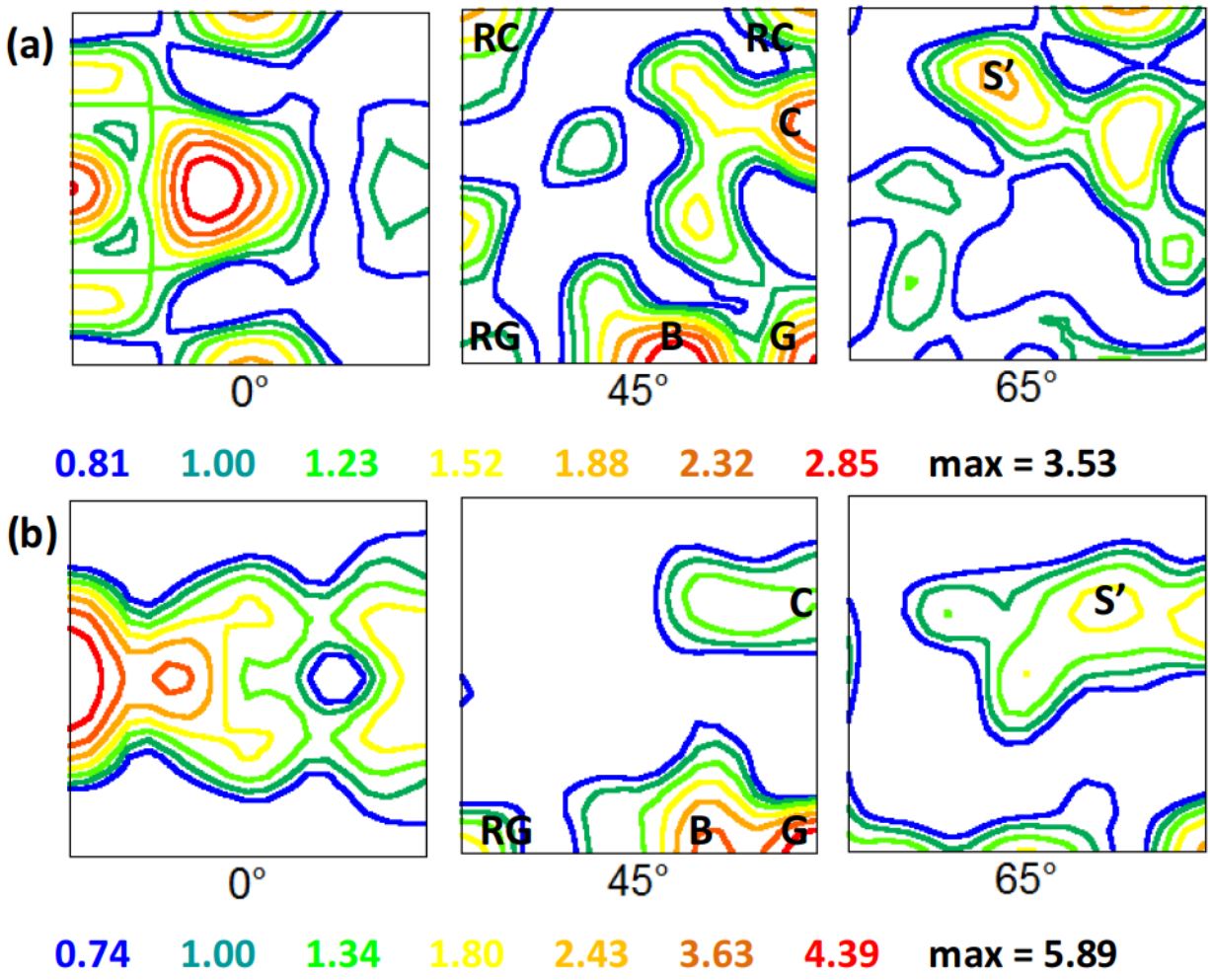

Figure 4-5. Orientation distribution functions (ODFs) in ϕ_2 = 0°, 45° and 65° sections for RA in sample QP-0.25-2 (a) and QP-0.25-3 (b). (RC = Rotated Cube, C = Copper, RG = Rotated Goss, B = Brass and G = Goss).

On the other hand, as it can be seen in Figure 4-6, the martensite has a crystallographic texture which is frequently observed after double α–γ–α transformation of cold deformed BCC phase in AHHSs [21]. This is because the crystallographic texture has not changed much as a consequence of the Q&P treatment given to the as-received steel [189, 190]. All texture components observed in the BCC structure originate from deformed austenite with a good agreement with the observed texture of the retained austenite. Note that despite using identical color scales, there are differences in the strength of the textures (Figure 4-5 and Figure 4-6).

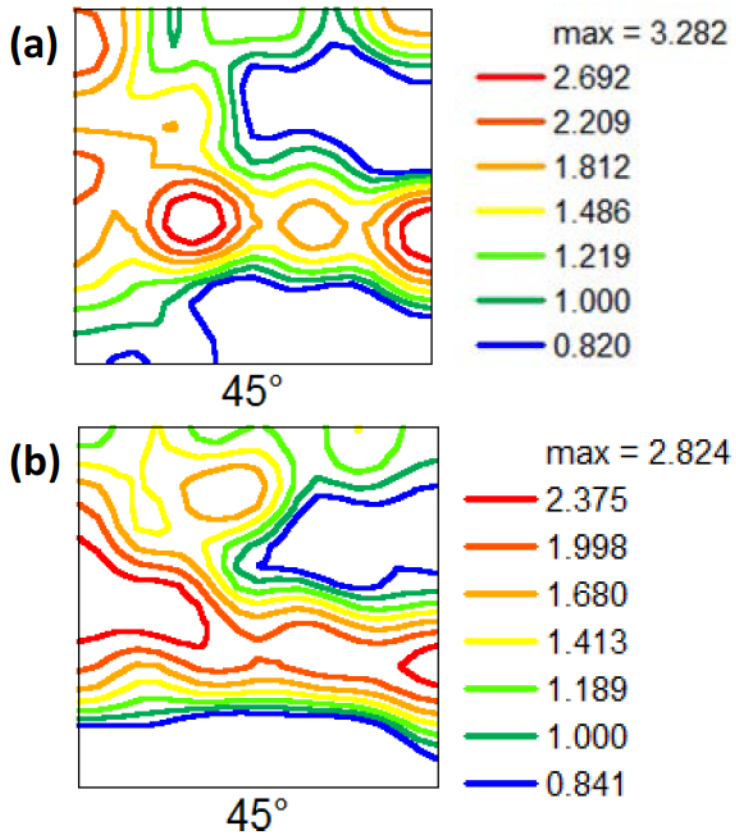

Figure 4-6. Orientation distribution functions (ODFs) in $\phi_2 = 45°$ sections for martensite in sample QP-0.25-2 (a) and QP-0.25-3 (b).

4.1.3. Conclusions to Section 4.1

Steel with the QP-0.25 nominal composition was subjected to Q&P treatment with varying QT, PT and Pt. Multiphase microstructure consisting of different fractions of TM, UM and RA was obtained. The effect of Q&P parameters on the microstructure, texture and tensile mechanical properties was thoroughly studied. It was shown that:

- The QT does not affect significantly the size and volume fraction of microconstituents, though the morphology of RA strongly depends on QT. Interlath lamellar RA prevails in the microstructure of the samples quenched at 224°C and 264°C which has high stability against transformation under strain, whereas blocky type RA dominates in the microstructure of the samples quenched at 244°C. The latter has low stability against transformation under strain which results in higher ultimate tensile strength.
- The PT has a strong effect on size and volume fraction of microconstituents and mechanical properties of the Q&P steel. The RA average size increases with increasing PT, and the highest RA volume fraction is reached after

partitioning at 400°C due to effective control of carbon diffusion by PT. However, high PT reduces mechanical strength and strain hardening exponent of the material, though its ductility is enhanced.

- The influence of Pt at 400°C on the size and volume fraction of microconstituents is ambiguous. The RA average size tends to grow with increasing Pt up to 500 s followed by its saturation, whereas RA volume fraction is not sensitive to Pt below 500 s and increases after partitioning for 1000 s. The material shows the highest ultimate tensile strength and strain hardening exponent at the shortest Pt followed by their significant reduction and slight gain in ductility with further increase of the Pt.
- There is no significant influence of Q&P parameters on the texture of RA. The main observed components include Brass {011} ⟨112⟩, Goss {110} ⟨001⟩, Rotated Goss {110} ⟨110⟩, and Copper {211} ⟨111⟩. The weak rotated cube {001} ⟨110⟩ is only present in the QP-0.25-2 sample. RA with the latter orientation has higher stability, resulting in the highest ultimate tensile strength for this Q&P condition. The Q&P parameters have no effect on crystallographic texture of martensite. It is similar to the texture frequently observed after double α–γ–α transformation of cold deformed BCC phase in AHHSs.

4.2. Global and local deformation behavior and mechanical properties of individual phases in the Q&P steels

In this section, the effect of Q&P parameters on the microstructure and morphology of microconstituents is analyzed. For this purpose, the QP-0.25-2, QP0.25-4 and QP-0.25-5 samples were chosen. Then, nanoindentation was employed to study mechanical properties of their individual microconstituents, which were identified *a priori* by EBSD analysis. Special attention was paid to the effect of the morphology of RA on its transformation stability. *In situ* tensile tests and digital image correlation analysis were performed to study the deformation behavior of the Q&P processed steel at the micro-scale with respect to the local microstructure. The effect of local microstructure and properties of individual phases on the degree of strain partitioning is discussed below.

4.2.1. Properties of the individual microconstituents in the Q&P steel

An OIM map of the area selected for nanoindentation in the QP-0.25-5 specimen and an AFM image of residual indents left by the nanoindenter on the same area are presented in Figure 4-7. It is clearly seen that the indentations were performed on individual phases, so their individual properties could be analyzed.

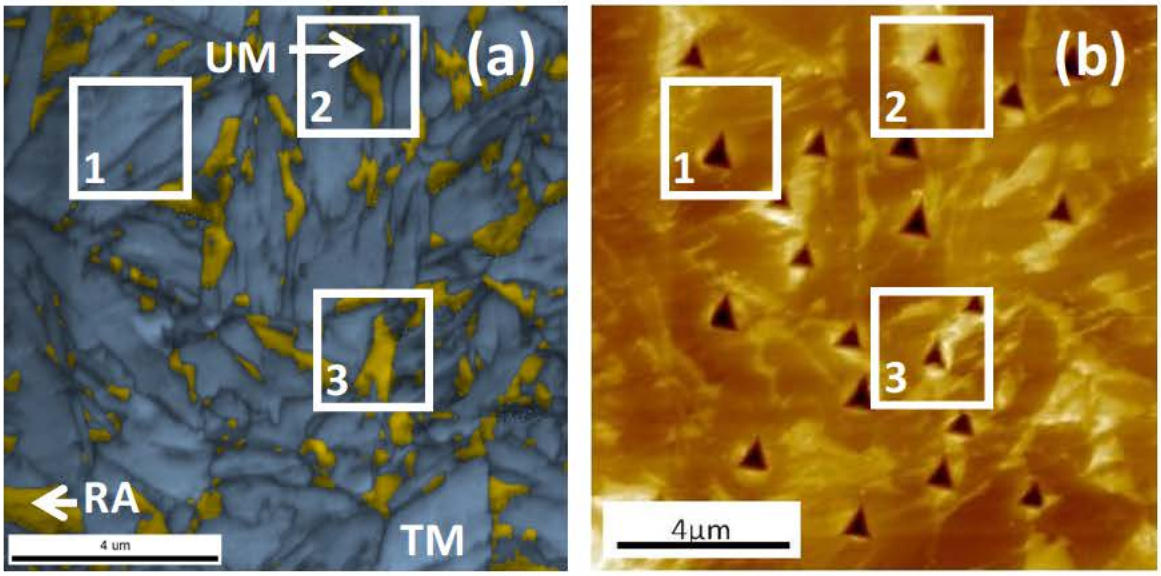

Figure 4-7. (a) OIM map and (b) residual indents imaged by AFM in the sample partitioned at 400°C for 500 s (QP-0.25-5).

The elasto-plastic material properties obtained from the nanoindentation tests are summarized in Table 4-5. Nanohardness of RA was measured only in the specimens partitioned at 400°C (QP-0.25-4 and QP-0.25-5), with larger RA grain sizes (Table

4-2). Nanohardness values of 6.4 ± 1.2 GPa and 5.5 ± 0.5 GPa were measured for partitioning times of 100 s (QP-0.25-4) and 500 s (QP-0.25-5), respectively (Table 4-5). In addition, the elasto-plastic properties obtained for the UM provide nanohardness values of 6.6 ± 0.8 GPa and 8.8 ± 0.9 GPa for the QP-0.25-2 and QP-0.25-4 specimens, respectively. Nanoindentation tests on TM yield very similar nanohardness values for all studied conditions, i.e. 5.3 ± 0.4 GPa, 5.6 ± 0.4 GPa and 5.6 ± 0.5 GPa (Table 4-5).

Table 4-5. Elasto-plastic material properties obtained from the nanoindentation tests for the RA, TM and UM (nanohardness H).

Specimen		Retained Austenite H (GPa)	Tempered Martensite H (GPa)	Untempered Martensite H (GPa)
QP-0.25-	2	-	5.3 ± 0.4	6.6 ± 0.8
	4	6.4 ± 1.2	5.6 ± 0.4	8.8 ± 0.9
	5	5.5 ± 0.5	5.6 ± 0.5	-

Next, the radius of the plastic zone for individual indents was estimated in order to validate the results presented in Table 4-5. The contact radius a' was obtained using the equation:

$$a' = \sqrt{A/\pi} \qquad \text{(Eq. 4-2)}$$

where A is the projected contact area of the indent. In the case of the TM microconstituent a' was found to be 314.6 ± 1.6 nm. For Berkovich tips, the ratio between the radius of the plastic zone c and the contact radius a' is determined as [191, 192]:

$$c/a' = 3.4 \qquad \text{(Eq. 4-3)}$$

From this ratio, the radius of plastic zone was calculated for each microconstituent. The radius of the plastic zone in TM (1.07 ± 0.005 μm) is well below of the TM block size consisting of several laths with identical crystal orientations, so plastic deformation occurs strictly in the interior of the blocks, validating the nanohardness values. The radius of plastic zone in RA (1.06 ± 0.001 μm) exceeds the size of RA

grains (see Table 4-2), extending into the surrounding microconstituents. As other phases have higher hardness, it can be concluded that nanohardness values of RA presented in Table 4-5 are overestimated. The radius of the plastic zone in the UM (1.04 ± 0.02 μm) should be comparable to the size of UM grains, which could not be precisely measured (see Section 4.1), so nanohardness data for this microconstituent presented in Table 4-5 are ambiguous. Nevertheless, as the nanohardness of the TM matrix is similar in all studied conditions, the elasto-plastic material properties obtained from the nanoindentation tests for the RA and the UM (Table 4-5) can be used for the comparative purposes.

The Q&P treatment aims at concentrating carbon in RA formed after the first quench [15, 16, 19]. Therefore, like in TRIP steels [60, 193], the martensite formed during the final quench to room temperature (UM) usually contains higher amount of carbon (≈ 0.6 - 1 wt. %) than before the treatment. This, in turn, should lead to higher solid solution hardening in the UM microconstituents. Nanoindentation measurements (Table 4-5) show that nanohardness of UM is at least 25 % higher compared to that of TM (sample QP-0.25-2), and this difference increases to 56 % with increasing partitioning temperature (sample QP-0.25-4), even though the partitioning time is reduced. Therefore, it can be concluded, that the carbon enrichment of the prior RA grain is more effectively controlled by partitioning temperature, and the carbon diffusion is enhanced by partitioning temperature rather than by time, as it was suggested in [21].

Representative load-displacement curves from nanoindentation experiments on RA are presented in Figure 4-8 a. Detailed analysis of the loading curves shows that interlath lamellar RA present in the specimen partitioned at shorter time (QP-0.25-4) has higher deformation resistance compared to that of the blocky RA prevailing in the specimen after longer partitioning (QP-0.25-5). This is demonstrated by the higher maximum load for the same penetration distance. In addition, evidence for martensitic transformation of RA, i.e. TRIP effect [60, 83, 109], during nanoindentation is observed on loading curves as small discontinuities or pop-ins, indicated by black arrows in Figure 4-8. It should be noted that such pop-ins were more often observed in the sample containing blocky RA rather than interlath lamellar RA, indicating higher stability of the latter type of RA. Particularly, at an indentation depth of ≈ 80 nm and applied loads of ≈ 1450 μN and ≈ 1150 μN (Figure 4-8 a), a slight rise of the curve slope after the pop-ins suggests that martensitic transformation results in increased hardness [62, 194]. Figure 4-8 b and

c show the (P/h) vs. h plots that were calculated from Figure 4-8 a. The slopes of the (P/h) vs. h plots at the early stage of plastic deformation are approximately 0.07 $\mu N \cdot nm^{-2}$ and 0.08 $\mu N \cdot nm^{-2}$ for the specimens QP-0.25-4 and QP-0.25-5, respectively. These slopes increase up to 0.11 $\mu N \cdot nm^{-2}$ and 0.13 $\mu N \cdot nm^{-2}$ with further loading (Figure 4-8 b and c).

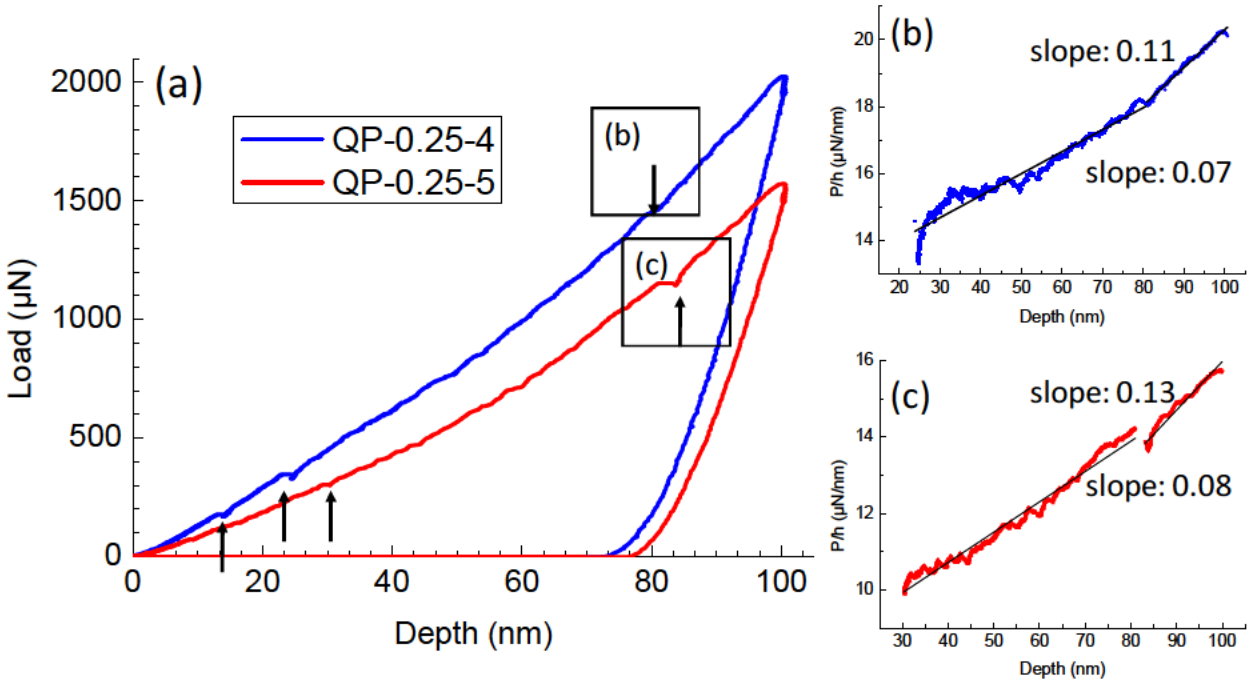

Figure 4-8. (a) Representative load-displacement curves from nanoindentation experiments on RA on the sample partitioned at 400°C for 100 s (QP-0.25-4) and the sample partitioned at 400°C for 500 s (QP-0.25-5). The load-displacement curves in (a) were converted into (P/h) vs. h curves of ≈1450 μN and ≈1150 μN in (b) and (c), respectively.

Comparison of two studied samples containing the highest volume fraction of RA (QP-0.25-4 and QP-0.25-5 samples) shows that the interlath lamellar RA prevailing in the specimen QP-0.25-4 is more stable during deformation than the blocky RA dominating in the specimen QP-0.25-5 [77]. Thus, the martensitic transformation of RA during plastic deformation, i.e. TRIP effect [60, 83, 109], in the specimen QP-0.25-4 occurs in a more continuous manner [21] and hence the lowest work hardening rate is obtained for the QP-0.25-5 sample (Table 4-4). From the nanoindentation experiments, it is seen that RA was also less stable in this sample (Figure 4-8). On the other hand, it follows from the stress - strain curves (Table 4-4), that the Q&P steel with the highest volume fraction of RA (QP-0.25-4 and QP-0.25-5 samples) shows higher ductility compared to the Q&P steel with lower RA content (QP-0.25-2 sample) (Table 4-3). It was already reported by several authors that RA

presenting film-like or interlath lamellar morphologies have better transformation stability compared with a blocky one [77, 78]. This agrees well with the strain hardening behavior as well as with the low ductility values of the QP-0.25-2 sample (Table 4-4), where the film-like RA is stable against deformation.

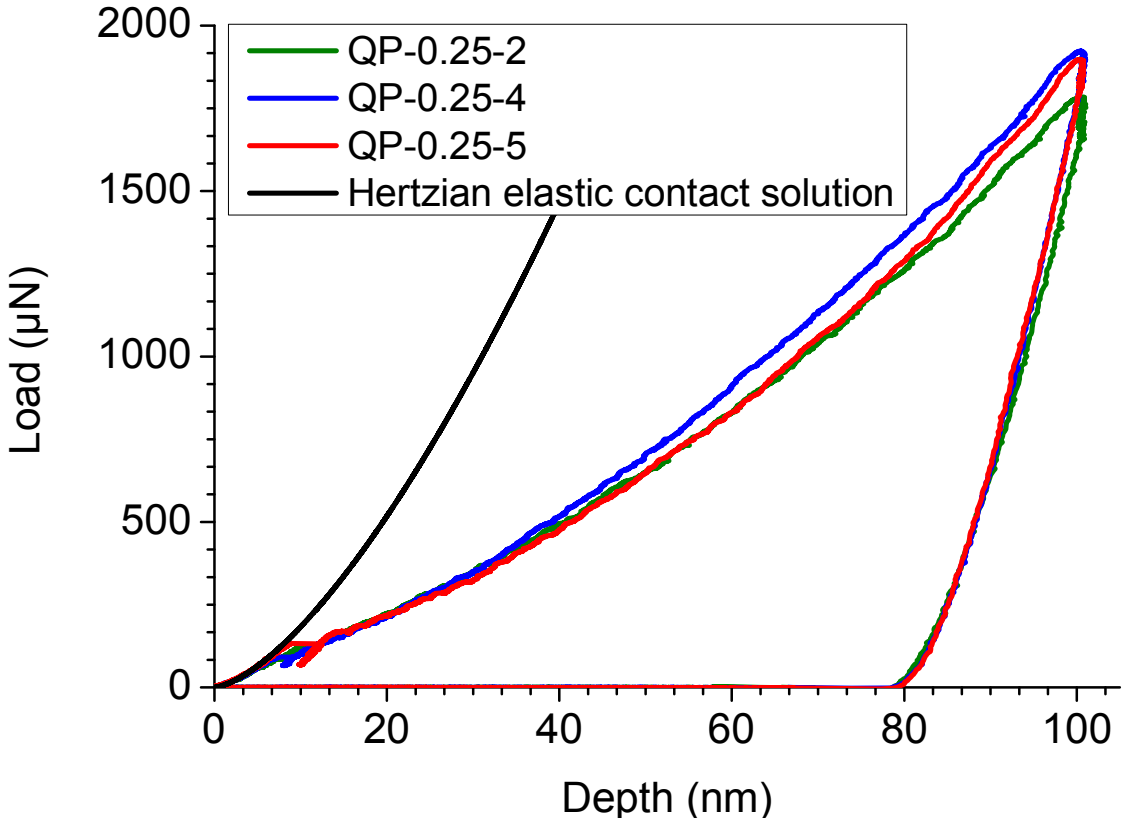

Figure 4-9. Representative load-displacement curves from nanoindentation experiments on TM in the studied steel.

Figure 4-9 shows the load-displacement curves from nanoindentation on individual TM grains in all studied Q&P specimens. A pop-in is observed on all curves at indentation depth of ≈ 8 nm and applied load of ≈ 10 μN. Since the first pop-in represents the transition from elastic to elasto-plastic deformation during indentation [62, 79, 195, 196], the stresses at pop-in during spherical indentation can be estimated from the Hertzian elastic contact mechanics as [195-197]:

$$P = \frac{4}{3} \cdot E_r \cdot \sqrt{R'} \cdot h^{1.5} \qquad \text{(Eq. 4-4)}$$

where E_r is the reduced indentation modulus, R' the radius of the Berkovich indenter tip (R' ≈ 450 nm), which was experimentally obtained by AFM, and h the corresponding indentation depth.

Before the first pop-in, the theoretical curve (black line in Figure 4-9) obtained from (Eq. 3-4), fits the experimental loading curve well, indicating that the part of loading curve before the first pop-in is elastic, while the rest of the loading curve is elasto-plastic. In [60], Furnémont *et al.* asserted that it is not possible to translate directly nanohardness values into plastic flow properties. Nevertheless, the maximum shear stress under the indenter along the symmetry axis at the first pop-in can be estimated using the relationship [195-198]:

$$\tau_{max} = 0.31 \cdot p_o \qquad \textbf{(Eq. 4-5)}$$

where

$$p_o = \left(\frac{6 \cdot P \cdot {E_r}^2}{\pi^3 \cdot R^2} \right)^{1/3} \qquad \textbf{(Eq. 4-6)}$$

according to the standard Hertzian analysis. Using (Eq. 3-5) and (Eq. 3-6) and the load at the first pop-in, τ_{max} was estimated as 4.5 ± 0.3 GPa, 5.1 ± 0.3 GPa and 5.1 ± 0.02 GPa for the QP-0.25-2, QP-0.25-4 and QP-0.25-5 specimens, respectively (Table 4-6). It is seen that the maximum shear stresses in TM in the specimens partitioned at 400°C (QP-0.25-4 and QP-0.25-5) are higher compared to that in the specimen partitioned at 300°C (QP-0.25-2).

Table 4-6. Maximum shear stress in TM underneath the Berkovich indenter.

Specimen		τ_{max}(GPa)
QP-0.25-	2	4.5 ± 0.3
	4	5.1 ± 0.3
	5	5.1 ± 0.02

As it is well known, the time required for effective partitioning is mainly determined by two factors: the expected RA volume fraction and the local carbon content affecting RA stability [21]. For a lower PT, the time necessary to obtain higher volume fraction of RA with higher carbon content is longer. Comparison of samples partitioned at different temperatures for 500 s shows that a lower volume fraction of RA is obtained in the sample partitioned at 300°C (QP-0.25-2), but with a comparable carbon content in both cases (Table 4-3), whereas the reduction of

partitioning time at 400°C results in decrease of RA carbon content (Table 4-3). As the QT was kept constant for all studied conditions [21, 28], the volume fraction of martensite formed during the first quenching should be similar (Table 4-3). Martensitic transformation imparts high elastic strain energies that can only proceed in combination with accommodation processes, which introduce high dislocation density into martensite [199]. Both solid solution hardening (tetragonal lattice is supersaturated by interstitial carbon atoms) and dislocation hardening (due to high dislocation density) result in high strength of martensite [60]. Carbon diffusion from martensite into RA and partial annihilation of dislocations in martensite by their climb occur simultaneously during partitioning step, and there is some interplay between both processes due to interactions between diffusing carbon and iron atoms and dislocations [16, 200]. Contribution of both hardening mechanisms into hardness of TM should depend on the Q&P parameters. However, the variations in the nanohardness values measured on TM microconstituent in all studied conditions are not high (Table 4-5). Glide of dislocations nucleated underneath the indenter tip is the main deformation mechanism in TM [198, 201-203]. Several studies suggest that the first pop-in shown in the TM phase (observed in Figure 4-9) occurs either due to nucleation of dislocations at the theoretical strength if there are no dislocations in the highly stressed zone, or due to activation of pre-existing dislocations [60, 62, 79, 196]. Both 'scenarios' are characterized by avalanches in the motion of dislocations resulting in a pop-in on the loading curve, though the maximum shear stress is lower in the latter case. The lower value of the maximum shear stress measured on TM in the QP-0.25-2 sample indicates higher density of pre-existing dislocations remained after partitioning process (Table 4-6). Indeed, lower partitioning temperature decreases dislocation climb controlled by diffusion process that reduces the amount of annihilated dislocations during partitioning process.

4.2.2. **Local plastic deformation of the Q&P steel**

The evolution of microscale plastic strain ε_{yy} distribution on the surface of the QP-0.25-5 specimen in the loading direction during *in situ* tensile testing is illustrated in Figure 4-10. The onset and development of a network-like structure of interconnected bands of localized plastic flow, oriented at 45° to 60° with respect to the loading axis, is clearly seen, whereas a significant fraction of little deformed areas remains present. High strains accumulate at spots connected by deformation bands (Figure 4-10 c).

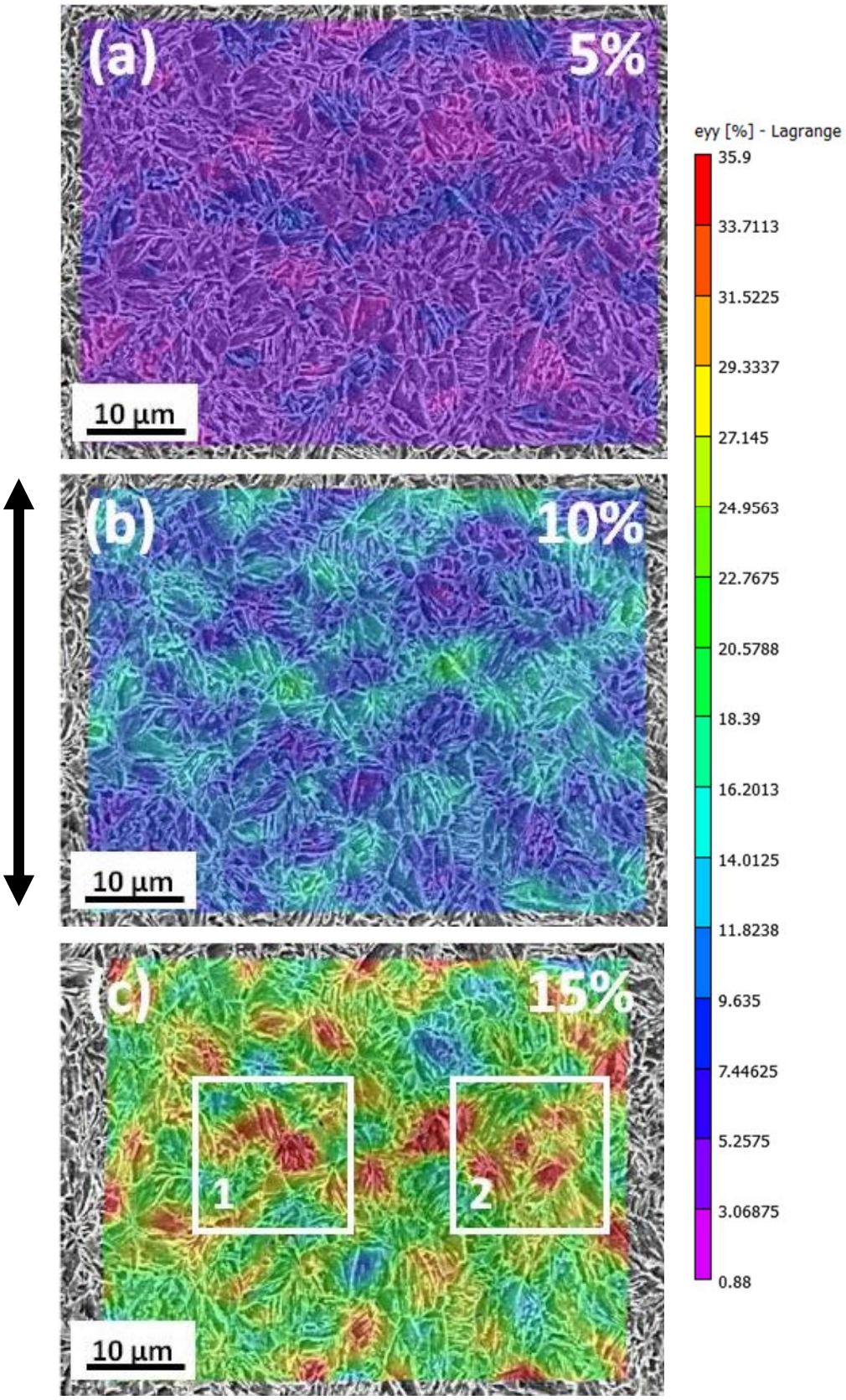

Figure 4-10. Evolution of in-plane local plastic strain distribution during tensile deformation of the sample partitioned at 400°C for 500 s (QP-0.25-5) to the global plastic strain of (a) 5 %, (b) 10 % and (c) 15 %. The loading direction is vertical (indicated by a black arrow).

Strong partitioning of local plastic strain between different phases is observed at all deformation steps (Figure 4-10 a-c). The degree of strain partitioning strongly increases with global plastic strain. Besides, the amount of plastic deformation accommodated by different phases is inversely proportional to their nanohardness. For instance, after plastic deformation to the global plastic strain of 15 % in the QP-0.25-5 sample, the maximum local plastic strain accommodated by TM reaches a value of ≈ 35.9 %, whereas it does not exceed ≈ 14 % in the UM. It is also seen that UM blocks often act as effective barriers, at which deformation bands stop or bend (Figure 4-10 a and b). Plastic strain accommodated by individual UM grains does not seem to depend on their morphological orientation with respect to the loading axis. Nevertheless, in the case of TM, plastic strain accommodated by each grain is determined to some extent by the orientation of its former laths. The amount of plastic strain accumulated by grains with their laths perpendicular or inclined at ≈ 45° with respect to the tensile axis is higher compared to those that are parallel to the loading axis. Blocks consisting of several grains with less resistant orientations (marked by squares 1 and 2 in Figure 4-10 c) are preferable sites for nucleation of deformation bands. Plastic deformation begins with localized plastic flow in the soft phases, and dislocation hardening in the soft phases spreads the plastic deformation into the harder phases. Deformation bands tend to propagate through grains of less resistant morphological orientations, whereas UM grains and even TM grains with parallel laths to the loading axis act as effective barriers for their propagation.

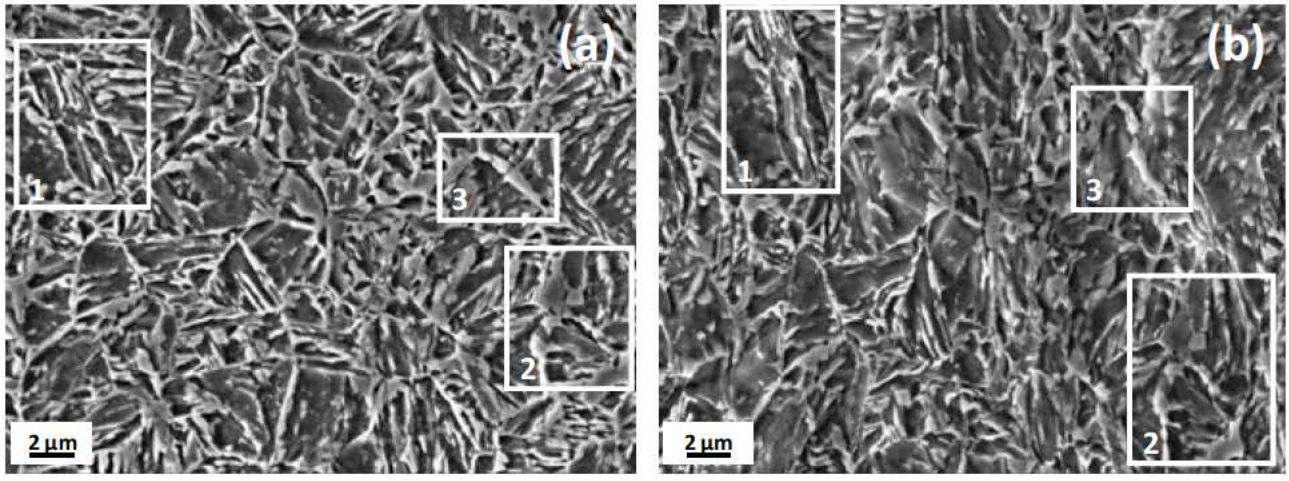

Figure 4-11. SEM images of the sample partitioned at 400°C for 500 s (QP-0.25-5): (a) initial microstructure; (b) microstructure after tensile deformation to the global plastic strain of ≈ 22 % (necking area).

Figure 4-11 shows SEM images taken from the QP-0.25-5 sample in the non-deformed state (Figure 4-11 a) and after tensile deformation to the global plastic

strain of 22 % (Figure 4-11 b). In the areas where hard phases are present (UM blocks), the large difference in strength between microconstituents results in localization of plastic deformation in a softer TM matrix, that can also lead to slight rotation of microconstituents (rectangles 1 and 2). Local rupture at the interphase boundaries due to the localized plastic flow can be seen inside the necking area (white arrow in rectangle 3).

The network-like plastic deformation maps observed in this work are similar to those reported earlier for inter-critically annealed Q&P steels [20], DP steels [69-71, 163] and MMCs [76]. The difference in mechanical properties of individual microconstituents in materials with multiphase microstructures can significantly affect the degree of strain partitioning during plastic deformation [67, 68]. Other factors affecting plastic deformation maps include morphology of microconstituents, their volume fraction, bonding strength between microconstituents, etc. The results presented in this work demonstrate that nanohardness of microconstituents present in the Q&P steel can vary significantly (see Section 1.3.2). That, in turn, results in significant strain partitioning during plastic deformation of the Q&P steel. Plastic deformation tends to accumulate in the 'soft' microconstituents, whereas 'hard' microconstituents provide less contribution to plastic deformation. For this reason, TM is deformed according to morphological restrictions and even rotation of TM grains can be observed in some cases (Figure 4-11). In addition, the strain experienced by the softer phase (TM) can be much higher than the macroscopically imposed strain (Figure 4-10). This effect is even enhanced when the TM is trapped between harder UM blocks (rectangle 2 in Figure 4-11 a and b). These results are analogous to those reported by Han *et al.* [67] for a DP steel.

Figure 4-12 and Figure 4-13 show the evolution of microscale plastic strain ε_{yy} distributions on the surface of the QP-0.25-2 and QP-0.25-4 specimens, respectively. It is seen that local plastic deformation behavior of both specimens is quite similar to that described above for the QP-0.25-5 specimen.

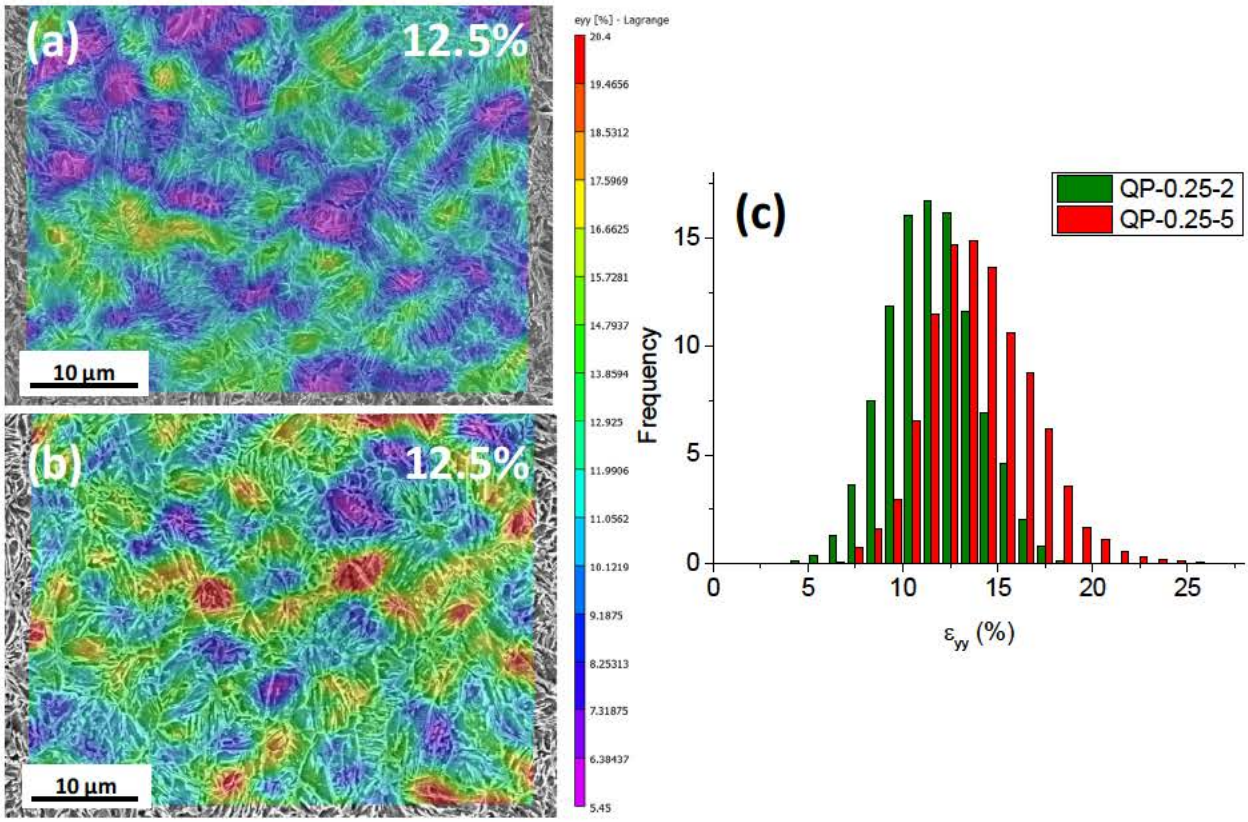

Figure 4-12. Distribution of local plastic strain on surface of the sample partitioned at 300°C for 500 s (QP-0.25-2) (a) and the sample partitioned at 400°C for 500 s (QP-0.25-5) (b) after tensile deformation to a global plastic strain of 12.5 %. Histograms of plastic strain distribution for both samples (c).

For the QP0.25-2 sample, local plastic strain values are found to be in the range between 2.8 % and 17.4 %, with an average value of 13.0 ± 2.8 %, whereas for the QP-0.25-5 sample the local plastic strain has values between 5.7 % and 25.6 % with an average value of 13.0 ± 2.7 % (Figure 4-12). The same comparison is shown in Figure 4-12 for samples QP-0.25-4 and QP-0.25-5. In this case, the local plastic deformation values for the QP-0.25-4 sample are distributed between 5.1 % and 19.7 % with an average value of 10.7 ± 2.7 %. From Figure 4-13 c, it can be seen that for the same global plastic strain, local plastic strain tends to have higher values in the case of the QP-0.25-5 sample.

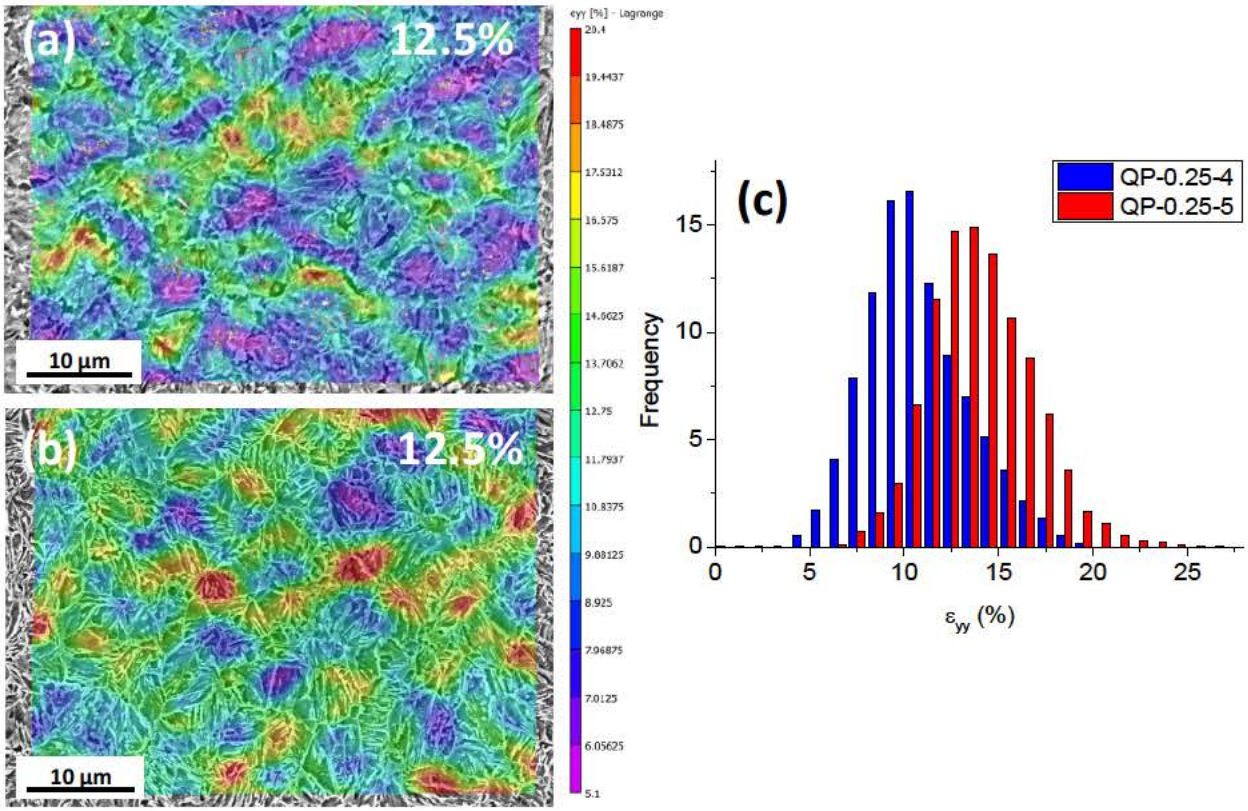

Figure 4-13. Distribution of local plastic strain on surface of the sample partitioned at 400°C for 100 s (QP-0.25-4) (a) and the sample partitioned at 400°C for 500 s (QP-0.25-5) (b) after tensile deformation to a global plastic strain of 12.5 %. Histograms of plastic strain distribution for both samples (c).

As was already discussed above, martensitic transformation of RA plays a very important role in plastic deformation of the Q&P steels. It can be hypothesized that different morphologies of RA and their different stability after different Q&P treatments affect plastic deformation maps, though this effect can be hardly quantified in the present work. Nevertheless, the elasto-plastic materials properties obtained from the nanoindentation tests in the QP-0.25-5 sample (Table 4-5) and the global strain hardening behavior obtained from tensile testing confirm that the blocky RA in the QP-0.25-5 sample has low stability, and it is 'consumed' during the early stage of tensile deformation. Furthermore, the change in slope of the (P/h) vs. h plots is believed to be the consequence of the change in the predominant deformation mode (Figure 4-8 a-c) [194]. This means that for a 12.5 % global plastic strain, most of blocky RA is transformed to martensite, whereas this might be not the case for interlath-lamellar RA or film-like RA. In addition, the constrained TM relaxes with the volume expansion during the austenite-martensite transformation [20, 204]. Martensite transformation leads to an increase in volume such that the stress surrounding TM, increases the work hardening rate [80]. For this reason, the

average local plastic strain value as well as the distribution of the local plastic strain for the QP-0.25-2 and QP-0.25-5 samples in Figure 4-12 c are very similar, but the local plastic strain tends to have higher values in the QP-0.25-5 sample [101].

4.2.3. **Conclusions to Section 4.2**

The effect of Q&P parameters (PT and Pt) on the microstructure and mechanical properties of the QP-0.25 composition was studied. Plastic deformation of the Q&P processed steel was carefully analyzed at macro- and micro-scales via *in situ* testing, DIC analysis and nanoindentation on individual microconstituents determined *a priori* by EBSD analysis. It was demonstrated that:

- The Q&P parameters significantly affect the microstructure of the studied steel, including size, morphology, and distribution of microconstituents (RA, TM and UM), as well as the carbon content in individual phases. Carbon diffusion during partitioning is controlled more effectively by partitioning temperature rather than time.
- Mechanical properties of individual microconstituents are strongly influenced by the Q&P parameters. Nanoindentation measurements on TM showed that the maximum shear stresses underneath the indenter tip in the specimens partitioned at 400°C are higher compared to that in the specimen partitioned at 300°C. This is related to the lesser annihilation of dislocations in martensite at 300°C, that leaves higher density of pre-existing dislocations, which, in turn, results in lower maximum shear stress.
- Plastic deformation of all Q&P steels at microscale level has a complex character. Plastic deformation maps consist of network-like plastic deformation bands interconnected at high strain spots. There is a weak effect of the Q&P parameters on histograms of local plastic strain distribution that is related to volume fraction of individual microconstituents as well as morphology (i.e. stability) of RA.

4.3. Fracture behavior of Q&P steels

This chapter addresses the effect of microstructural architecture in multiphase Q&P steels on their fracture behavior at macro- and micro-scales. Fracture behavior of three Q&P steels (the QP-0.25-5, QP-0.28-1 and QP-0.28-2 samples) is carefully studied with respect to their microstructure and fracture mechanisms are analyzed. It is demonstrated that the RA volume fraction does not affect significantly the local fracture initiation toughness, whereas it can greatly improve the total crack growth resistance in Q&P steels. In addition, matrix conditions can play an important role in the fracture behavior of Q&P steels. Based on the analysis of the experimental results, a general recipe to tailor fracture properties of Q&P steels is proposed.

4.3.1. Microstructure and mechanical properties

OIM phase maps with BCC in blue and FCC in yellow superimposed with the image quality of the studied samples are shown in Figure 4-14.

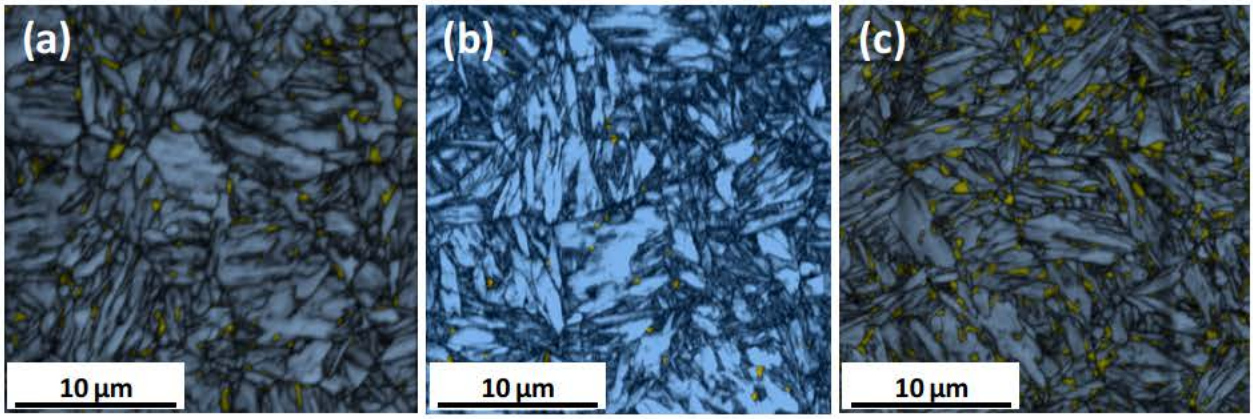

Figure 4-14. OIM maps of (a) the QP-0.25-5 sample, (b) the QP-0.28-1 sample and (c) the QP-0.28-2 sample.

After all Q&P treatments, irregular-shaped blocks of TM constitute the major phase of the microstructure, whereas the others (i.e. UM and RA) are dispersed in the matrix. Due to a less perfect BCC lattice, UM regions formed during the last quench to room temperature can be identified as the darkest ones, which can be found in the vicinity of the yellow RA grains. The size of the UM can be roughly estimated but could not be accurately measured from the available OIM maps, since lattice distortion leads to a low pattern quality and indexation of the UM zones in the OIM scans. Information on the size of the microconstituents (TM and RA) is provided in Table 4-7.

Table 4-7. Average grain size (equivalent circle diameter) for the different microconstituents of the Q&P steel grades.

Specimen	Tempered martensite (TM) (μm)	Retained austenite (RA) (μm)
QP-0.25-5	3.1 ± 0.2	0.6 ± 0.1
QP-0.28-1	2.3 ± 0.1	0.3 ± 0.04
QP-0.28-2	2.3 ± 0.2	0.7 ± 0.1

The average size of TM for the QP-0.28-1 and the QP-0.28-2 specimens is in the same range, being 2.3 ± 0.1 μm and 2.3 ± 0.2 μm, respectively. However, a slightly higher value of 3.1 ± 0.2 μm is found in the case of the QP-0.25-5 sample. Regarding the RA average grain size, the value obtained for the QP-0.28-1 is half of that obtained for the other two samples, being 0.3 ± 0.04 μm, 0.6 ± 0.1 μm and 0.7 ± 0.1 μm, respectively. Various RA morphologies are present in the microstructure (Figure 4-14): film-like RA, lamellar RA and blocky RA. A thorough analysis of the available OIM micrographs shows that the prevalent type in the QP-0.28-1 sample is the film-like one, whereas in the QP-0.25-5 it is the blocky one. In the QP-0.28-2 a mixture of blocky RA and lamellar RA can be found. Although the spatial resolution of the EBSD technique is reasonably high (step size is ≈ 40 nm), the smallest austenite laths formed between the martensite plates, as observed with TEM, have sizes in the range of 20–100 nm [21, 77]. These laths can therefore not be resolved by EBSD but are detectable with XRD. Table 4-8 lists the measurements of volume fraction and carbon content of RA fraction, as well as the volume fraction of TM and UM which were determined by X-ray diffraction combined with EBSD analysis. Average volume fractions of RA 11.5 %, 7.5 % and 23.8 % with carbon contents of 0.92, 1.1 and 1 wt. % were measured in the QP-0.25-5, the QP-0.28-1 and the QP-0.28-2 samples, respectively (Table 4-8). On the other hand, localized EBSD scans yield significantly lower RA fractions, being 2.5 %, 1.2 % and 9.9 % for the QP-0.25-5, QP-0.28-1 and the QP-0.28-2 samples, respectively.

Table 4-8. Volume fraction and carbon content (wt. %) of RA and volume fraction of UM and TM in the studied steel grades.

Specimen	Retained austenite (RA)		Untempered martensite (UM)	Tempered martensite (TM)
	(%)	% C (wt.)	(%)	(%)
QP-0.25-5	11.5	1.1	10.7	77.8
QP-0.28-1	7.5	0.92	31.1	61.4
QP-0.28-2	23.8	1	15.3	60.9

Finally, Table 4-9 summarizes the mechanical properties measured on the studied steel grades. The results can be generalized as follows. The reported 0.2 % proof stress ($\sigma_{0.2}$) values are superior to 1000 MPa in all samples. The highest $\sigma_{0.2}$ value is obtained for the QP-0.28-1 sample, where also the highest σ_{UTS} is reached (Table 4-9). Nevertheless, this occurs to the detriment of both uniform elongation (ε_u) and elongation to failure (ε_f), which are almost 50% inferior compared to those of the QP-0.25-5 and the QP-0.28-2 samples. All these factors result in a different strain hardening behavior in all samples.

Table 4-9. Mechanical properties measured on the studied Q&P steel grades ($\sigma_{0.2}$, σ_{UTS}, ε_u, ε_f, n).

Specimen	$\sigma_{0.2}$ (MPa)	σ_{UTS} (MPa)	ε_u (%)	ε_f (%)	n
QP-0.25-5	1119	1341	9.5	12.9	0.12
QP-0.28-1	1207	1943	4.9	8.1	0.22
QP-0.28-2	1034	1425	9.6	15.8	0.17

4.3.2. Three-dimensional models of fracture surfaces for analysis of fracture behavior

SEM images of fracture surfaces of the broken Q&P steel specimens are illustrated in Figure 4-15 a, b and c. It is seen that all three conditions show a combination of quasi-cleavage mode with ductile fracture one. For the quasi-cleavage facets, fracture propagates along transgranular paths producing fracture surfaces similar to those caused by pure metallic cleavage. This feature of quasi-cleavage is indicated by a white

arrow in Figure 4-15 (a). In this case, fracture is usually preceded by formation of numerous small imbedded microcracks in the material ahead of the macroscopic crack, and the coalescence of some microcracks with the main macroscopic propagating crack [104].

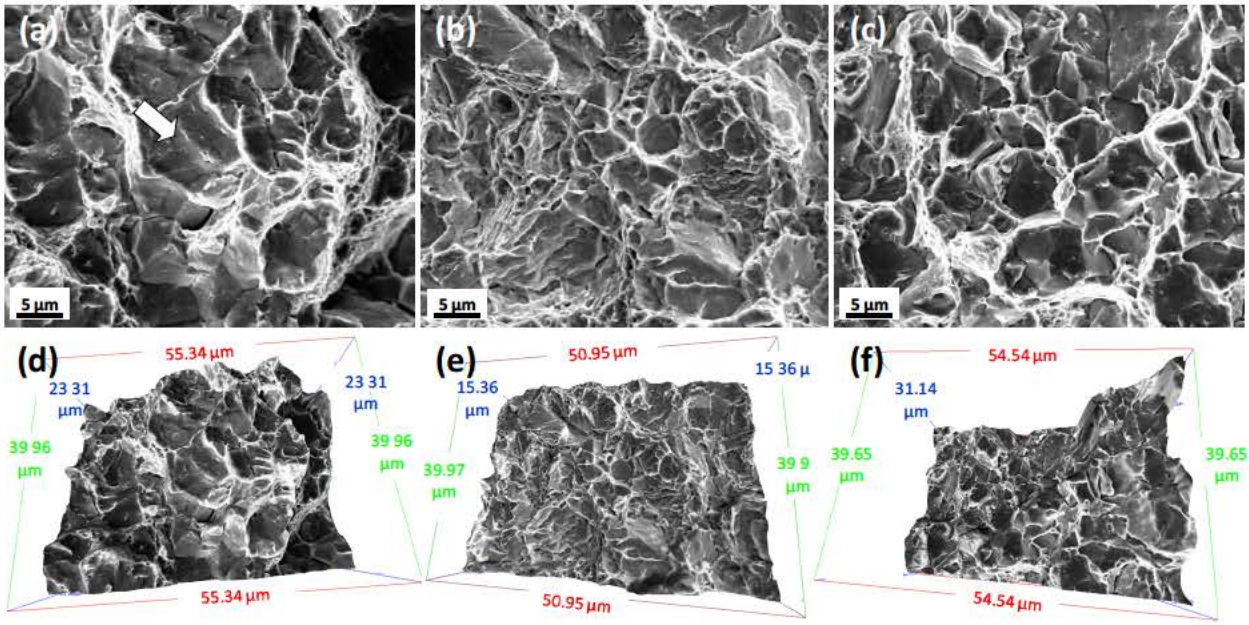

Figure 4-15. Fracture surface of (a) the QP-0.25-5 sample, (b) the QP-0.28-1 sample and (c) the QP-0.28-5 sample. Corresponding DEMs for: (d) the QP-0.25-5 sample, (e) the QP-0.28-1 sample and (f) the QP-0.28-2 sample.

It can be hypothesized that after transformation from austenite to martensite, the structural state of the parent phase is reflected to some degree in the resulting fracture surface. In particular, the block and packet sizes might be directly related to the size of parent austenite grains [205]. Cracks could propagate through the prior austenite grain boundaries, and the smooth fracture facets show no evidence of plastic deformation (marked by white arrow on Figure 4-15 a) [104, 205]. On the other hand, the ductile fracture surface mainly consists of dimples of varying size resulting from the growth of neighboring (micro)voids until the material between them necks down and ruptures. Microvoids can grow from various internal free surfaces. Under increasing stress conditions, the free surfaces grow into spherical voids and, at some stage, coalesce to form a local increment of fracture [104]. Some of the coarse dimples on the surface are surrounded by very fine dimples formed during coalescence of the larger ones (Figure 4-16 a and b). Nevertheless, the area fraction of the small dimples is much lower compared to that of the large dimples.

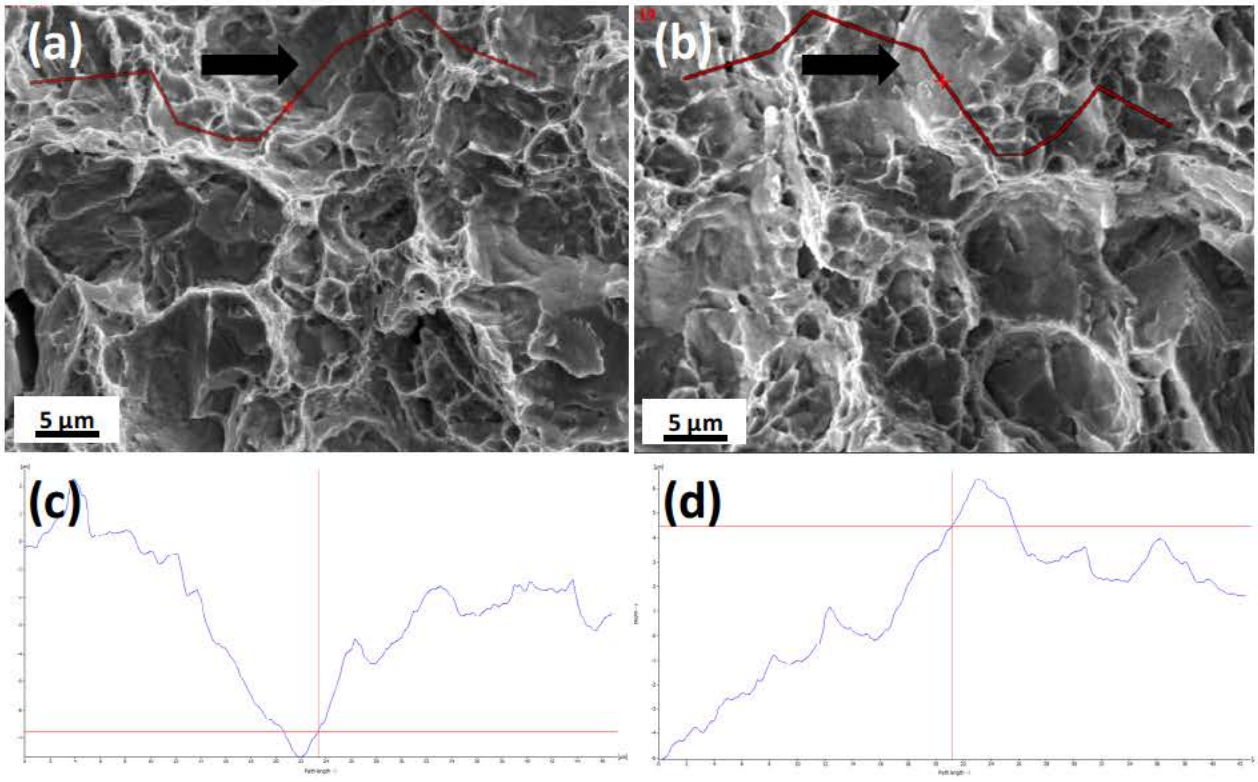

Figure 4-16. (a and b) SEM images of corresponding regions on both specimen halves of the QP-0.25-2 sample; corresponding profiles (c) through the fracture surface element in (a) and (d) the fracture surface element in (b).

As previously mentioned in Section 4.1.1, it is well known that in Q&P steels RA presenting film-like or interlath lamellar morphologies have better transformation stability compared with a blocky type [15, 16, 77, 78], which is 'consumed' during the early stage of plastic deformation [20]. In order for cleavage to initiate, there must be a local discontinuity, i.e. sharp microcrack, ahead of the macroscopic crack that is sufficient to exceed the bond strength. In the case of the analyzed multiphase Q&P steel grades, this discontinuity may be originated by the rupture of either UM island formed during Q&P cycle, or UM formed by phase transformation of RA due to applied stress. Then, the crack can propagate through the neighboring TM grains in a brittle manner. The preferable cleavage planes in this fracture mode are those with the lowest packing density, since fewer bonds must be broken and the spacing between planes is greater. In the case of the body-centered cubic (BCC) materials, cleavage typically occurs on (100) planes. The propagating crack changes direction each time it crosses a grain boundary; the crack seeks the most favorably oriented cleavage plane in each grain. Cleavage is most likely when the plastic flow is restricted [102]. However, as it can be seen in Figure 4-15 and Figure 4-16 a and b, quasi-cleavage fracture is combined with ductile fracture. In this case, voids form around

second-phase particles when sufficient stress is applied to the interfacial bonds. Once voids form, further plastic strain and hydrostatic stresses cause the voids to grow and eventually coalesce [102].

Figure 4-15 d, e and f illustrates representative DEMs of the corresponding fracture surfaces in Figure 4-15 a, b and c, for samples QP-0.25-5, QP-0.28-1 and QP-0.28-2, respectively. Their qualitative analysis gives the first impression that the fracture surfaces of all three conditions are very similar, despite they have different chemical compositions and Q&P treatments. Therefore, further quantitative analysis was performed in order to accurately measure fracture surface features, such as dimple size, as well as to reconstruct the fracture process. Results of this analysis and their discussion are presented in the following sections.

4.3.2.1. Dimple size and energy required to form dimple structure of fracture surface

DEMS can be utilized for the estimation of the dimple depth, h_o. The DEMs from corresponding fracture surface regions on both parts of a broken specimen must be generated for reconstruction of the local fracture process [178]. Figure 4-16 depicts the SEM images from the corresponding fracture surface areas on both halves of the same broken specimen for the QP-0.25-5 sample. The procedure for the determination of the h_o-values is the following. The left hand profile in Figure 4-16c corresponds to the image on Figure 4-16a and the profile in Figure 4-16d corresponds to the second half of the broken sample (Figure 4-16b). In Figure 4-17 a and b, these two profiles are arranged so they reproduce two stages of the fracture process.

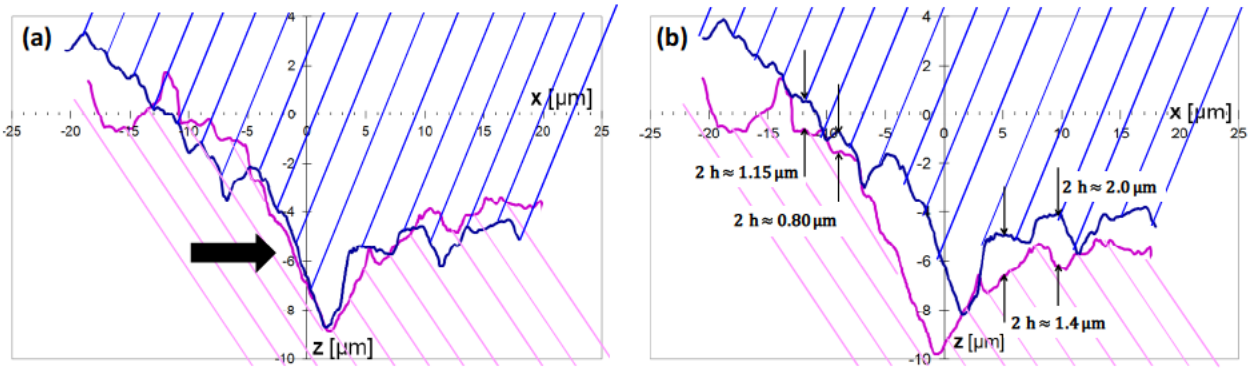

Figure 4-17. Profiles through the corresponding fracture surface element of Figure 4-16 at the (a) beginning of local failure and (b) moment of local failure.

Figure 4-17a illustrates the beginning of local failure, where quasi-cleavage of the UM phase occurs (marked by black arrows on Figure 4-16 a,b and Figure 4-17a). Figure

4-17b illustrates the moment of local failure, where fine voids coalesce with each other and with the large void formed due to quasi-cleavage of UM. The height of each dimple, h_o, can be easily estimated from the profiles as a half of void height (Figure 4-17b). At least 20 dimples were analyzed for each material condition and the obtained values of average dimple height are listed in Table 4-10.

The specific plastic strain energy required to form the micro-ductile structure per the unit area, R_{surf} which is depicted in Figure 4-18, can be estimated according to the Stüwe model [206] as:

$$R_{surf} = 2S\bar{\sigma}h_o \qquad \text{(Eq. 4-7)}$$

Where $S = 0.25$ and $\bar{\sigma}$ designates an appropriate flow stress of the material, determined as [207]:

$$\bar{\sigma} = \sigma_{UTS}\frac{\exp(n)}{(1+n)n^n} \qquad \text{(Eq. 4-8)}$$

Data on dimple depth and R_{surf} -values are given on Table 4-10.

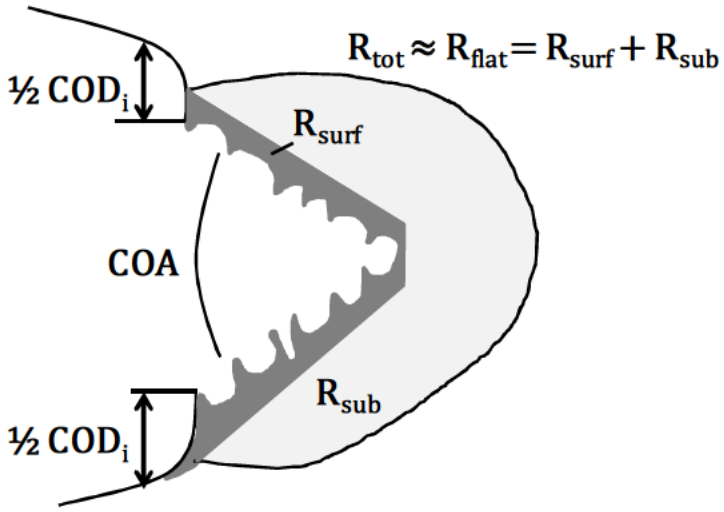

Figure 4-18. A schematic view of the direct approach to separate fracture energies. Redrawn from [178].

The largest dimples are observed in the QP-0.25-5 sample, that also corresponds to the Q&P steel grade with the largest TM grain size (Table 4-7) and the highest fraction of TM (Table 4-8). The energy required for the formation of dimple structure of surface R_{surf} is very low in all specimens and ranges between 0.22 and

0.53 kJ/m^2 (Table 4-10). For example, a value of 20 kJ/m^2 was reported for a maraging steel in [178], where dimples had a height of 200-300 µm. No any correlation between volume fraction of RA (Table 4-8) and the R_{surf} - values is observed. These observations can be rationalized based on high fraction of interphase and grain boundaries in the multiphase Q&P steels along with small size of microconstituents and significant stress partitioning in the microstructure [20, 162], which promote void formation at interphase boundaries, acting as potential sites for void nucleation [102]. This results in much lower size of dimples compared to that observed in other steels [178]. Indeed, the largest dimples found in the sample QP-0.25-5 having largest TM grains (Table 4-7) and highest volume fraction of TM (Table 4-8) speak in favor of this hypothesis.

Table 4-10. The depth of dimples and the plastic strain energy to form a unit area of the dimple structure on the fracture surface (R_{surf}).

Specimen	Dimples depth (h_0) (µm)	R_{suf} (kJ/m^2)
QP-0.25-5	0.61	0.53
QP-0.28-1	0.16	0.22
QP-0.28-2	0.29	0.28

4.3.2.2. Local and global fracture toughness

In this section, the procedure to determine the local crack tip opening displacement at the moment of fracture initiation is shortly described. The SEM micrographs in Figure 4-19 show corresponding regions in the midsection of both halves of the broken DENT QP-0.25-5 sample.

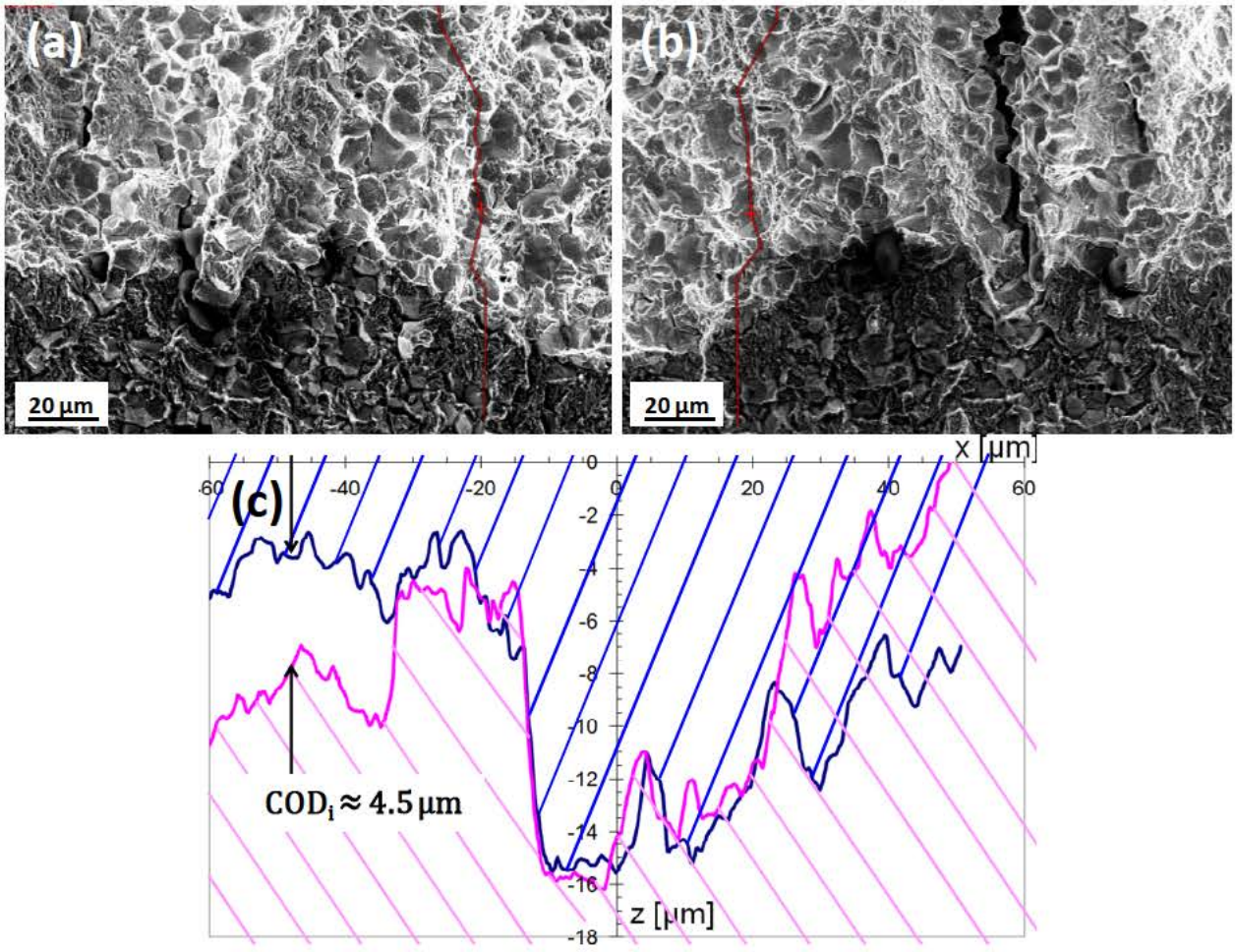

Figure 4-19. (a and b) SEM images of corresponding midsection regions on both specimen halves of the QP-0.25-5 sample tested at room temperature; (c) profiles at the moment of fracture initiation in the PT-400 sample at room temperature $COD_i^{local} = 4.5$ µm.

The fatigue regions (the dark regions at the bottom of the images) and the regions of micro-ductile fracture (at the top of the images) can be clearly identified. On the DEMs of these corresponding regions, crack profiles are extracted perpendicular to the fatigue crack front. Two corresponding profile paths are indicated in red color in Figure 4-19 a and b. In Figure 4-19 c, they are arranged so, that the moment of fracture initiation is depicted, i.e. the moment when the ligament between the first void in front of the tip and the blunted pre-crack fails. The upper profile (blue line) corresponds to Figure 4-19 a, whereas the lower profile (pink line) corresponds to Figure 4-19 b (Figure 4-19 c). From the profiles, the values of the local fracture initiation toughness COD_i^{local} can be determined at various positions along the crack front as shown in Figure 4-19 c, $COD_i^{local} = 4.5\ \mu m$. For each condition, at least 20 measurements were performed along the crack front in the midsection of the broken DENT specimens, where plane strain deformation prevails. Their average value for a given specimen is denoted as COD_i and it is a measure of the global fracture

toughness at the moment of fracture initiation. The COD_i-values are summarized in Table 4-11. Values of 4 ± 0.7, 2.8 ± 0.6 µm and 4.1 ± 1.5 µm are obtained for the QP-0.25-5, QP-0.28-1 and QP-0.28-2 samples, respectively. It can be seen that the average values of local fracture initiation toughness, COD_i, are not greatly affected by microstructure.

Table 4-11. The results of fracture surface analysis and estimation of fracture toughness and crack growth resistance.

Specimen	K_Q (MPa·m$^{1/2}$)	COD_i - δ_t (µm)	J_i (kJ/m^2)	$COD_{0.2}$ - $\delta_{0.2}$ (µm)	$J_{0.2}$ (kJ/m^2)	CTOA (°)	R_{tot} (kJ/m^2)
QP-0.25-5	148.8 ± 5.9	4 ± 0.7	8.7	15.7 ± 0.7	34.1	3.7	92.3
QP-0.28-1	73.2 ± 0.1	2.8 ± 0.6	9.3	9.3 ± 0.8	31.3	1	49.7
QP-0.28-2	117.2 ± 9.0	4.1 ± 1.5	10.1	22 ± 3.1	54.2	3	124.1

The COD_i^{local} -values can be subsequently transformed to J_i^{local}-values, using the well-known relationship between the J-integral and COD [169] :

$$J = \frac{1}{d_n}\sigma_y COD \qquad \text{(Eq. 4-9)}$$

The parameter d_n in (Eq. 4-9) is a dimensionless constant that depends on the strain hardening coefficient $n = 1/N$, and on the reference strain, $\varepsilon_o = \sigma_y/E$. The average J_i-values are also listed in Table 4-11.

An analogous procedure to that described above for the COD_i-values calculation was used in order to estimate the $COD_{0.2}$-values. In this case, the profiles are arranged so that the crack propagation, Δa, is 0.2 mm from the fatigue pre-crack front, as depicted in Figure 4-20. The results from the $COD_{0.2}$ calculation (Table 4-11) show the same tendency to those obtained for the COD_i estimation. However, the difference between $COD_{0.2}$ for the QP-0.28-2 and QP-0.25-5 samples is larger.

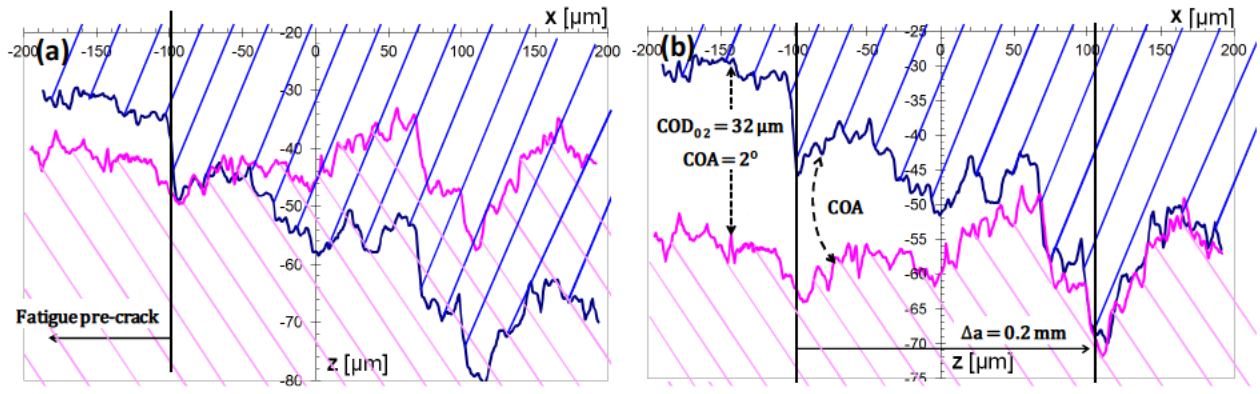

Figure 4-20. Profiles from the DEM of fracture surface showing the moment of (a) start of crack growth and (b) crack propagated to 0.2 mm.

It is seen that a slight increment of both COD_i and $COD_{0.2}$ is observed when the fraction of RA is enhanced. However, their scatter (i.e. standard deviation) (Table 4-11) tends to increase with increasing volume fraction of RA (Table 4-8). This can be explained in Figure 4-21, where an OIM phase map superimposed with image quality of the QP-0.28-2 sample can be seen. The local resistance against local fracture initiation can vary depending on which microconstituent (TM, Um or RA) is faced by a fatigue pre-crack, its size and crystallographic orientation. In addition, Gerberich *et al.* [208] and Antolovich *et al.* [108] suggested that fracture toughness could be enhanced through the TRIP effect. As previously stated in Section 4.1.1, many factors influence the transformation stability of austenite [77, 84, 87-89, 92]. In the present case, carbon content, grain size and the surrounding phases of RA (fractions of TM and UM) are very similar, so RA grains with different morphologies [15, 16, 77, 78] should behave differently in front of the crack. This was confirmed in the work by Wu *et al.* [105], where it was stated that toughness of Q&P-treated sheet steels is determined to a certain extent by the stability of RA.

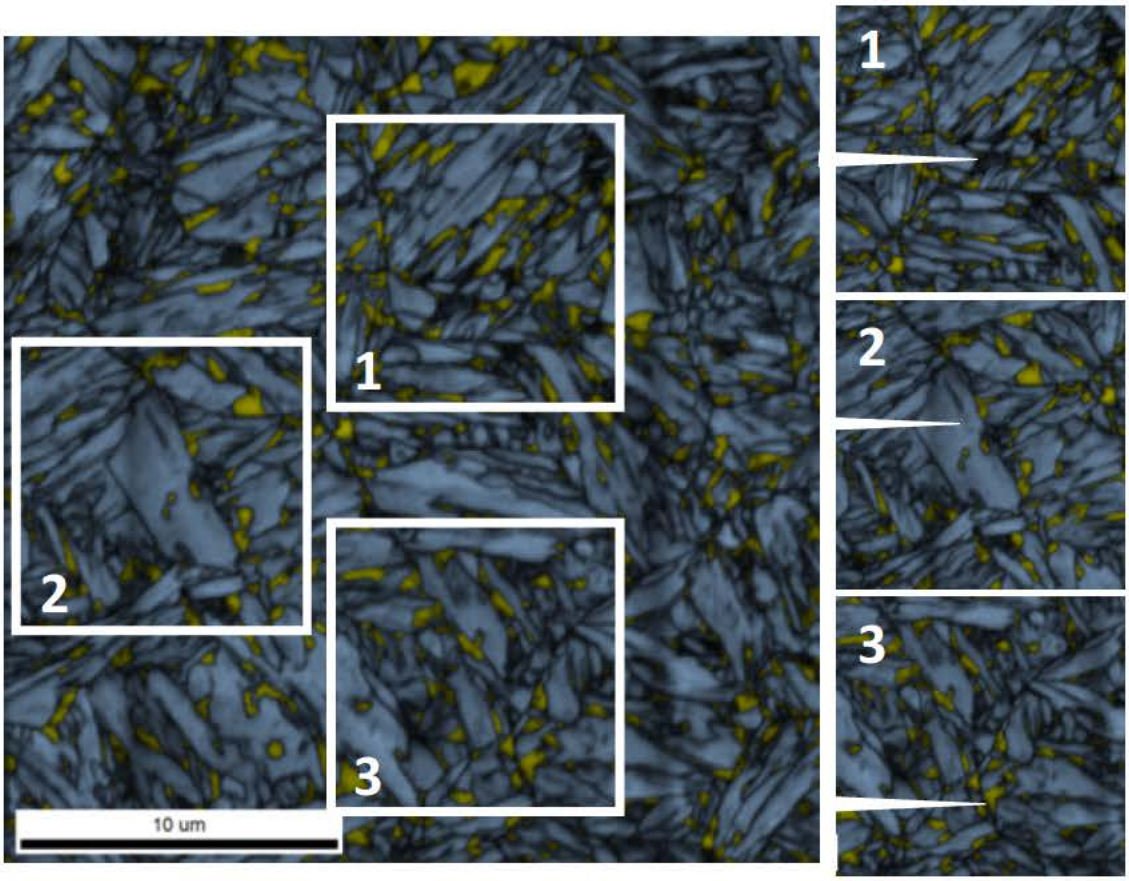

Figure 4-21. OIM maps of the QP-0.28- sample, illustrating the microstructural heterogeneity which leads to a high scatter in the resistance against crack propagation. Close-up views of the areas within the rectangles shown in 1, 2 and 3.

4.3.2.3. Crack growth resistance

The total crack growth resistance, R_{tot}, of a material can be defined as total non-reversible energy which is required to extend the crack area by an increment [178]. As the local fracture initiation toughness can be measured in terms of the critical $CTOD$, the local crack growth resistance can be measured in terms of the crack opening angle, COA. The COA can be easily measured from the profiles generated using DEMs. Eight COA-values were estimated for the crack extension at the onset of crack propagation ($\Delta a = 0.2\,mm$). An example is shown in Figure 4-20 for the QP-0.28-2 sample. The average COA-values are listed in Table 4-11. Then, the R_{tot}-values can be calculated as [178, 209]:

$$R_{tot} = \frac{m\sigma_y b}{\eta} \cdot COA \qquad \text{(Eq. 4-10)}$$

where b is the ligament length, η the pre-factor in the formula to evaluate J, and m is estimated as:

$$m = \frac{\sigma_{UTS}}{\sigma_y} \cdot \frac{\exp(n)}{(1+n) \cdot n^n} \quad \text{(Eq. 4-11)}$$

The calculated R_{tot}-values for the crack extension at the beginning of crack propagation are presented in Table 4-11. It is seen that the total crack growth resistance tends to increase with increasing volume fraction of RA (Table 4-8). When the fraction of RA increases from 7.5 % to 11.5% (in samples QP-0.28-1 and QP-0.25-5, respectively), the R_{tot} -value is enhanced from 49.7 kJ/m^2 to 92.3 kJ/m^2. However, a slightly modest increment is observed when the RA fraction is further increased up to 23.8 % (QP-0.28-2), reaching a R_{tot}-value equal to 124.1 kJ/m^2.

As it was reported in Section 4.3.2.1, the energy required for formation of dimple structure of surface R_{surf} is very low in all specimens. Therefore, as R_{tot} (see Figure 4-18), results from the addition of R_{surf} and R_{sub}, only a small percent of the plastic energy spent, is used to form the fracture surfaces. The remaining part is spent in the deformation process below the surface. This energy is thus required to produce the global crack opening angle in the crack path [178].

4.3.3. **The principles of microstructural design in Q&P steels to improve their fracture properties**

Based on the results above, it can be concluded that fracture properties in Q&P steels can be tuned via intelligent microstructural design. A general recipe for improvement of fracture behavior of multiphase Q&P steel grades includes:

- Control of the volume fraction, size and morphology of RA. Enhanced RA volume fraction slightly improves fracture initiation toughness (COD_i) and can significantly improve the crack growth resistance (R_{tot}). Austenite - martensite phase transformation can be also controlled via factors determining stability of RA, such as their size, carbon content, crystallographic orientation, etc [162].
- Matrix conditions can play an important role in determining fracture behavior of Q&P steels. In particular, the specific plastic strain energy required to form the micro-ductile structure per the unit area R_{surf} was found to be dependent on the TM grain size and volume fraction. In addition, local discontinuities originating cleavage initiation may be generated by the rupture of either UM

island formed during Q&P cycle, or UM formed by phase transformation of RA due to applied stress.

4.3.4. Conclusions to Section 4.3

Fracture behavior of the Q&P steels was analyzed by fracture testing of DENT specimens and quantitative fracture surface analysis. The values of the local crack tip opening displacement, crack opening angle and dimple height were experimentally measured. The energy required for formation of fracture surface and total crack growth resistance were calculated. It is demonstrated that:

- Local fracture initiation toughness is slightly increased in the sample with the highest volume fraction of RA, whereas total crack growth resistance of Q&P steels is significantly improved with increasing volume fraction of RA due to the TRIP-effect delaying crack propagation.
- Matrix conditions (volume fraction of TM and UM) can play important role in fracture behavior of Q&P steels.
- Fracture properties of Q&P steels can be tuned via intelligent microstructural design, i.e. manipulation with volume fraction and morphology of RA and matrix conditions.

4.4. Fatigue behavior of Q&P steels

This work focuses on the effect of microstructure on high cycle fatigue of Q&P steels and its evolution during cyclic loading. For this purpose, due to the excellent compromise between tensile properties and fracture behavior, the QP-0.25-5 and QP-0.28-2 chemistries were analyzed.

It is demonstrated that increased content of RA improves fatigue limit of Q&P steels that is related to delay of crack propagation due to austenite-martensite phase transformation. Increasing stress amplitude promotes austenite-martensite phase transformation during cycling. It is shown that size and crystallographic orientation of RA are the main factors determining its stability, whereas its shape and spatial distribution do not seem to affect it significantly. Fatigue crack initiation during fatigue testing with high stress amplitudes occurs by inter-granular cracking, whereas transgranular cracking controls fatigue crack initiation during cycling loading with lower stress amplitudes. Transgranular crack propagation dominates in the second stage of fatigue at all stress amplitudes. The final stage of fatigue is also not affected by the stress amplitude. It is suggested that fatigue life of Q&P steels can be enhanced via improvement of strength of grain/interphase boundaries.

4.4.1. Microstructure of the Q&P processed steels before cyclic deformation

OIM phase maps with BCC phase (martensite) in blue and FCC phase (RA) in yellow superimposed with the gray scale band contrast of the studied samples are shown in Figure 4-22 and Figure 4-23 (top images).

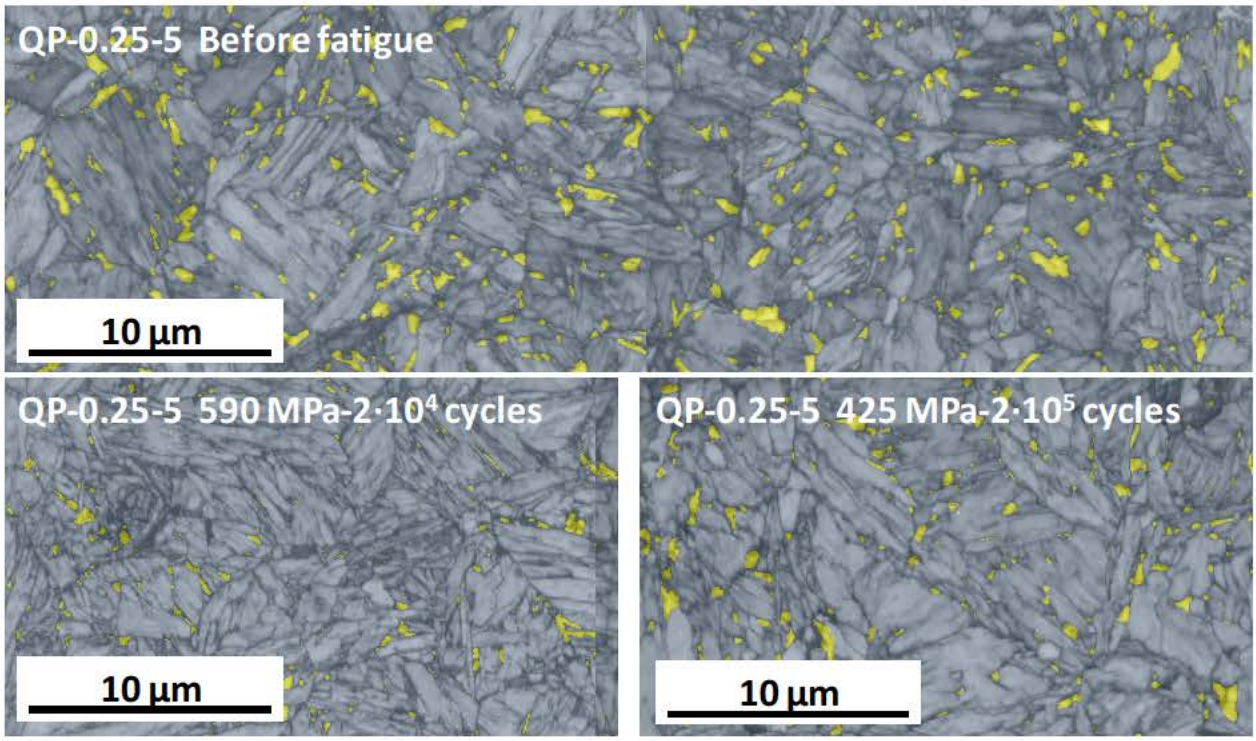

Figure 4-22. Combined gray scale band contrast and color coded phase map of the QP-0.25-5 steel grade before fatigue (top), after fatigue testing with the highest stress amplitude (bottom left) and after fatigue testing with the lowest stress amplitude (bottom right).

After both Q&P treatments, irregular-shaped blocks of TM constitute the major phase of the microstructure, whereas the others (i.e. UM and RA) are dispersed in the matrix (see Section 4.1.1). Due to a less perfect BCC lattice, UM regions formed during the last quench to room temperature can be identified as the darkest ones, which can be found in the vicinity of the yellow RA grains. The average grain diameter of the UM regions can be roughly estimated but could not be accurately measured from the available OIM maps, since lattice distortion leads to a low pattern quality and indexation of the UM zones in the OIM scans. Information for the size of the microconstituents (TM and RA) before fatigue testing is provided in Table 4-12.

Table 4-12. Average grain size (equivalent circle diameter) for the different microconstituents of the Q&P steel grades.

Specimen	Tempered martensite (TM) (µm)	Retained austenite (RA) (µm)
QP-0.25-5	3.1 ± 0.9	0.3 ± 0.2
QP-0.28-2	2.3 ± 0.7	0.3 ± 0.2

In the case of the TM microconstituent, a slightly higher value of the grain size of 3.1 ± 0.9 µm can be found for the QP-0.25-5 sample, compared to the QP-0.28-2 sample (2.3 ± 0.7 µm) (Table 4-12). Moreover, the RA average size is in the same range for the QP-0.25-5 and the QP-0.28-2 specimens (Table 4-12). In both cases, various RA morphologies are present in the microstructure (Figure 4-22 and Figure 4-23) film-like RA, lamellar RA and blocky RA [210]. The growth of interlath RA from film-like to a blocky type as a function of partitioning parameters has been reported in literature [21, 162, 210]. As explained in Section 4.1.1, the transformation stability of RA is affected by many factors, among other its morphology [77, 94]. The largest "blocky type" austenite grains usually show a relatively low mechanical stability during tensile testing [84, 98]. This morphology tends to transform to martensite under a small strain and contributes little to the TRIP effect [15, 16, 77, 78], as it is 'consumed' during the early stage of plastic deformation [20, 86]. On the contrary, the interlath-lamellar morphology shows intermediate stability and steadily transforms throughout the entire test, whereas the film-like RA has been reported to be the most resistant morphology against transformation [98].

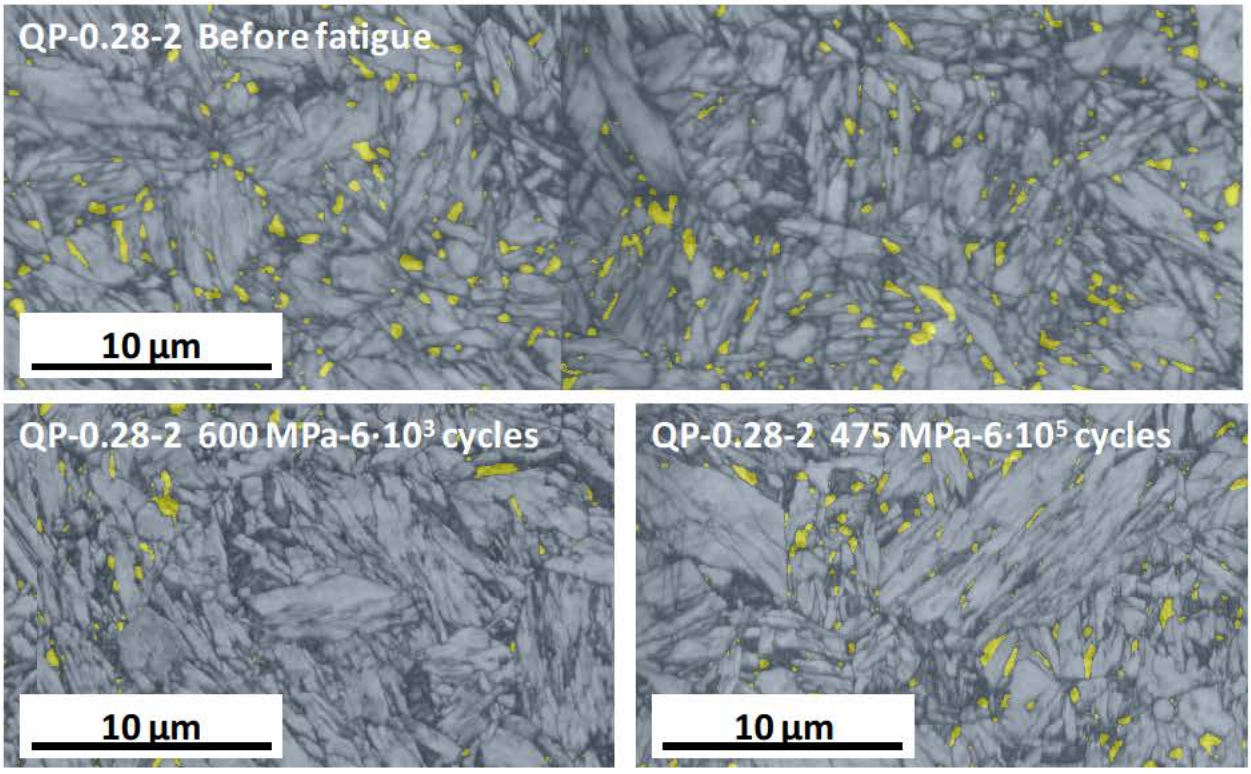

Figure 4-23. Combined gray scale band contrast and color coded phase map of the QP-0.28-2 steel grade before fatigue (top), after fatigue testing with the highest stress amplitude (bottom left) and after fatigue testing with the lowest stress amplitude (bottom right).

Table 4-13 lists the measurements of volume fraction and carbon content of RA, as well as the volume fraction of TM and UM which were determined by X-ray diffraction and by EBSD analysis.

Table 4-13. Volume fraction and carbon content (wt. %) of RA and volume fraction of UM and TM in the studied steel grades.

Specimen	Retained austenite (RA)		Untempered martensite (UM)	Tempered martensite (TM)
	(%)	% C (wt.)	(%)	(%)
QP-0.25-5	11.5	1.1	13.3	75.2
QP-0.28-2	23.8	1	16.0	60.2

Average volume fractions of RA 11.5 % and 23.8 %, along with carbon contents of 1.1 and 1 wt. % were measured by XRD in the QP-0.25-5 and the QP-0.28-2 samples, respectively (Table 4-13). The localized EBSD scans yield significantly lower RA fractions than XRD before fatigue testing, being 6.3 % and 4.0 % for the QP-0.25-5 and the QP-0.28-2 samples (Table 4-14), respectively.

Table 4-14. Fraction of RA (%) measured by EBSD before and after fatigue testing at the distance of 1 mm from the fracture surface.

Specimen	Before fatigue	High stress amplitude	Low stress amplitude
QP-0.25-5	6.3	2.2	4.0
QP-0.28-2	4.0	1.8	3.2

It should be noted that although the spatial resolution of the EBSD technique is reasonably high (step size is ≈ 55 nm), the smallest austenite laths formed between the martensite plates, as observed with TEM, have sizes in the range of 20–100 nm [21, 77, 210]. The smallest laths can therefore not be resolved by EBSD but are detectable with XRD. Similar observations have been reported for various Q&P steels in [21, 183, 210]. Therefore, it can be concluded that the fraction of smallest austenite laths (film-like type) which are not detected by EBSD, is higher in the QP-0.28-2 steel grade.

4.4.2. Tensile properties of Q&P steels

As it was already discussed in Section 4.3.1, the tensile properties measured on the studied steel grades are summarized in Table 4-9. The reported differences in mechanical behavior can be related to the microstructure of the Q&P processed steels. Both steel grades have similar grain size of TM and RA. However, much higher volume fraction of RA in the QP-0.28-2 steel (23.8 %) results in lower yield strength, higher strain hardening exponent and higher ultimate tensile strength of the material. In addition, in the QP-0.28-2 sample, ductility may be enhanced due to the contribution of the high volume fraction of film-like RA that is present in the microstructure [60, 109, 210].

4.4.3. Cyclic behavior of Q&P steels

Figure 4-24 shows the *S-N* curve for the QP-0.25-5 and QP-0.28-2 steel grades. At the higher stress amplitudes laying in the range of 500-600 MPa, experimental points for both Q&P steels are overlapping. The number of cycles, that the steels can endure before failure, tends to increase with decreasing stress amplitude. For the QP-0.28-2 steel, the *S-N* curve becomes horizontal at the stress amplitude of S = 445 MPa at $2 \cdot 10^6$ cycles, which can be referred to as the fatigue limit of the material [101]. However, the fatigue limit for the QP-0.25-5 steel could not be estimated, as all tested specimens broke achieving maximum number of cycles of $2 \cdot 10^5$ at the lowest stress amplitude of 425 MPa. Nevertheless, it is clear that the QP-0.28-2 steel grade shows higher fatigue limit compared to the other material (Figure 4-24).

It is well known that in the HCF regime, fatigue life is governed by crack nucleation [101]. Thus, materials with higher resistance against fatigue crack initiation have higher fatigue life. Obviously, the resistance of the material to crack nucleation is determined by its microstructure. In the next section, the effect of microstructure on fatigue behavior of the Q&P steels and evolution of microstructure during cycling is analyzed.

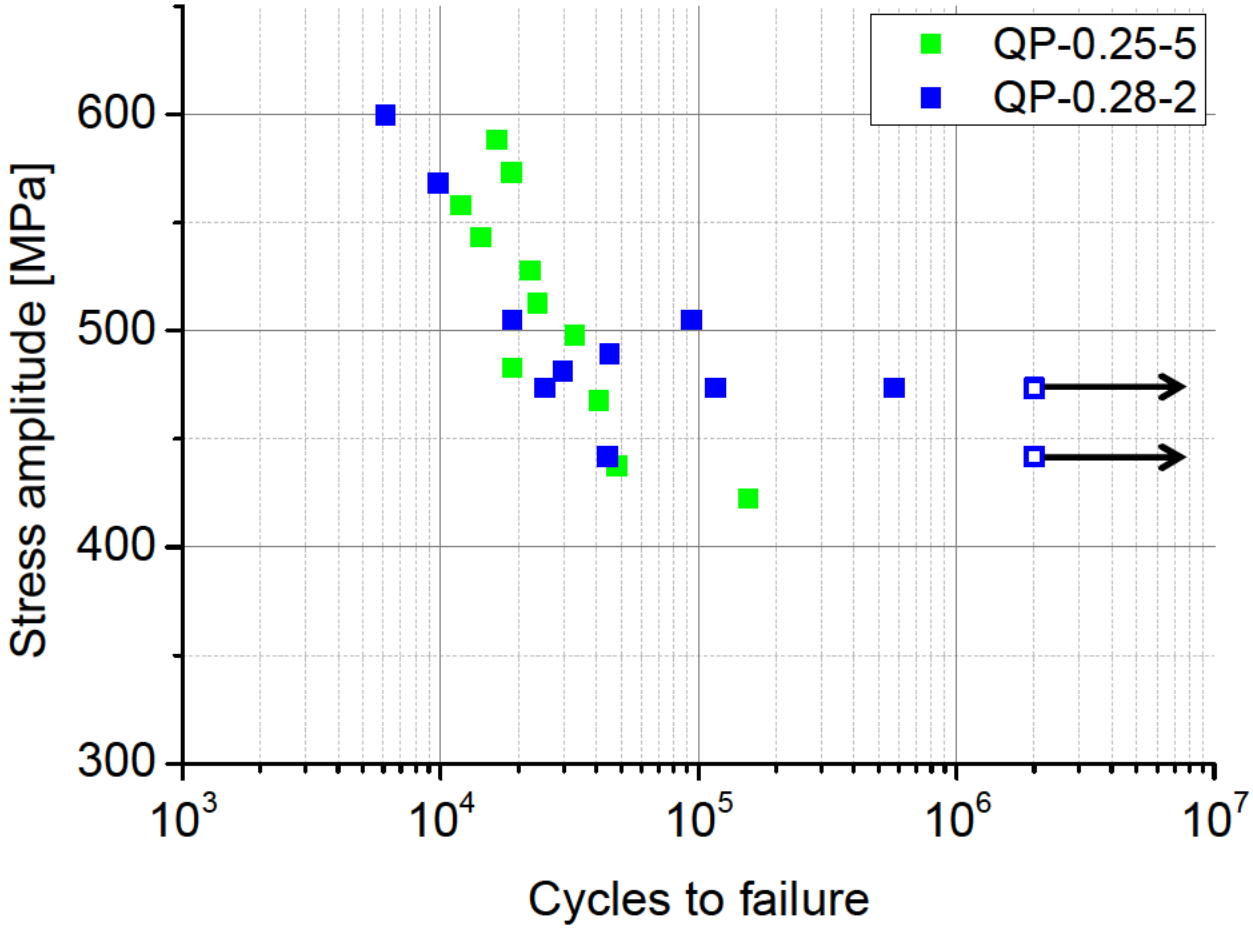

Figure 4-24. QP-0.25-5 and QP-0.28-2 steel grades *S-N* curves comparative.

4.4.4. Evolution of microstructure in the Q&P steels during fatigue testing

4.4.4.1. Effect of cyclic deformation on phase composition of the Q&P steels

In order to study the effect of cyclic deformation on microstructure and the role of RA in cyclic behavior, the microstructure of samples from both steel grades after fatigue testing with the highest stress amplitude (i.e. the lowest number of cycles before failure) and with the lowest stress amplitude (i.e. with the highest number of cycles before failure) was carefully analyzed. The OIM scans were taken from areas located at 1 mm distance from the fracture surface of the broken specimens: thus, the measurements were performed inside the homogenously cyclically deformed zone, i.e., in the gauge length area, which was not affected by microscopic plastic deformation in front of the propagating crack. The bottom left images in Figure 4-22 and Figure 4-23 correspond to the QP-0.25-5 and QP-0.28-2 steels after fatigue testing with the highest stress amplitude, whereas the bottom right images in Figure 4-22 and Figure 4-23 correspond to the specimens after fatigue testing with the lowest stress amplitude. The RA fraction was also measured by EBSD after fatigue

testing and the results are listed in Table 4-14. Partial RA transformation takes place during cyclic loading, as can be seen in Table 4-14. In addition, for both chemistries, the RA fraction measured in the specimen after fatigue testing with the highest stress amplitude is inferior to that measured in the specimen with the lowest stress amplitude (Table 4-14). This agrees well with the results previously reported for TRIP steels in [121], where higher applied stresses resulted in higher volume transformation of RA, due to the higher contribution of mechanical driving force to the total driving force for martensitic transformation, and to the higher damage accumulation in the form of cyclic plasticity [211]. Despite the fact that in both cases the maximum stresses reached during cyclic testing are well below the 0.2 % proof stress value measured for the Q&P steel (Table 4-9), the local stress reached in the RA microconstituent should be superior to its 0.2 % proof stress due to significant stress and strain partitioning in the Q&P steels [162]. Recent electron microscopy studies have also shown that transformation of RA to martensite is triggered ahead of the fatigue crack tip, leading to a delay in fatigue crack growth [212]. This was indirectly confirmed in the present study, where the Q&P steel with the higher volume fraction of RA shows higher fatigue life at lower stress amplitudes.

The evolution of the RA grain size and RA aspect ratio during cyclic loading at both fatigue regimes and for both chemistries was also studied (Figure 4-25).

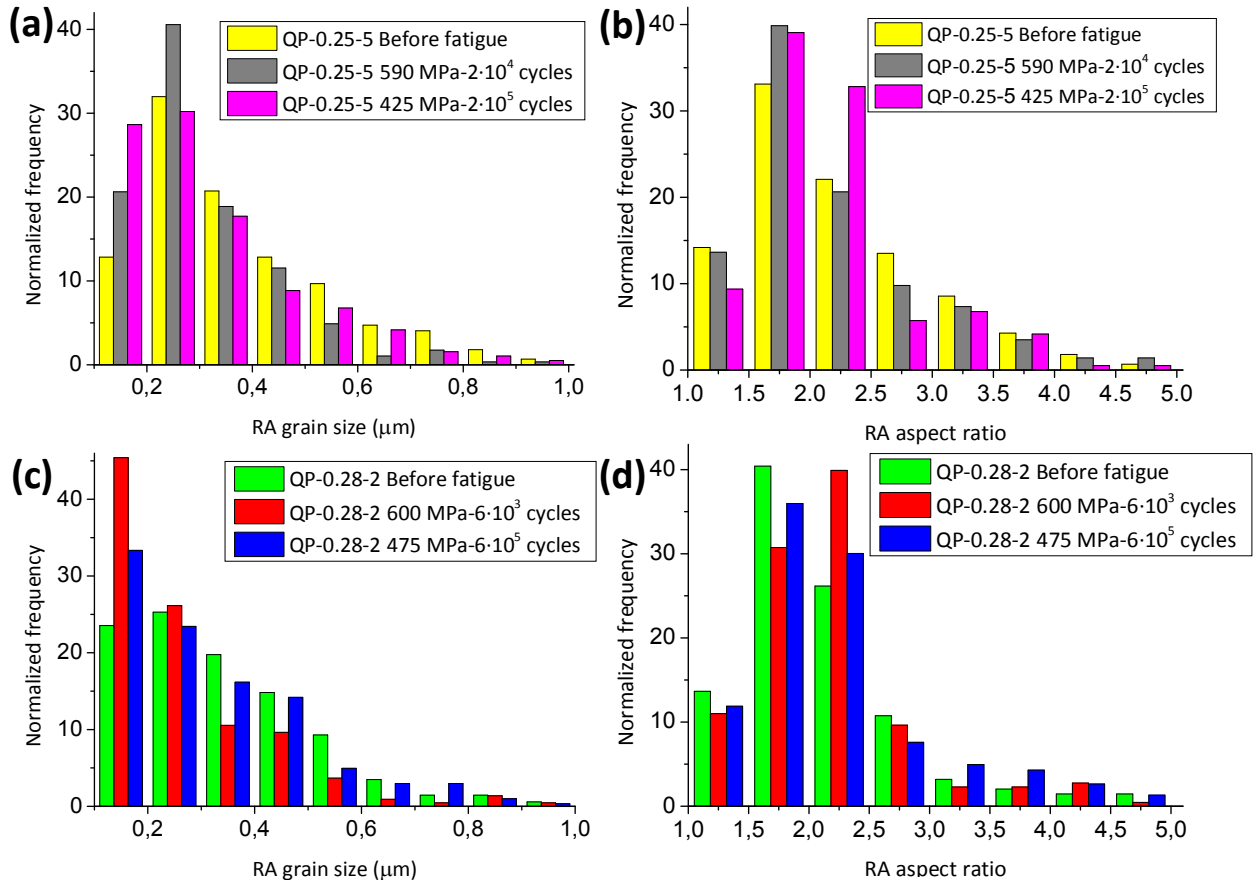

Figure 4-25. Histograms of RA grain size (a,c) and RA aspect ratio distribution (b,d) in the QP-0.25-5 (a,b) and the QP-0.28-2 (c,d) samples before and after fatigue testing.

For both compositions, the RA grain size distribution before fatigue testing is broader (Figure 4-25 a and c) and it becomes narrower with fatigue testing, surrounding a peak located at 0.2 μm. This means that the smallest RA grains were more stable against cyclic deformation [162] and/or that some coarse RA grains were partially transformed [77] and reduced their size. This tendency is more evident in the case of the samples tested with the highest stress amplitude, as the RA transformation is enhanced by the higher applied stresses. On the contrary, no clear conclusions can be drawn from the RA aspect ratio histograms in Figure 4-25 b and d. Therefore, it can be concluded that neither the shape of RA nor its spatial distribution can significantly affect stability of RA during cyclic loading.

4.4.4.2. Effect of crystallographic orientation of RA on its stability during cycling

The effect of crystallographic orientation of RA on its stability in cyclic loading was studied in this work. As an example, the ODFs in ϕ_2 = 0°, 45° and 65° sections of Euler space for RA in the QP-28-2 sample before and after fatigue testing [95, 210] are presented in Figure 4-26.

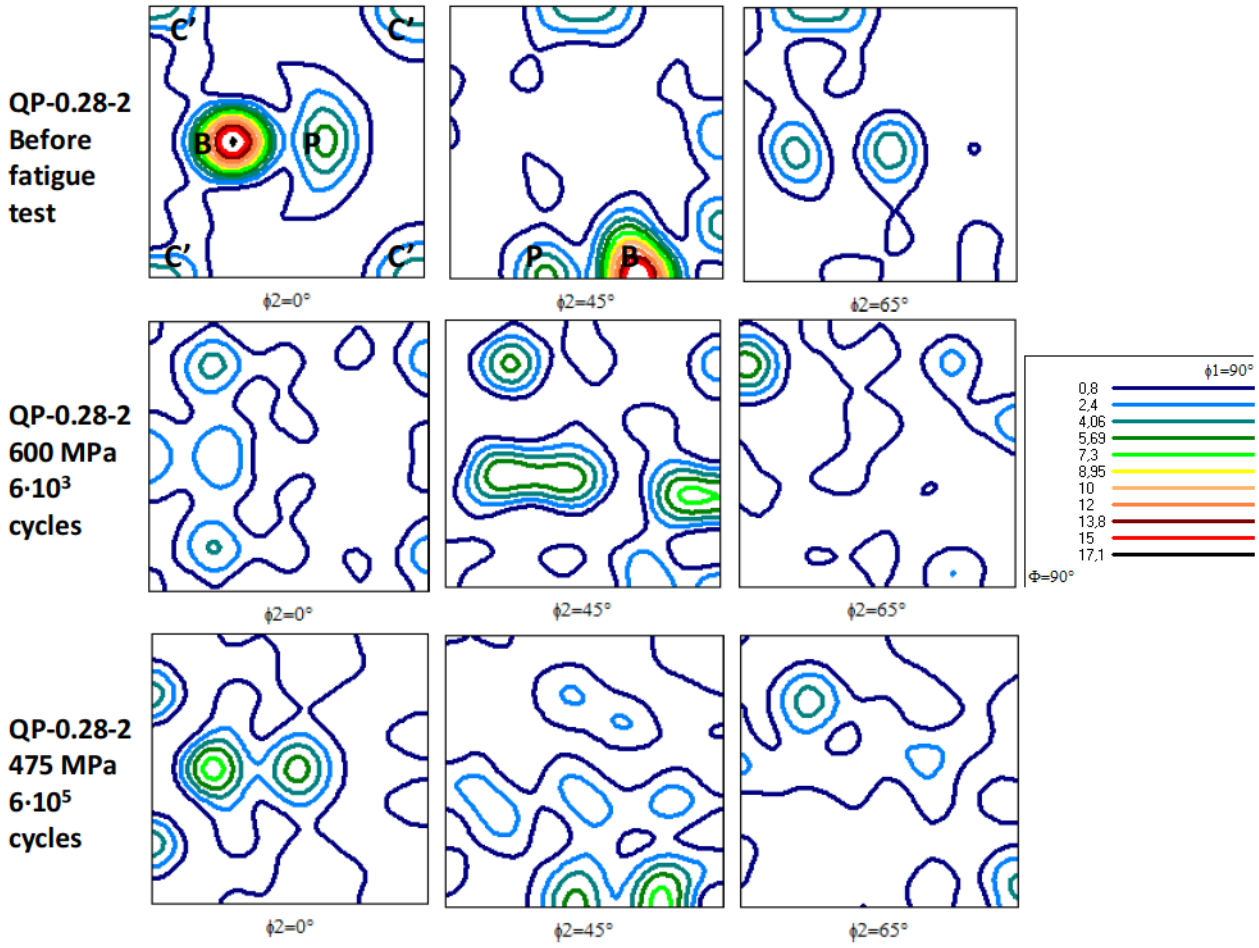

Figure 4-26. Orientation distribution functions (ODFs) in ϕ_2 = 0°, 45° and 65° sections for retained austenite in sample QP-0.28 before and after fatigue testing.

All the important orientations typical for rolled and annealed FCC materials can be found in these sections. The series expansion method (with L_{max} = 16) was employed for representing each ODF. It should be noted that identical color scales are used for all conditions (Figure 4-26). In the material before fatigue testing, orientations with highest intensities are located in the vicinity of the Brass B {011} <112>, P {011} <111> and Cube C' {001} <110> components (see Figure 4-26). In the specimen after fatigue testing with the lowest stress amplitude, the textures of RA are rather weak compared to those of the undeformed material. In addition, the weak Cube texture should have fully undergone the transformation to martensite, as it does not appear in the corresponding ODFs. Moreover, the Brass and P components seem to weaken their intensity. Similar observations can be also reported for the specimen after fatigue testing with the highest stress amplitude. The behavior of the Brass component is analogous and even more pronounced for this testing regime, as it weakens its intensity and/or rotates at the expense of other random components. In this case, both the Cube and P texture should have fully undergone the

transformation to austenite, due to the localized plastic deformation enhanced by the microstructural heterogeneity of the Q&P steel grade. As it was already discussed above, some plastic deformation can be induced during fatigue testing with the highest stress amplitudes into the RA microconstituent, as local stresses might reach and even exceed the RA yield stress [10, 11, 71, 117, 162]. It should be noted that these observations are in a very good accordance with those reported by De Knijf *et al.* [95], who investigated the transformation rate of RA orientations during interrupted tensile testing of a Q&P steel. Their results on the distribution of the mechanical driving force for the martensitic transformation of RA are summarized in Figure 4-27.

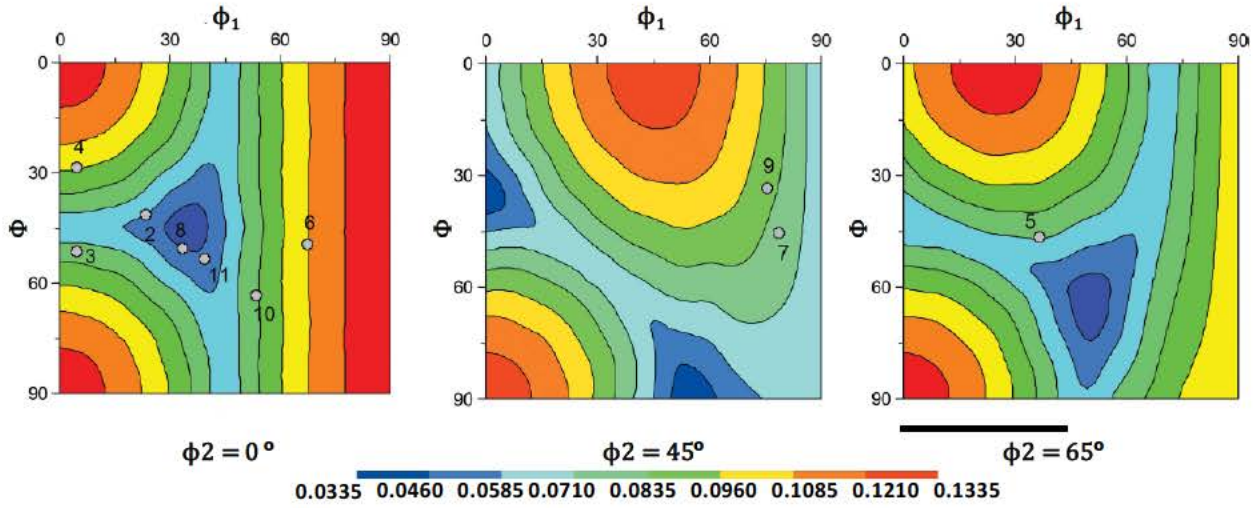

Figure 4-27. The distribution of the mechanical driving force for the martensitic transformation in orientation space, ϕ_2 = 0°, 45° and 65°. Low values of the modeled mechanical driving force correspond to low transformation potentials [95].

According to [95], the cube orientation, which is frequently present in textures of FCC materials after conventional rolling and recrystallization annealing, shows the highest martensitic transformation potential. In contrast, typical FCC rolling components, such as the Brass component, are less likely to undergo martensitic transformation than the recrystallization texture components and thus present lower transformation potential. On the other hand, the P component shows an intermediate transformation potential between the Cube and Brass components (Figure 4-27). Therefore, the orientations with the highest transformation potentials transform first and the orientations with lower transformation potentials will transform later or will remain stable (if other parameters such as RA grain size, carbon concentration and morphology are not taken into account) [95, 210].

It should be noted that Q&P processing leads to formation of a very complex multiphase microstructure, where there are numerous other factors affecting transformation stability of RA, such as the carbon concentration in the RA grains [84, 87], the constraining effect of the surrounding phases [92], etc. The stability of a given RA grain is always determined by interplay of all those factors, and it is an extremely complicated task to determine the contribution of each individual factor [86].

4.4.5. **Fatigue fractography analysis and mechanisms of fatigue crack initiation and propagation**

As it is described in Section 1.6, fatigue failure proceeds in three distinct stages. These three areas are depicted on the fatigue fracture surface for the QP-0.28-2 grade tested at the highest stress amplitude (Figure 4-28). The SEM image of the overall fracture surface is shown in the top left image, along with indication of the location of the stages I, II and III. Figure 4-28 (I) illustrates the inter-granular cracking mechanism which was responsible for fatigue crack initiation on the specimen surface. The size of the fatigue crack initiation area is ≈ 25 μm. Transgranular crack propagation mechanisms dominate in the second stage, though some small areas of intragranular crack propagation are also observed (Figure 4-28 (II)). Roughly, the surface formed by intragranular cracking is estimated at ≈ 10 %. Finally the ultimate ductile failure surface (Figure 4-28 (III)) consists of dimples resulting from the growth of small neighboring voids until the material between them necks down and ruptures [104]. Size of dimples is in the range of 1-10 μm. The large dimples are surrounded by smaller ones formed during coalescence of larger voids.

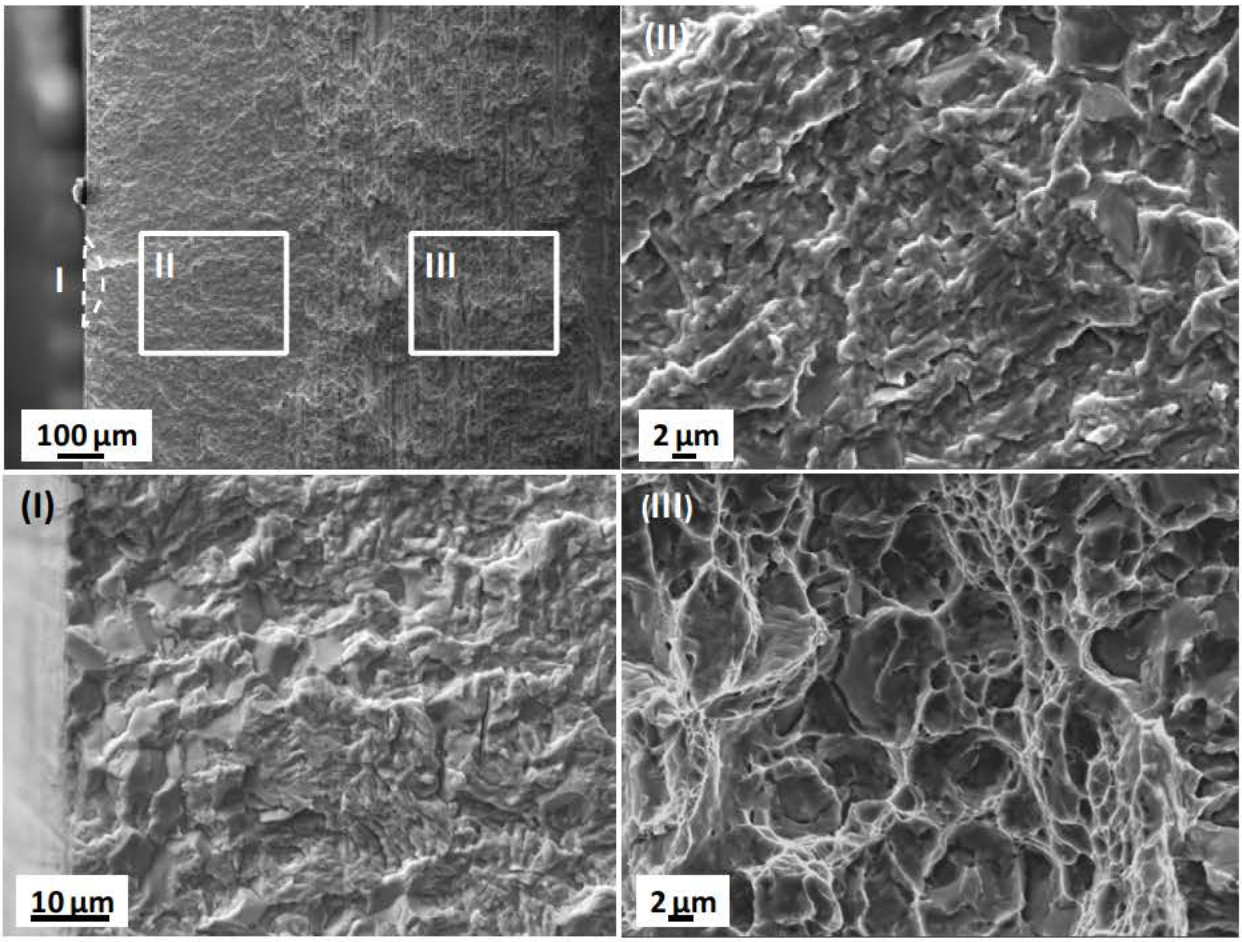

Figure 4-28. Fatigue fracture surface of the QP-0.28-2 grade formed after fatigue testing with high stress amplitude (600 MPa and $6 \cdot 10^3$ cycles). I stands for fatigue crack initiation area, II for fatigue crack propagation area and III for the last stage of fracture.

Similar fatigue fracture surface was observed in the QP-0.25-5 grade tested under similar conditions. In addition, some evidence of quasi-cleavage is also seen, that could take place in the UM microconstituent having the lowest ductility in the microstructure.

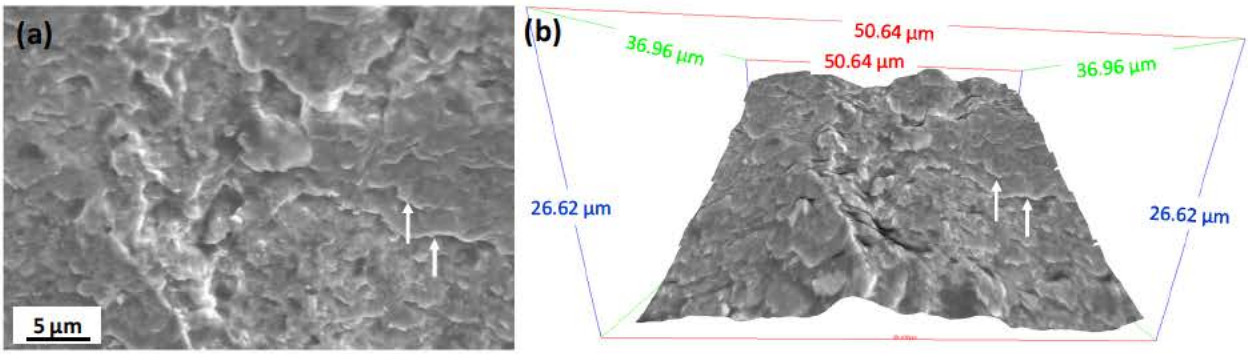

Figure 4-29. Fatigue fracture surface of the QP-0.28-2 grade formed in the fatigue crack initiation area after testing with low stress amplitude (425 MPa and $2 \cdot 10^5$ cycles). SEM image (a) and stereo image (b). Striations are marked by white arrows.

Analysis of fatigue fracture surfaces in the Q&P steels tested with the lowest stress amplitude showed that transgranular cracking was the fatigue crack initiation mechanism in both steel grades (Figure 4-29). Again this mechanism was dominant during stable crack propagation. Striations were not regularly observed on the fatigue fracture surface (Figure 4-29). Well developed dimple structures were observed for the final stage for the both steel grades. There was no any effect of the stress amplitude on the morphology of fracture surface formed at the final stage of fatigue testing, as demonstrated for the QP-0.28-2 chemistry in Figure 4-30.

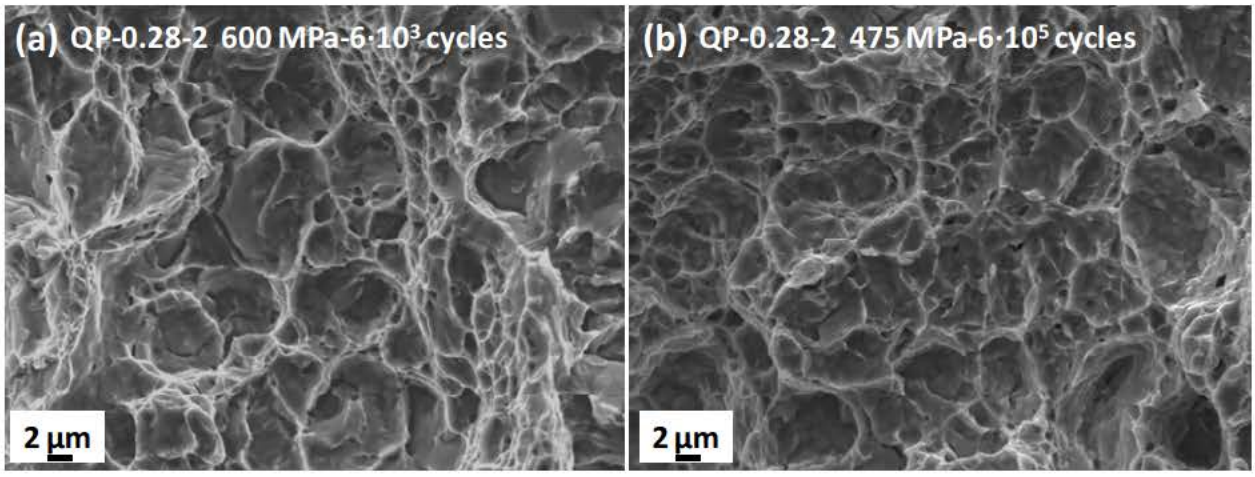

Figure 4-30. Fatigue fracture surface of the QP-0.28-2 grade formed in the final stage of fatigue after testing with high stress amplitude (600 MPa and $6 \cdot 10^3$ cycles) (a), and with low stress amplitude (475 MPa and $6 \cdot 10^5$ cycles) (b).

These observations indicate that grain/interphase boundary is the 'weakest link' in the microstructure of the Q&P steels subjected to fatigue testing with high stress amplitudes, whereas at lower stress amplitudes grain/interphase boundaries play a less important role in cyclic behavior of the material. As the fatigue life in the HCF regime is governed by fatigue crack nucleation, it can be suggested that enhancement of strength of grain/interphase boundary should improve fatigue life of the Q&P steels.

4.4.6. Conclusions to Section 4.4

High cycle fatigue behavior of Q&P steels was studied. The effect of microstructure and fatigue testing parameters on fatigue behavior, mechanisms of fatigue crack initiation and propagation along with the evolution of microstructure during cycling loading were analyzed. It was demonstrated that:

- Microstructure of Q&P steels plays a key role in their fatigue behavior. The Q&P steel with the higher volume fraction of RA shows higher fatigue limit,

that is related to delay of crack propagation due to austenite-martensite phase transformation. Volume fraction of RA tends to decrease with increasing stress amplitude in fatigue testing.

- Stability of RA against phase transformation during cyclic behavior is determined mainly by their size and crystallographic orientation, as in the case of monotonic uniaxial loading. Smaller RA grains show higher stability compared to the larger ones. The orientations with the highest transformation potentials transform first and the orientations with lowest transformation potentials transform later or remain stable. These tendencies are more pronounced at higher stress amplitudes.
- Inter-granular cracking is the only mechanism for fatigue crack initiation during fatigue testing with high stress amplitudes, whereas transgranular cracking is responsible for fatigue crack initiation during testing with lower stress amplitudes. Transgranular crack propagation dominates in the second stage of fatigue independently on the stress amplitude. The final stage of fatigue is also not affected by stress amplitude. Hence, the fatigue life of Q&P steels can be enhanced via improvement of strength of grain/interphase boundaries.

5 Conclusions

5. CONCLUSIONS

Following conclusions can be drawn based on the analysis of the outcomes of this work:

- Q&P steels have a complex microstructure: Irregular-shaped blocks of TM constitute the major phase of the microstructure, whereas the others (i.e. UM and RA) are dispersed in the matrix.
- The Q&P parameters significantly affect the microstructure of the studied steels, including size, morphology and distribution of microconstituents (RA, TM and UM), as well as the carbon content in RA. Mechanical properties of individual microconstituents are also strongly influenced by the Q&P parameters.
- Tensile mechanical properties of the Q&P steel grades are determined by their microstructure, particularly the volume fraction and morphology of RA. In addition, the plastic deformation of the Q&P steels at the microscale has a very complex character. Maps of local plastic strain distribution consist of network-like plastic deformation bands interconnected at spots which can accumulate very high amount of plastic strain.
- Matrix conditions (volume fraction and average grain size of TM and UM) play important role in fracture behavior of the Q&P steels. Local fracture initiation toughness is slightly improved with increasing volume fraction of RA, whereas the total crack growth resistance is significantly enhanced.
- Fatigue behavior of the Q&P steels is determined by their microstructure. In the studied materials, it is improved with increasing volume fraction of RA due to delay of crack propagation related to austenite-martensite phase transformation. Grain size and crystallographic orientation of RA are the key factors determining its stability against cyclic loading. Inter-granular cracking is the only fatigue crack initiation mechanism at high stress amplitudes, whereas transgranular cracking dominates at lower stress amplitudes. There is no effect of stress amplitude on mechanisms of fatigue crack propagation in the second and third stages of fatigue.

6 Future work

6. FUTURE WORK

The following areas of future work are envisioned:

- The optimum Q&P microstructure for enhanced fracture properties must be resolved. In order to do so, next studies should deepen into the effect of microstructural constituents on the fracture behavior of the Q&P steels. Special attention should be paid to the effect of morphology of RA, TM and UM on the crack propagation and fracture toughness in Q&P steels.

- As AHSSs appear as attractive candidates for construction engineering applications in arctic locations, their properties and behavior at low temperatures are to be investigated. Particularly, the effect of microstructure on the ductile-brittle transition temperature (DBTT) is of interest.

- The present PhD thesis focuses on uniaxial tensile ductility of Q&P steels. As Q&P steels have complex microstructure with metastable RA, significant effect of stress state on ductility can be expected. Analysis of formability of these materials in biaxial stretching could shed a light on the effect of stress triaxiality on their mechanical behavior.

- No reports on dynamic/crash behavior of Q&P steels can be found in the literature up to-date. Therefore, it might be interesting to analyze the impact/crash behavior of Q&P steels. In addition, the effect of individual phase constituents on the dynamic behavior of Q&P steels is worthy of investigation. Strain rate sensitivity studies could also provide valuable information on mechanical behavior of Q&P steels.

7 Bibliography

7. BIBLIOGRAPHY

[1] J. Galán, *et al.*, "Advanced high strength steels for automotive industry," *Revista de metalurgia*, vol. 48, pp. 118-131, 2012.

[2] F. G. Caballero, *et al.*, "Design of cold rolled and continuous annealed carbide-free bainitic steels for automotive application," *Materials & Design*, vol. 49, pp. 667-680, 2013.

[3] E. De Moor, *et al.*, "Strategies for third-generation advanced high-strength steel development," *AIST Transactions* vol. 7, pp. 133-144, 2010.

[4] H. K. D. H. Bhadeshia, "The bainite transformation: unresolved issues," *Materials Science and Engineering: A*, vol. 273–275, pp. 58-66, 1999.

[5] E. Rodríguez, *et al.*, "Caracterización dinámica de los cambios microestructurales en barras de aceros dúplex SAF 2205 utilizando la dimensión de información," *Revista de Metalurgia*, vol. 50, pp. 1-15, 2014.

[6] W. AutoSteel, *Advanced high-strength steels application guidelines* Brussels, Belgium, 2014.

[7] S. Keeler, "The proliferation of new types and grades of advanced high strength steels," *MetalForming Magazine*, vol. 48, 2014.

[8] H. K. D. H. Bhadeshia and S. R. Honeycombe, "3 - The iron-carbon equilibrium diagram and plain carbon steels," in *Steels (Third Edition)*, H. K. D. H. B. R. Honeycombe, Ed., ed Oxford: Butterworth-Heinemann, 2006, pp. 39-70.

[9] E. De Moor, *et al.*, "AIST Transactions strategies for third-generation advanced high-strength steel development," *Iron & Steel Technology*, vol. 7, p. 132, 2010.

[10] T. Hilditch, *et al.*, "Role of microstructure in the low cycle fatigue of multi-phase steels," *Materials Science and Engineering: A*, vol. 534, pp. 288-296, 2012.

[11] I. Cerny, *et al.*, "Fatigue properties of a low alloy 42SiCr steel heat treated by quenching and partitioning process," *11th International Conference on the Mechanical Behavior of Materials (Icm11)*, vol. 10, pp. 3310-3315, 2011.

[12] M. J. Santofimia, *et al.*, "Characterization of the microstructure obtained by the quenching and partitioning process in a low-carbon steel," *Materials Characterization*, vol. 59, pp. 1758-1764, 2008.

[13] C. Garcia-Mateo, *et al.*, "Tensile behaviour of a nanocrystalline bainitic steel containing 3 wt% silicon," *Materials Science and Engineering: A*, vol. 549, pp. 185-192, 2012.

[14] F. G. Caballero, *et al.*, "Theoretical design and advanced microstructure in super high strength steels," *Materials & Design*, vol. 30, pp. 2077-2083, 2009.

[15] E. De Moor, *et al.*, "Effect of retained austenite stabilized via quench and partitioning on the strain hardening of martensitic steels," *Metallurgical and Materials Transactions A*, vol. 39, pp. 2586-2595, 2008.

[16] J. G. Speer, *et al.*, "The "Quenching and Partitioning" process: background and recent progress," *Materials Research*, vol. 8, pp. 417-423, 2005.

[17] J. G. Speer and D. K. Matlock, "Recent developments in low-carbon sheet steels," *Journal of the Minerals Metals & Materials Society*, vol. 54, pp. 19-24, Jul 2002.

[18] D. Gutiérrez, *et al.*, "Evaluación del trabajo esencial de fractura en chapa de un acero de alta resistencia de fase dual," *Revista de Metalurgia*, vol. 49, pp. 45-54, 2013.

[19] J. Speer, *et al.*, "Carbon partitioning into austenite after martensite transformation," *Acta Materialia*, vol. 51, pp. 2611-2622, 2003.

[20] I. de Diego-Calderón, *et al.*, "Deformation behavior of a high strength multiphase steel at macro- and micro-scales," *Materials Science and Engineering: A*, vol. 611, pp. 201-211, 2014.

[21] D. De Knijf, *et al.*, "Effect of fresh martensite on the stability of retained austenite in quenching and partitioning steel," *Materials Science and Engineering: A*, vol. 615, pp. 107-115, 2014.

[22] J. G. Speer, *et al.*, "Critical assessment 7: quenching and partitioning," *Materials Science and Technology*, vol. 31, pp. 3-9, 2015.

[23] D. V. Edmonds, *et al.*, "Quenching and partitioning martensite—A novel steel heat treatment," *Materials Science and Engineering: A*, vol. 438–440, pp. 25-34, 2006.

[24] E. De Moor, *et al.*, "Effect of carbon and manganese on the quenching and partitioning response of CMnSi steels," *ISIJ International*, vol. 51, pp. 137-144, 2011.

[25] M. Sarikaya, *et al.*, "Solute element partitioning and austenite stabilization in steels," in *International Conference on Solid to Solid Phase Transformations*, Warrendale, PA, 1982, pp. 1421-1425.

[26] K. S. Choi, *et al.*, "Determination of carbon distributions in quenched and partitioned microstructures using nanoscale secondary ion mass spectroscopy," *Scripta Materialia*, vol. 104, pp. 79-82, 2015.

[27] Y. Toji, *et al.*, "Carbon partitioning during quenching and partitioning heat treatment accompanied by carbide precipitation," *Acta Materialia*, vol. 86, pp. 137-147, 2015.

[28] D. P. Koistinen and R. E. Marburger, "A general equation prescribing the extent of the austenite-martensite transformation in pure iron-carbon alloys and plain carbon steels," *Acta Metallurgica*, vol. 7, pp. 59-60, 1959.

[29] H. S. Yang, *et al.*, "More complete theory for the calculation of the martensite-start temperature in steels," *ISIJ International*, vol. 52, pp. 164-166, 2012.

[30] M. J. Santofimia, *et al.*, "Overview of mechanisms involved during the quenching and partitioning process in steels," *Metallurgical and Materials Transactions A*, vol. 42A, pp. 3620-3626, 2011.

[31] J. H. Jang, *et al.*, "Solubility of carbon in tetragonal ferrite in equilibrium with austenite," *Scripta Materialia*, vol. 68, pp. 195-198, 2013.

[32] H. Bhadeshia, "Carbon in cubic and tetragonal ferrite," *Philosophical Magazine*, vol. 93, pp. 3714-3725, 2013.

[33] J. Epp, *et al.*, "In situ X-Ray diffraction analysis of carbon partitioning during quenching of low carbon steel," *Metallurgical and Materials Transactions A*, vol. 43, pp. 2210-2217, 2012.

[34] M. J. Santofimia, *et al.*, "Microstructural evolution of a low-carbon steel during application of quenching and partitioning heat treatments after partial austenitization," *Metallurgical and Materials Transactions A*, vol. 40, pp. 46-57, 2009.

[35] G. Krauss, "Tempering and structural change in ferrous martensitic structures," in *International Conference on Phase Transformations in Ferrous Alloys*, Warrendale, PA, 1984, pp. 101-123.

[36] H. C. Lee and G. Krauss, "Interlath carbide transitions in martensitic medium-carbon steels tempered between 200 and 300C," in *Fundamentals of Aging and Tempering in Bainitic and Martensitic Steel Products*, Warrendale, PA, 1992, pp. 39-43.

[37] M. Hillert and J. Agren, "On the definitions of paraequilibrium and orthoequilibrium," *Scripta Materialia*, vol. 50, pp. 697-699, 2004.

[38] J. G. Speer, *et al.*, "Comments on "On the definitions of paraequilibrium and orthoequilibrium"," *Scripta Materialia*, vol. 52, pp. 83-85, Jan 2005.

[39] M. Hillert and J. Agren, "Reply to comments on "On the definition of paraequilibrium and orthoequilibrium"," *Scripta Materialia*, vol. 52, pp. 87-88, 2005.

[40] L. Barbe, *et al.*, "Characterization of the metastable austenite in low-alloy FeCMnSi TRIP-aided steel by neutron diffraction," *Zeitschrift Fur Metallkunde*, vol. 93, pp. 1217-1227, 2002.

[41] H. Bhadeshia and D. V. Edmonds, "Bainite transformation in a silicon steel," *Metallurgical Transactions A*, vol. 10, pp. 895-907, 1979.

[42] H. Wever, *Structure formation in alloys* vol. 69. Berlin: Wiley-V C H Verlag Gmbh, 1965.

[43] H. K. D. H. Bhadeshia and S. R. Honeycombe, "4 - The effects of alloying elements on iron-carbon alloys," in *Steels (Third Edition)*, H. K. D. H. B. R. Honeycombe, Ed., ed Oxford: Butterworth-Heinemann, 2006, pp. 71-93.

[44] J. Tobata, *et al.*, "Role of silicon in quenching and partitioning treatment of low-carbon martensitic stainless steel," *ISIJ International*, vol. 52, pp. 1377-1382, 2012.

[45] W. S. Owen, "The effect of silicon on the kinetics of tempering," *Transactions of the American Society for Metals*, vol. 46, pp. 812-829, 1954.

[46] A. Grajcar, *et al.*, "Third generation of AHSS with increased fraction of retained austenite for the automotive industry," *Archives of Civil and Mechanical Engineering*, vol. 12, pp. 334-341, 2012.

[47] A. Grajcar and R. Kuziak, "Thermomechanically processed TRIP steels with increased Mn content," *Steel Research International*, vol. 83, pp. 875-878, 2012.

[48] A. M. Streicher, *et al.*, "Advanced high strength sheet steels for automotive applications," in *Conference on Advanced High Strength Sheet Steels for Automotive Applications*, Warrendale, PA, 2004, pp. 51-62.

[49] J. G. Speer, *et al.*, "Quenching and partitioning: a fundamentally new process to create high strength TRIP sheet microstructures," *Symposium on the Thermodynamics, Kinetics, Characterization and Modeling of Austenite Formation and Decomposition*, pp. 505-522, 2003.

[50] A. J. Clarke, *et al.*, "Influence of carbon partitioning kinetics on final austenite fraction during quenching and partitioning," *Scripta Materialia*, vol. 61, pp. 149-152, 2009.

[51] D. T. Pierce, *et al.*, "Characterization of transition carbides in quench and partitioned steel microstructures by Mössbauer spectroscopy and complementary techniques," *Acta Materialia*, vol. 90, pp. 417-430, 2015.

[52] E. Paravicini Bagliani, *et al.*, "Microstructure, tensile and toughness properties after quenching and partitioning treatments of a medium-carbon steel," *Materials Science and Engineering: A*, vol. 559, pp. 486-495, 2013.

[53] X. Tan, *et al.*, "Microstructure–properties relationship in a one-step quenched and partitioned steel," *Materials Science and Engineering: A*, vol. 589, pp. 101-111, 2014.

[54] W. Q. Cao, *et al.*, "Application of quenching and partitioning to improve ductility of ultrahigh strength low alloy steel," in *Pricm 7, Pts 1-3*. vol. 654-656, J. F. Nie and A. Morton, Eds., ed Stafa-Zurich: Trans Tech Publications Ltd, 2010, pp. 29-32.

[55] F. Rizzo, *et al.*, "Quenching and partitioning of Ni-added high strength steels," in *THERMEC 2006, Pts 1-5*. vol. 539-543, T. Chandra, *et al.*, Eds., ed Stafa-Zurich: Trans Tech Publications Ltd, 2007, pp. 4476-4481.

[56] A. R. Martins, *et al.*, "Microstructure and mechanical properties of Ni-added high strength steels subjected to quenching and partitioning (Q&P) heat treatment," in *Materials Science & Technology 2009 Conference and Exhibition (MS&T Partner Societies)*, Pittsburgh, PA, 2009, pp. 1564-1574.

[57] B. Mašek, Jirková H., Hauserová, D., Kučerová L., Klauberová D., "The effect of Mn and Si on the properties of advanced high strength steels processed by quenching and partitioning " *Materials Science Forum*, vol. 654-656, pp. 94-97, 2010.

[58] E. De Moor, *et al.*, "Effect of Si, Al and Mo alloying on tensile properties obtained by quenching and partitioning," in *Materials Science and Technology*, Pittsburgh, PA, 2009, pp. 1554-1563.

[59] M. J. Santofimia, *et al.*, "New low carbon Q&P steels containing film-like intercritical ferrite," *Materials Science and Engineering: A*, vol. 527, pp. 6429-6439, 2010.

[60] Q. Furnemont, *et al.*, "On the measurement of the nanohardness of the constitutive phases of TRIP-assisted multiphase steels," *Materials Science and Engineering: A*, vol. 328, pp. 26-32, May 2002.

[61] A. I. H. Committee, *ASM Handbook: properties and selection: irons steels and high performance alloys*. USA: ASM International, 1990.

[62] B. B. He, *et al.*, "Nanoindentation investigation on the mechanical stability of individual austenite grains in a medium-Mn transformation-induced plasticity steel," *Scripta Materialia*, vol. 69, pp. 215-218, 2013.

[63] T. Ohmura, *et al.*, "Evaluation of the matrix strength of Fe-0.4 wt% C tempered martensite using nanoindentation techniques," *Philosophical Magazine A*, vol. 82, pp. 1903-1910, Jul 2002.

[64] T. Ohmura, *et al.*, "Evaluation of temper softening behavior of Fe–C binary martensitic steels by nanoindentation," *Scripta Materialia*, vol. 49, pp. 1157-1162, 2003.

[65] M. D. Taylor, *et al.*, "Correlations between nanoindentation hardness and macroscopic mechanical properties in DP980 steels," *Materials Science and Engineering: A*, vol. 597, pp. 431-439, 2014.

[66] X. Tan, *et al.*, "Effect of partitioning procedure on microstructure and mechanical properties of a hot-rolled directly quenched and partitioned steel," *Materials Science and Engineering: A*, vol. 594, pp. 149-160, 2014.

[67] Q. Han, *et al.*, "Strain partitioning in dual-phase steels containing tempered martensite," *Materials Science and Engineering: A*, vol. 611, pp. 90-99, 2014.

[68] Q. H. Han, *et al.*, "Quantitative measurement of strain partitioning and slip systems in a dual-phase steel," *Scripta Materialia*, vol. 69, pp. 13-16, Jul 2013.

[69] M. Kapp, *et al.*, "A micro-level strain analysis of a high-strength dual-phase steel," *International Journal of Materials Research*, vol. 102, pp. 687-691, 2011.

[70] J. D. Kang, *et al.*, "Digital image correlation studies for microscopic strain distribution and damage in dual phase steels," *Scripta Materialia*, vol. 56, pp. 999-1002, 2007.

[71] A. El Bartali, *et al.*, "Strain heterogeneities between phases in a duplex stainless steel. Comparison between measures and simulation," in *Fatigue 2010*. vol. 2, P. Lukas, Ed., ed Amsterdam: Elsevier Science Bv, 2010, pp. 2229-2237.

[72] D. Hauserová, *et al.*, "Properties of advanced experimental CMnSiMo steel achieved by QP process," *Procedia Engineering*, vol. 10, pp. 2961-2966, 2011.

[73] H. Ghadbeigi, *et al.*, "Local plastic strain evolution in a high strength dual-phase steel," *Materials Science and Engineering A*, vol. 527, pp. 5026-5032, 2010.

[74] K. Unterweger and O. Kolednik, "The local deformation behaviour of MMCs - an experimental study," *Zeitschrift Fur Metallkunde*, vol. 96, pp. 1063-1068, 2005.

[75] A. B. Pandey, *et al.*, "Deformation and fracture of a particle-reinforced aluminum alloy composite: Part I. Experiments," *Metallurgical and Materials Transactions A*, vol. 31, pp. 921-936, 2000.

[76] O. Kolednik and K. Unterweger, "The ductility of metal matrix composites - relation to local deformation behavior and damage evolution," *Engineering Fracture Mechanics*, vol. 75, pp. 3663-3676, 2008.

[77] X. C. Xiong, *et al.*, "The effect of morphology on the stability of retained austenite in a quenched and partitioned steel," *Scripta Materialia*, vol. 68, pp. 321-324, 2013.

[78] R. Ding, *et al.*, "A novel design to enhance the amount of retained austenite and mechanical properties in low-alloyed steel," *Scripta Materialia*, vol. 88, pp. 21-24, 2014.

[79] T. H. Ahn, *et al.*, "Investigation of strain-induced martensitic transformation in metastable austenite using nanoindentation," *Scripta Materialia*, vol. 63, pp. 540-543, 2010.

[80] Z. J. Xie, *et al.*, "Stability of retained austenite in multi-phase microstructure during austempering and its effect on the ductility of a low carbon steel," *Materials Science and Engineering: A*, vol. 603, pp. 69-75, 2014.

[81] K. Zhang, *et al.*, "A new effect of retained austenite on ductility enhancement in high-strength quenching–partitioning–tempering martensitic steel," *Materials Science and Engineering: A*, vol. 528, pp. 8486-8491, 2011.

[82] C. Y. Wang, *et al.*, "Characterization of microstructure obtained by quenching and partitioning process in low alloy martensitic steel," *Materials Science and Engineering: A*, vol. 527, pp. 3442-3449, 2010.

[83] J. Chiang, *et al.*, "Effect of microstructure on retained austenite stability and work hardening of TRIP steels," *Materials Science and Engineering A*, vol. 528, pp. 4516-4521, 2011.

[84] R. Blondé, *et al.*, "Mechanical stability of individual austenite grains in TRIP steel studied by synchrotron X-ray diffraction during tensile loading," *Materials Science and Engineering: A*, vol. 618, pp. 280-287, 2014.

[85] D. De Knijf, *et al.*, "Study of heat treatment parameters and kinetics of quenching and partitioning cycles," *Materials Science and Technology*, vol. 31, pp. 817-828, 2015.

[86] D. De Knijf, *et al.*, "Factors influencing the austenite stability during tensile testing of quenching and partitioning steel determined via in-situ Electron Backscatter Diffraction," *Materials Science and Engineering: A*, vol. 638, pp. 219-227, 2015.

[87] N. H. van Dijk, *et al.*, "Thermal stability of retained austenite in TRIP steels studied by synchrotron X-ray diffraction during cooling," *Acta Materialia*, vol. 53, pp. 5439-5447, 2005.

[88] E. Jimenez-Melero, *et al.*, "Characterization of individual retained austenite grains and their stability in low-alloyed TRIP steels," *Acta Materialia*, vol. 55, pp. 6713-6723, 2007.

[89] E. Jimenez-Melero, *et al.*, "The effect of aluminium and phosphorus on the stability of individual austenite grains in TRIP steels," *Acta Materialia*, vol. 57, pp. 533-543, 2009.

[90] R. Blondé, *et al.*, "High-energy X-ray diffraction study on the temperature-dependent mechanical stability of retained austenite in low-alloyed TRIP steels," *Acta Materialia*, vol. 60, pp. 565-577, 2012.

[91] E. Jimenez-Melero, *et al.*, "Martensitic transformation of individual grains in low-alloyed TRIP steels," *Scripta Materialia*, vol. 56, pp. 421-424, 2007.

[92] P. J. Jacques, *et al.*, "On the influence of interactions between phases on the mechanical stability of retained austenite in transformation-induced plasticity multiphase steels," *Metallurgical and Materials Transactions A*, vol. 32, pp. 2759-2768, 2001.

[93] K. Sugimoto, *et al.*, "Effects of volume fraction and stability of retained austenite on ductility of TRIP-aided Dual Phase steels," *ISIJ International*, vol. 32, pp. 1311-1318, 1992.

[94] I. B. Timokhina, *et al.*, "Effect of microstructure on the stability of retained austenite in transformation-induced-plasticity steels," *Metallurgical and Materials Transactions A*, vol. 35, pp. 2331-2341, 2004.

[95] D. De Knijf, *et al.*, "Orientation dependence of the martensite transformation in a quenched and partitioned steel subjected to uniaxial tension," *Journal of Applied Crystallography*, vol. 47, pp. 1261-1266, 2014.

[96] J. Wang and S. Van Der Zwaag, "Stabilization mechanisms of retained austenite in transformation-induced plasticity steel," *Metallurgical and Materials Transactions A*, vol. 32, pp. 1527-1539, 2001.

[97] K. Sugimoto, *et al.*, "Ductility and formability of newly developed high strength low alloy TRIP-aided sheet steels with annealed martensite matrix," *ISIJ International*, vol. 42, pp. 910-915, 2002.

[98] A. F. L. Mark, PhD thesis, Microstructural effects on the stability of retained austenite in Transformation Induced Plasticity Steels, Queen's University, Ontario, 2007.

[99] P. J. Jacques, "Transformation-induced plasticity for high strength formable steels," *Current Opinion in Solid State and Materials Science*, vol. 8, pp. 259-265, 2004.

[100] P. Jacques, *et al.*, "Bainite transformation of low carbon Mn–Si TRIP-assisted multiphase steels: influence of silicon content on cementite precipitation and austenite retention," *Materials Science and Engineering: A*, vol. 273–275, pp. 475-479, 1999.

[101] G. E. Dieter, *Mechanical metallurgy*. New York: McGraw-Hill, 1976.

[102] T. L. Anderson, *Fracture mechanics: fundamentals and applications*, Third Edition ed.: CRC press., 2011.

[103] H. Yoshida and M. Nagumo, "Microstructures controlling the ductile crack growth resistance of low carbon steels," *Metallurgical and Materials Transactions A*, vol. 29, pp. 279-287, 1998.

[104] H. Liebowitz, *Fracture: An advanced treatise*: Academic Press, 1969.

[105] R. Wu, *et al.*, "Effect of retained austenite on the fracture toughness of quenching and partitioning (Q&P)-treated sheet steels," *Metallurgical and Materials Transactions A*, pp. 1-11, 2013.

[106] X. Sun, *et al.*, "On key factors influencing ductile fractures of dual phase (DP) steels," *Materials Science and Engineering: A*, vol. 526, pp. 140-149, 2009.

[107] O. Kolednik, *et al.*, "The fracture resistance of a ferritic-austenitic duplex steel," *Acta Materialia*, vol. 44, pp. 3307-3319, 1995.

[108] S. Antolovich and B. Singh, "On the toughness increment associated with the austenite to martensite phase transformation in TRIP steels," *Metallurgical and Materials Transactions B*, vol. 2, pp. 2135-2141, 1971.

[109] P. Jacques, *et al.*, "On the role of martensitic transformation on damage and cracking resistance in trip-assisted multiphase steels," *Acta Materialia*, vol. 49, pp. 139-152, 2001.

[110] G. Lacroix, *et al.*, "The fracture toughness of TRIP-assisted multiphase steels," *Acta Materialia*, vol. 56, pp. 3900-3913, 2008.

[111] S. Chatterjee and H. K. D. H. Bhadeshia, "TRIP-assisted steels: cracking of high-carbon martensite," *Materials Science and Technology*, vol. 22, pp. 645-649, 2006.

[112] M. Calcagnotto, *et al.*, "Deformation and fracture mechanisms in fine- and ultrafine-grained ferrite/martensite dual-phase steels and the effect of aging," *Acta Materialia*, vol. 59, pp. 658-670, 2011.

[113] M. Calcagnotto, *et al.*, "Effect of grain refinement to 1 μm on strength and toughness of dual-phase steels," *Materials Science and Engineering: A*, vol. 527, pp. 7832-7840, 2010.

[114] S. Mocarski, "Total approach to reliability of case-hardened parts," *Metal Progress*, vol. 98, pp. 96-98, 1970.

[115] R. Idris and Y. Prawoto, "Influence of ferrite fraction within martensite matrix on fatigue crack propagation: An experimental verification with dual phase steel," *Materials Science and Engineering A*, vol. 552, pp. 547-554, 2012.

[116] S. Li, *et al.*, "Effects of microstructure on fatigue crack growth behavior in cold-rolled dual phase steels," *Materials Science and Engineering: A*, vol. 612, pp. 153-161, 2014.

[117] Z. Z. Hu, *et al.*, "The effect of austenite on low cycle fatigue in three-phase steel," *International Journal of Fatigue*, vol. 19, pp. 641-646, 1997.

[118] G. Baudry and A. Pineau, "Influence of strain-induced martensitic transformation on the low-cycle fatigue behavior of a stainless steel," *Materials Science and Engineering,* vol. 28, pp. 229-242, 1977.

[119] A. M. Sarosiek and W. S. Owen, "The work-hardening of dual-phase steels at small plastic strains," *Materials Science and Engineering,* vol. 66, pp. 13-34, 1984.

[120] X. Cheng, *et al.*, "Fatigue crack growth in TRIP steel under positive R-ratios," *Engineering Fracture Mechanics,* vol. 75, pp. 739-749, 2008.

[121] G. N. Haidemenopoulos, *et al.*, "On the effect of austenite stability on high cycle fatigue of TRIP 700 steel," *Materials Science and Engineering A,* vol. 573, pp. 7-11, 2013.

[122] S. K. Paul, *et al.*, "Effect of martensite volume fraction on low cycle fatigue behaviour of dual phase steels: Experimental and microstructural investigation," *Materials Science and Engineering: A,* vol. 638, pp. 296-304, 2015.

[123] D. A. Porter and K. E. Easterling, *Phase transformations in metals and alloys* Third Edition ed.: Taylor & Francis, 1992.

[124] A. Grajcar, *et al.*, "Seggregation of alloying elements in thermomechanically rolled medium-Mn multiphase steels," *Journal of Achievements in Materials and Manufacturing Engineering,* vol. 55, pp. 256-264, 2012.

[125] M. V. Li, *et al.*, "A computational model for the prediction of steel hardenability," *Metallurgical and Materials Transactions B,* vol. 29, pp. 661-672, 1998.

[126] R. A. Grange, "Estimating the hardenability of carbon steels," *Metallurgical Transactions,* vol. 4, pp. 2231-2244, 1973.

[127] S.-J. Kim, *et al.*, "Effect of Cu, Cr and Ni on mechanical properties of 0.15 wt.% C TRIP-aided cold rolled steels," *Scripta Materialia,* vol. 48, pp. 539-544, 2003.

[128] J. G. Speer, *et al.*, "Partitioning of carbon from supersaturated plates of ferrite, with application to steel processing and fundamentals of the bainite transformation," *Current Opinion in Solid State & Materials Science,* vol. 8, pp. 219-237, 2004.

[129] J. O. Andersson, *et al.*, "Thermo-Calc & DICTRA, computational tools for materials science," *Calphad,* vol. 26, pp. 273-312, 2002.

[130] S. M. C. van Bohemen, "Bainite and martensite start temperature calculated with exponential carbon dependence," *Materials Science and Technology,* vol. 28, pp. 487-495, 2012.

[131] E. De Moor, *et al.*, "Calorimetric study of carbon partitioning from martensite into austenite steel," *Physical Review B,* vol. 82, 2010.

[132] B. E. Warren, *X-ray diffraction*. Mineola, New York: Dover Publications, 1969.

[133] B. D. Cullity, *Elements of X-ray diffraction, 2nd edition*. Boston: Addison-Wesley, 1978.

[134] J. Als-Nielsen and D. McMorrow, *Elements of modern X-ray physics*: Wiley, 2001.

[135] W. H. Bragg, "X-rays and crystal structure, with special reference to certain metals," *Journal of the Institute of Metals,* vol. 16, pp. 2-17, 1916.

[136] C. Suryanarayana and G. Norton, *X-Ray diffraction: A practical approach*: Springer, 1998.

[137] C. A. Schneider, *et al.*, "NIH Image to ImageJ: 25 years of image analysis," *Nature Methods,* vol. 9, pp. 671-675, 2012.

[138] A. Bogner, *et al.*, "A history of scanning electron microscopy developments: Towards "wet-STEM" imaging," *Micron,* vol. 38, pp. 390-401, 2007.

[139] D. Stojakovic, "Electron backscatter diffraction in materials characterization," *Processing and Application of Ceramics: PAC,* vol. 6, pp. 1-13, 2012.

[140] V. Randle, "Electron backscatter diffraction: Strategies for reliable data acquisition and processing," *Materials Characterization,* vol. 60, pp. 913-922, 2009.

[141] J. Jiang, *et al.*, "Microtexture evolution via deformation twinning and slip during compression of magnesium alloy AZ31," *Materials Science and Engineering A,* vol. 483-84, pp. 576-579, 2008.

[142] D. Raabe, *et al.*, "Characterization of the microstructure and texture of nanostructured electrodeposited NiCo using electron backscatter diffraction (EBSD)," *Acta Materialia,* vol. 54, pp. 2451-62, 2006.

[143] V. Randle, *et al.*, "Five-parameter grain boundary distribution of commercially grain boundary engineered nickel and copper," *Acta Materialia,* vol. 56, pp. 2363-2373, 2008.

[144] M. G. Perez, *et al.*, "Identification of phases in zinc alloy powders using electron backscatter diffraction," *Materials Science and Engineering A,* vol. 424, pp. 239-250, 2006.

[145] A. J. Wilkinson, *et al.*, "High-resolution elastic strain measurement from electron backscatter diffraction patterns: New levels of sensitivity," *Ultramicroscopy,* vol. 106, pp. 307-313, 2006.

[146] P. V. C. Hough, "Machine analysis of bubble chamber pictures," in *High Energy Accelerators and Instrumentation, CERN*, Geneva, Switzerland, 1959, pp. 554-556.

[147] R. O. Duda and P. E. Hart, "Use of Hough transformation to detect lines and curves in pictures," *Communications of the Acm,* vol. 15, 1972.

[148] W. H. Miller, *A treatise on crystallography*: For J. & J. J. Deighton, 1839.

[149] M. K. Adam J. Schwartz, Brent L. Adams, David P. Field, *Electron backscatter diffraction in materials science*. New York City: Springer US, 2009.

[150] S. I. Wright and M. M. Nowell, "EBSD image quality mapping," *Microscopy and Microanalysis,* vol. 12, pp. 72-84, 2006.

[151] G. N. P. Suwas S., "Crystallograpic texture in Materials," *Journal of the Indian Institute of Science,* vol. 88, pp. 151-177, 2008.

[152] F. J. Humphreys and M. Hatherly, "Chapter 3 - Deformation textures," in *Recrystallization and Related Annealing Phenomena (Second Edition)*, F. J. H. Hatherly, Ed., ed Oxford: Elsevier, 2004, pp. 67-89.

[153] V. Randle and O. Engler, *Introduction to texture analysis: macrostructure, microstructure and orientation mapping*. Boca Raton CRC Press, 2009.

[154] H. J. Bunge, "Textures in multiphase alloys," *Zeitschrift Fur Metallkunde,* vol. 76, pp. 92-101, 1985.

[155] D. Johnson, *et al.*, "Chapter 1 - Basic principles of atomic force microscopy," in *Atomic Force Microscopy in Process Engineering*, W. R. Bowen and N. Hilal, Eds., ed Oxford: Butterworth-Heinemann, 2009, pp. 1-30.

[156] J. R. Davis, *Tensile testing, 2nd Edition*. Novelty: A S M International, 2004.

[157] A. C. Fischer-Cripps, *Nanoindentation*. New York: Springer 2011.

[158] E. S. Berkovich, "Three-faceted diamond pyramid for micro-hardness testing," *Industrial Diamond Review,* vol. 11, pp. 129-133, 1951.

[159] W. C. Oliver and G. M. Pharr, "An improved technique for determining hardness and Elastic-Modulus using load and displacement sensing indentation experiments," *Journal of Materials Research,* vol. 7, pp. 1564-1583, 1992.

[160] G. Z. Voyiadjis and R. Peters, "Size effects in nanoindentation: an experimental and analytical study," *Acta Mechanica,* vol. 211, pp. 131-153, 2010.

[161] L. P. Canal, *et al.*, "Application of digital image correlation at the microscale in fiber-reinforced composites," *Composites Part A,* vol. 43, pp. 1630-1638, 2012.

[162] I. de Diego-Calderón, *et al.*, "Global and local deformation behavior and mechanical properties of individual phases in a quenched and partitioned steel," *Materials Science and Engineering: A,* vol. 630, pp. 27-35, 2015.

[163] Q. Han, *et al.*, "Quantitative measurement of strain partitioning and slip systems in a dual-phase steel," *Scripta Materialia,* vol. 69, pp. 13-16, 2013.

[164] M. A. Sutton, *et al.*, *Image correlation for shape, motion and deformation measurements: basic concepts, theory and applications*: Springer, 2009.

[165] A. A. Wells, "Unstable crack propagation in metals: cleavage and fast fracture," in *Crack Propagation Symposium*, Cranfield, UK, 1961.

[166] J. R. Rice, "A path independent integral and approximate analysis of strain concentration by notches and cracks," *Journal of Applied Mechanics,* vol. 35, 1968.

[167] J. W. Hutchinson, "Singular behavior at end of a tensile crack in a hardening material," *Journal of the Mechanics and Physics of Solids,* vol. 16, 1968.

[168] J. R. Rice and G. F. Rosengren, "Plane strain deformation near a crack tip in a power-law hardening material," *Journal of the Mechanics and Physics of Solids,* vol. 16, 1968.

[169] C. F. Shih, "Relationships between the J-integral and the crack opening displacement for stationary and extending cracks," *Journal of the Mechanics and Physics of Solids,* vol. 29, pp. 305-326, 1981.

[170] B. Cotterell, *et al.*, "Measuring toughness and the cohesive stress–displacement relationship by the essential work of fracture concept," *Engineering Fracture Mechanics,* vol. 72, pp. 827-848, 2005.

[171] R. Knockaert, *et al.*, "Experimental and numerical investigation of fracture in double-edge notched steel plates," *International Journal of Fracture,* vol. 81, pp. 383-399, 1996.

[172] H. H. Johnson, "Calibrating electric potential method for studying slow crack growth " *Materials Research and Standards,* vol. 5, pp. 442-445, 1965.

[173] J. Stampfl, *et al.*, "Reconstruction of surface topographies by scanning electron microscopy for application in fracture research," *Applied physics A,* vol. 63, pp. 341-346, 1996.

[174] S. Scherer and O. Kolednik, "A new system for automatic surface analysis in SEM," *The Amercias Microscopy and Analysis,* vol. 336, pp. 15-17 2001.

[175] A. Tatschl and O. Kolednik, "A new tool for the experimental characterization of micro-plasticity," *Materials Science and Engineering A,* vol. 339, pp. 265-280, 2003.

[176] J. Stampfl, *et al.*, "Determination of the fracture toughness by automatic image processing," *International Journal of Fracture,* vol. 78, pp. 35-44, 1996.

[177] A. Hohenwarter and R. Pippan, "A comprehensive study on the damage tolerance of ultrafine-grained copper," *Materials Science and Engineering A,* vol. 540, pp. 89-96, 2012.

[178] J. Stampfl and O. Kolednik, "The separation of the fracture energy in metallic materials," *International Journal of Fracture*, vol. 101, pp. 321-345, 2000.

[179] I. Sabirov and O. Kolednik, "The effect of inclusion size on the local conditions for void nucleation near a crack tip in a mild steel," *Scripta Materialia*, vol. 53, pp. 1373-1378, 2005.

[180] I. Sabirov and O. Kolednik, "Local and global measures of the fracture toughness of metal matrix composites," *Materials Science and Engineering: A*, vol. 527, pp. 3100-3110, 2010.

[181] I. Sabirov, *et al.*, "Equal channel angular pressing of metal matrix composites: Effect on particle distribution and fracture toughness," *Acta Materialia*, vol. 53, pp. 4919-4930, 2005.

[182] "International Organization for Standardization," in *ISO 1099:2006(E): Metallic materials - Fatigue testing - Axial force controlled method*, ed Geneva, Switzerland, 2006.

[183] G. K. Tirumalasetty, *et al.*, "Deformation-induced austenite grain rotation and transformation in TRIP-assisted steel," *Acta Materialia*, vol. 60, pp. 1311-1321, 2012.

[184] M. J. Santofimia, *et al.*, "Microstructural development during the quenching and partitioning process in a newly designed low-carbon steel," *Acta Materialia*, vol. 59, pp. 6059-6068, 2011.

[185] Y. Prawoto, *et al.*, "Effect of prior austenite grain size on the morphology and mechanical properties of martensite in medium carbon steel," *Journal of Materials Science & Technology*, vol. 28, pp. 461-466, 2012.

[186] A. J. Kaijalainen, *et al.*, "Effect of austenite grain structure on the strength and toughness of direct-quenched martensite," *Journal of Alloys and Compounds*, vol. 577, Supplement 1, pp. S642-S648, 2013.

[187] A. S. Schulz-Beenken, "Martensite in steels: its significance, recent developments and trends," *J. Phys. IV France*, vol. 07, pp. C5-359-C5-366, 1997.

[188] J. Sun, *et al.*, "Study of microstructural evolution, microstructure-mechanical properties correlation and collaborative deformation-transformation behavior of quenching and partitioning (Q&P) steel," *Materials Science and Engineering: A*, vol. 596, pp. 89-97, 2014.

[189] M. S. Joo, *et al.*, "Experiments to separate the effect of texture on anisotropy of pipeline steel," *Materials Science and Engineering: A*, vol. 556, pp. 601-606, 2012.

[190] R. Petrov, *et al.*, "Microstructure and texture of a lightly deformed TRIP-assisted steel characterized by means of the EBSD technique," *Materials Science and Engineering A*, vol. 447, pp. 285-297, 2007.

[191] D. Kramer, *et al.*, "Yield strength predictions from the plastic zone around nanocontacts," *Acta Materialia*, vol. 47, pp. 333-343, 1998.

[192] C. L. Woodcock and D. F. Bahr, "Plastic zone evolution around small scale indentations," *Scripta Materialia*, vol. 43, pp. 783-788, 2000.

[193] A. F. Mark, *et al.*, "Development and characterisation of model TRIP steel microstructures," *Materials Science and Engineering: A*, vol. 576, pp. 108-117, 2013.

[194] K. Sekido, *et al.*, "Nanoindentation/atomic force microscopy analyses of ε - martensitic transformation and shape memory effect in Fe–28Mn–6Si–5Cr alloy," *Scripta Materialia*, vol. 65, pp. 942-945, 2011.

[195] P. S. Phani, *et al.*, "A stochastic model for the size dependence of spherical indentation pop-in," *Journal of Materials Research*, vol. 28, pp. 2728-2739, 2013.

[196] R. D. K. Misra, *et al.*, "Ultrahigh strength martensite-austenite dual-phase steels with ultrafine structure: The response to indentation experiments," *Materials Science and Engineering: A*, vol. 560, pp. 693-699, 2013.

[197] K. L. Johnson, "Contact mechanics," *Proceedings of the Institution of Mechanical Engineers Part J-Journal of Engineering Tribology*, vol. 223, pp. 254-254, 2009.

[198] W. W. Gerberich, *et al.*, "Indentation induced dislocation nucleation: The initial yield point," *Acta Materialia*, vol. 44, pp. 3585-3598, 1996.

[199] J. Pesicka, *et al.*, "The evolution of dislocation density during heat treatment and creep of tempered martensite ferritic steels," *Acta Materialia*, vol. 51, pp. 4847-4862, 2003.

[200] J. Friedel, *Dislocations*. Reading, MA: Pergamon Press; [U.S.A. ed. distributed by] Addison-Wesley Publishing Company, 1964.

[201] A. A. Elmustafa, *et al.*, "Activation volume analysis of plastic deformation in fcc materials using nanoindentation," in *Surface Engineering 2002-Synthesis, Characterization and Applications*. vol. 750, A. Kumar, *et al.*, Eds., ed Warrendale: Materials Research Society, 2003, pp. 77-82.

[202] A. A. Elmustafa and D. S. Stone, "Nanoindentation and the indentation size effect: Kinetics of deformation and strain gradient plasticity," *Journal of the Mechanics and Physics of Solids*, vol. 51, pp. 357-381, 2003.

[203] A. Carpinteri and S. Puzzi, "A fractal approach to indentation size effect," *Engineering Fracture Mechanics*, vol. 73, pp. 2110-2122, 2006.

[204] H. Zhang, *et al.*, "Designing quadplex (four-phase) microstructures in an ultrahigh carbon steel," *Materials Science and Engineering: A*, vol. 612, pp. 46-53, 2014.

[205] G. Krauss, "Deformation and fracture in martensitic carbon steels tempered at low temperatures," *Metallurgical and Materials Transactions A*, vol. 32, pp. 861-877, 2001/04/01 2001.

[206] H. P. Stüwe, "The work necessary to form a ductile fracture surface," *Engineering Fracture Mechanics*, vol. 13, pp. 231-236, 1980.

[207] H. Stüwe, "The plastic work spent in ductile fracture," *Three-dimensional constitutive relations and ductile fracture (A 83-18477 06-39) Amsterdam, North-Holland Publishing Co.*, pp. 213-221, 1981.

[208] W. W. Gerberich, *et al.*, "Fracture and fractography of metastable austenites," *Metallurgical and Materials Transactions B*, vol. 2, pp. 2243-2253, 1971/08/01 1971.

[209] I. Sabirov, *et al.*, "About application of three dimensional analyses of fracture surfaces in fracture study on nanostructured titanium," *Computational Materials Science*, vol. 76, pp. 72-79, 2013.

[210] I. de Diego-Calderón, *et al.*, "Effect of Q&P parameters on microstructure development and mechanical behavior of Q&P steels," *Revista de Metalurgia*, vol. 51, pp. 1-12, 2015.

[211] G. B. Olson and M. Cohen, "Stress-assisted isothermal martensitic-transformation. Application to TRIP steels," *Metallurgical Transactions A*, vol. 13, pp. 1907-1914, 1982.

[212] C. Y. Huo and H. L. Gao, "Strain-induced martensitic transformation in fatigue crack tip zone for a high strength steel," *Materials Characterization*, vol. 55, pp. 12-18, 2005.